ABSTRACT

Title of Thesis: EXPERIMENTAL MODELING OF
TWIN-SCREW EXTRUSION PROCESSES
TO PREDICT PROPERTIES OF
EXTRUDED COMPOSITES

Benjamin J. Dryer, Master of Science, 2016

Directed by: Associate Professor, David I. Bigio
Department of Mechanical Engineering

Twin-screw extrusion is used to compound fillers into a polymer matrix in order to improve the properties of the final product. The resultant properties of the composite are determined by the operating conditions used during extrusion processing. Changes in the operating conditions affect the physics of the melt flow, inducing unique composite properties. In the following work, the Residence Stress Distribution methodology has been applied to model both the stress behavior and the property response of a twin-screw compounding process as a function of the operating conditions. The compounding of a pigment into a polymer melt has been investigated to determine the effect of stress on the degree of mixing, which will affect the properties of the composite. In addition, the pharmaceutical properties resulting from the compounding of an active pharmaceutical ingredient are modeled as a function of the operating conditions, indicating the physical behavior inducing the property responses.

EXPERIMENTAL MODELING OF TWIN-SCREW EXTRUSION PROCESSES TO PREDICT PROPERTIES OF EXTRUDED COMPOSITES

By

Benjamin Joseph Dryer

Thesis submitted to the Faculty of the Graduate School of the
University of Maryland, College Park in partial fulfillment
of the requirements for the degree of
Master of Science
2016

Advisory Committee:
Professor David Bigio, Chair/Advisor
Professor Hugh Bruck
Professor Johan Larsson

Acknowledgements

I would like to sincerely thank my advisor Dr. David Bigio for helping and guiding me throughout my research. Our discussions always provoked new thoughts on the research as well as my own personal development. I would also like to thank Dr. Hugh Bruck and Dr. Johan Larsson for serving on my committee.

Additionally, I would like to thank and acknowledge several of my colleagues in the Advanced Manufacturing Laboratory. Graduate students Jason Nixon and Graeme Fukuda provided invaluable guidance and support throughout my years here. Their experience and knowledge were essential in my progression from an undergraduate to a graduate student. I would also like to thank Jake Webb, Kyle Montemayor, Kathir Nalluswami, and Leslie Jones-Doves for completing and assisting with several experiments. Their help and dedication were crucial to the completion of this research.

I would like to thank our industry collaborators at Merck, Chemours, DuPont, and Coperion. Specifically, I want to acknowledge Chad Brown, Phil Niedenzu, Mark Wetzel, and Paul Andersen for their insights and guidance. This research could not have been completed without the relationships and resources provided by our partners in industry.

Finally, I would like to acknowledge my family and friends for their unrelenting support. I could not have finished this research without the motivation and encouragement they provided.

Contents

List of Figures

List of Tables

Abbreviations

API	**A**ctive **P**harmaceutical **I**ngredient
CAMES	**Ca**librated **M**icro**e**ncapuslated **S**ensor (beads)
CCD	**C**entral **C**omposite **D**esign
CoTSE	**Co**rotating **T**win-**S**crew Extruder
DoE	**D**esign **o**f **E**xperiments
EMMA	**E**thylene **m**eta-**m**ethyl **a**crylate
HDPE	**H**igh-**d**ensity **P**oly**e**theyle
HIPS	**H**igh-**i**mpact **P**oly**s**tyrene
HPLC	**H**igh-**p**erformance **L**iquid **C**hromatography
LLDPE	**Linear L**ow-**d**ensity **P**oly**e**theyle
LDPE	**L**ow-**d**ensity **P**oly**e**theyle
LH	**L**eft-**H**anded (reverse-conveying)
MWCNT	**M**ulti-**w**alled **C**arbon **N**anotube
PC	**P**oly**c**arbonate
PDMS	**P**oly**d**i**m**ethyl**s**iloxne (Silocone oil)
PMMA	**P**oly(**m**ethyl **m**eth**a**crylate (acrylic))
PLA	**P**oly**l**actic **A**cid
PVP	**P**oly(**v**inyl**p**yrrolidone)
RH	**R**ight-**H**anded (forward-conveying)
RRD	**R**esidence **R**evolution **D**istribution
RSD	**R**esidence **S**tress **D**istribution
RTD	**R**esidence **T**ime **D**istribution

RVD	**R**esidence **V**olume **D**istribution
SEM	**S**canning **E**lectron **M**icroscope
SSE	**S**ingle-**S**crew **E**xtruder
TiO_2	**T**itanium Di**o**xide
TSE	**T**win-**S**crew **E**xtruder
XRD	**X**-**r**ay Powder **D**iffraction

Symbols

$\%BU$	percent break-up	$\%$
$\%deg$	percent degradant	$\%$
$\%DF$	percent drag flow	$\%$
$\%RH$	relative humidity	$\%$
A	partially-filled coefficient	rev
B	fully-filled coefficient	mL
D	cluster diameter	μm
D_s	screw diameter	mm
Fa	fragmentation number	
F_d	shape factor	
H	screw channel height	mm
k"	erosion rate constant	
L/D	length-to-diameter ratio	mm/mm
M	dimensionless cluster mechanical properties	
$\dot{m}$	feed rate	g/min or kg/hr
n	screw lobes	
N	screw speed	RPM
Q	volumetric throughput	mL/s
Q/N	specific throughput	mL/rev
$Q/N_{100\%}$	100% specific throughput	mL/rev
R	cluster radius	μm

R^2	coefficient of determination	
R_{mean}	mean revolutions	rev
T_b	barrel temperature	°C
t_{mean}	mean residence time	min or s
T_{melt}	melt temperature	°C
V_{mean}	mean volumes	mL
W	screw channel width	mm
W_a	work of adhesion	mJ/m^2
$wt\%$	weight percentage	$\%$

α	statistical significance level	
$\dot{\gamma}$	shear rate	s^{-1}
μ	dynamic viscoity	Pa-s
π	physical constant	
σ_c	cohesive strength	Pa
ξ	dimensionless cluster radius	
τ	shear stress	Pa or kPa
ϕ	helical angle	degrees (°)
Ω	dimensionless cluster yield strength	

Chapter 1

Introduction

Twin-screw extrusion is frequently used to manufacturing polymer composites due to the flexibility of screw designs to achieve a range of mixing as well as the advantages of continuous processing. Composites are formed through twin-screw compounding, or mixing of two or more components within an extruder in order to produce a new material [1]. Typically, twin-screw compounding involves the mixing of a solid into a molten polymer, resulting in improved properties when compared to a purely polymer product. This allows for greater control over product properties and may introduce new utilities for the extruded material. By controlling the type and concentration of solid, twin-screw extruded composites can achieve improved mechanical, electrical, and thermal properties when compared to neat polymer [2–6] . In addition, twin-screw compounding has been shown to improve the optical properties of extruded products [5], as well as decrease the permeability of extruded films [6].

Typically, when solids are compounded into a polymer melt, they are introduced as clusters of particles held together with variable cohesive strengths. The mechanism for reducing cluster size is termed dispersive mixing, and the dispersive mixing capability of a twin-screw extruder (TSE) is a key reason why it is commonly selected for polymer compounding processes. The dispersibility of a solid cluster is heavily influenced by the cluster size. In this work, three size scales will be defined: primary particle, aggregate, and agglomerate. The term “cluster" will be used to refer to a solid additive of indeterminate size. Primary particles are the smallest cluster size that can occur during processing, typically as small as the nano-scale. These particles cannot be further dispersed. Aggregates are clusters of primary particles held together by strong cohesive forces and are therefore not easily dispersed. In comparison, agglomerates are a combination of weakly bonded primary particles and aggregates, and are therefore more readily dispersed. In other works, aggregates have been defined as “dense agglomerates” or “hard agglomerates” whereas agglomerates have been termed “sparse agglomerates” or “soft agglomerates” [7, 8]. In twin-screw compounding, aggregates and agglomerates are the primary cluster sizes of interest because their size can be reduced. The exact sizes defining primary particles, aggregates, and agglomerates are a function of the solid and the compounding process. Figure 1.1 demonstrates the relative size difference between the three cluster designations. The concentration of each scale in a composite is a function of the dispersive mixing that occurs during processing.

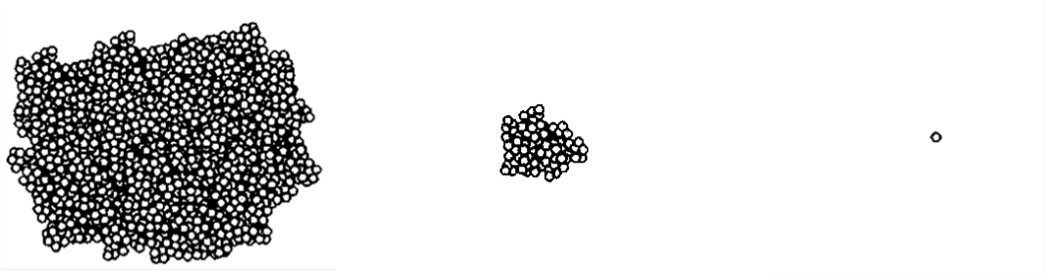

(a) Agglomerate (b) Aggregate (c) Primary Particle

FIGURE 1.1: Relative size difference between agglomerates, aggregates, and primary particles.

1.1 Motivation

The degree of dispersive mixing in a polymer composite has been demonstrated to affect the final product properties due to the reduction in the size of the solid clusters. Song and Youn determined the effect of multi-walled carbon nanotube (MWCNT) dispersion on the material properties of an epoxy composite by directly comparing well-dispersed and poorly dispersed composites. Results indicated that the well-dispersed samples had superior electrical and thermal conductivity as compared to the poorly dispersed samples. Additionally, the elongation at break and the tensile strength of the well-dispersed composites were superior [2]. Similarly, using a twin-screw microcompounder to compound MWCNT with polycarbonate, Kasaliwal et al. improved the dispersive mixing by increasing the screw speed, leading to significantly higher electrical conductivity in the composites [3]. Mayoral et al. confirmed the same property response using a twin-screw extruder to compound MWCNTs into polypropylene [9].

When compounding solid pigments, sufficient dispersion ensures exceptional optical

quality of the final product. During film extrusion of TiO_2 compounded into high-density polyethylene (HDPE), poor dispersion of the TiO_2 has been shown to cause optical imperfections [10]. Lee et al. showed that in linear low-density polyethylene (LLDPE) and TiO_2 films, increasing the total shear time lead to improved gloss as a result of fewer large clusters protruding from the surface [5]. In order to achieve these improvements in properties, dispersive mixing in a compounding process needs to be measured and controlled.

Twin-screw compounding has also shown great potential in the pharmaceutical field, where is has clear advantages over alternative processes. The continuous mixing in a TSE enables the creation of solid solution where a solid active pharmaceutical ingredient (API) is dissolved in a water-soluble polymer carrier, resulting in molecular dispersion of the API [11]. Molecular dispersion minimizes the size of the API, leading to improvements in the drug bioavailability, or the amount and rate of API absorption once ingested [12–14]. Due to the increased efficiency of absorption, a lower concentration of API is required. In addition, the continuous twin-screw extrusion process allows for greater processing efficiency than the more common batch processes for pharmaceutical manufacturing.

Even with these benefits, twin-screw compounding is used infrequently to manufacture pharmaceuticals today, due to adverse properties induced by the extrusion process. During extrusion, APIs can degrade into ineffective or dangerous forms, and if the degradation is significant, extrusion may not produce a safe or viable product. In addition, the extrusion process can introduce water into the final composite that may lower the glass

transition temperature of the polymer carrier, reducing its viscosity and destabilizing the API. If the API destabilizes, the solubility of the drug will decrease and the dosage will vary. In order to successfully extrude a commercial drug, the response of pharmaceutical properties to operating conditions needs to be determined. This will allow for the design of an appropriate twin-screw extrusion operating domain and evaluation of any property trade-offs.

Typically, industrial development of a pharmaceutical extrusion process focuses on determining a viable set of operating conditions without considering the physical mechanisms that affect the property response. However, the effect of operating conditions implies significant physical mechanisms that induce changes in pharmaceutical properties. By identifying the significant physical mechanisms, such as time, temperature, and stress, the property response can be universally developed independent of extruder size. Previous studies have investigated the effect of time and temperature on bioavailability, water content, and degradation, however, there is little experimental work examining the effect of stress on these pharmaceutical properties. Due to its influence on mixing within a TSE, it is likely that the stress developed during processing influences the property response.

1.2 Objective

The objective of this thesis is to apply the Residence Stress Distribution (RSD) methodology to model the stress behavior and property response of twin-screw compounding

processes as a function of the operating conditions. In addition, the significance of physical mechanisms, such as the stress, will be related the dispersion behavior of a solid pigment as well as the property response of an API during compounding. These objectives were investigated with two twin-screw compounding processes each producing a unique composite product. The first process was the compounding of a solid, agglomerated pigment into a polyethylene. The second process was the pharmaceutical extrusion of a weakly soluble API with a water-soluble polymer. The research goals with both processes are outlined below:

1. *Establish the dispersive mixing behavior of a solid cluster within a liquid polymer flow.*

   Through rheological experiments, simplified flow analysis of cluster dispersion is investigated. The relationship between the flow and dispersion behavior is evaluated through analysis of the size distribution of the clusters. This analysis indicates the primary modes for dispersion and the effect of the flow on cluster size. These relationships give insight into the dispersion behavior of a cluster within a twin-screw compounding process, and will help guide the design of screw geometries and suitable operating conditions.

2. *Develop the relationship between extruder operating conditions and dispersive mixing potential.*

   Twin-screw compounding processes are directly controlled by changing the extruder operating conditions. Adjusting the operating conditions induces changes in the melt flow, resulting in unique flow behavior. The physical effects of changing operating conditions are related to the dispersion behavior of solid clusters to determine the effect of operating conditions on the final size distribution of the solid clusters. By developing this relationship, operating conditions can be determined to maximize dispersion of the solid clusters in a composite, and hence achieve desired improvements in properties.

3. *Determine the property response of a pharmaceutical extrusion process.*

   Pharmaceutical extrusion processes require consideration of property trade-offs that may result in an unsafe or ineffective drug. Across a range of operating conditions, the pharmaceutical property response is evaluated to determine a suitable operating domain when considering these trade-offs. The response of properties to changes in operating conditions also indicates the physical relationships that have the most significant effect on the properties. This insight will allow for intuitive process design and control over a pharmaceutical extrusion process.

4. *Investigate the physical mechanisms that induce changes in pharmaceutical property response.*

   While operating conditions directly control the flow with a TSE, they do not directly indicate the physical mechanisms changing the property response. During the pharmaceutical extrusion experiment, physical parameters were measured at every set of operating conditions. These parameters are evaluated against property response in order to determine the physical significance behind the changes in operating conditions. The predictive accuracy of these parameters is compared against operating condition relationships to determine the utility of each approach.

Chapter 2

Background

2.1 Twin-Screw Extrusion

In the processing of polymer composites, twin-screw extrusion provides several benefits over alternative processing methods. Extrusion, whether single- or twin-screw, allows for continuous manufacturing, which decreases total production time and reduces inconsistencies in the product. Twin-screw extrusion in particular allows for intensive mixing of the molten polymer due to the intermeshing elements on each screw. The intermeshing elements on a twin-screw extruder (TSE) induce stress and strain on the melt, which can improve the quality of mixing. Single-screw extruders (SSE) are generally limited by the stress and strain induced by the screws dragging the melt against the barrel wall and the pressure developed by the pumping of the screw. While these actions are present in TSEs, the interaction between adjacent screw elements leads to

higher forces than typically achievable with a SSE. In addition, TSE screws are often comprised of individual, unique screw elements that can be selected and arranged to alter the flow development. Due to its mixing capability and adaptability, twin-screw extrusion is commonly used to compound solids into a neat polymer. The compounding of one or more materials into a molten polymer significantly affects the overall properties of the melt [2–6], with the final properties dependent upon the degree of mixing achieved during processing [2, 3, 5, 9, 10].

2.1.1 Extruder Geometry

Twin-screw extruder screws can either rotate in the same direction (co-rotating) or in alternate directions (counter-rotating). Co-rotating TSEs are able to achieve higher speeds and outputs than counter-rotating TSEs, making them ideal for compounding [15]. Screw elements on co-rotating TSEs can be fully intermeshed, resulting in a self-wiping behavior that prevents overheating of stagnant melt [16]. The elements on a TSE are modularly built along a screw shaft, allowing for customization of a screw to satisfy processing requirements. There are several different types of screw elements used in twin-screw extrusion, but only conveying elements and kneading blocks will be discussed.

2.1.1.1 Conveying Elements

Conveying elements are rounded channels angled to convey material either downstream towards the die (forward conveying) or upstream towards the material feed source (reverse conveying). Material is conveyed by the rotation of the conveying elements dragging the melt against the barrel wall, inducing flow along the angled channels. The angle of the channels determines the pitch of the element, or how far material travels axially with one revolution of the element. With every revolution, wide-pitched elements will convey material longer axial distances than narrow-pitched elements. As a result, narrow-pitched elements have less volume per screw channel. Examples of wide- and narrow-pitched elements are shown in Figure 2.1. Reverse conveying elements are angled against the conveying direction and are typically used to build up pressure in region, fully-filling a length of upstream elements.

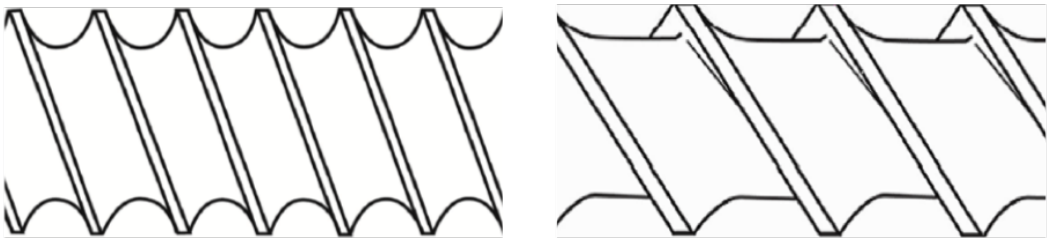

(a) Narrow-pitched (b) Wide-pitched

FIGURE 2.1: Narrow- and wide-pitched conveying elements [17].

Conveying elements are labeled with the convention: pitch/axial length, followed by the conveying direction for the element. For example, a forward conveying element with a 24 mm pitch and a 24 mm axial length would be labeled 24/24RH, with the ”RH” indicating right-handed, or forward conveying.

2.1.1.2 Kneading Blocks

Kneading blocks (KBs) are made up of staggered disks that split and squeeze the flow. The disks are typically offset at an angle to either convey material upstream or downstream. Neutral KBs have a 90° offset angle that prevents conveying action in either direction. Similar to reverse elements, neutral KBs build-up pressure and create a filled length of elements. Forward conveying and neutral KBs are shown in Figure 2.2. Using the axial length and number of paddles, the width of a KB paddle can be determined. Based on paddle width, KBs are colloquially termed "narrow" or "wide" KBs, which have distinctly different mixing action.

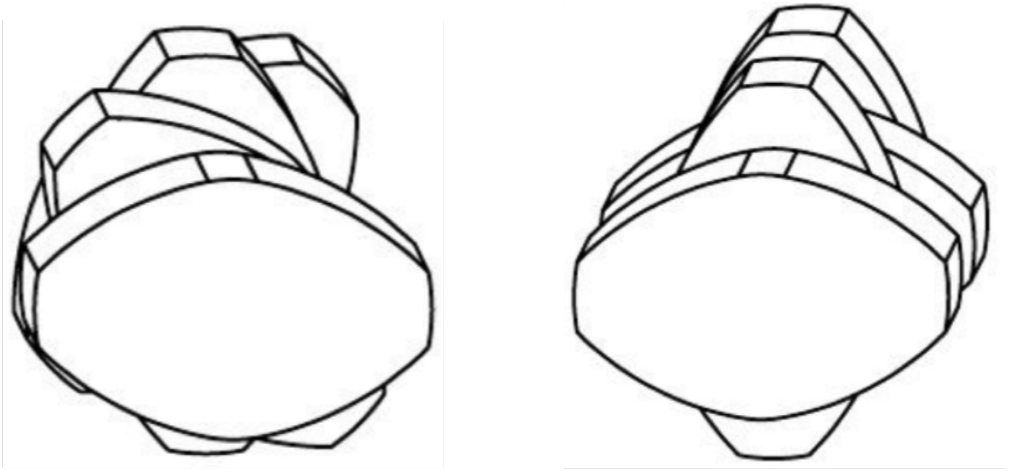

(a) Forward KB (b) Neutral KB

FIGURE 2.2: Forward and neutral kneading block elements [18].

KBs are labeled with the following convention: KB stagger angle/number of paddles/axial length - conveying direction. For example, a five paddle, reverse KB with a length of 30 mm and a stagger angle of 45° would be labeled KB45/5/30-LH.

2.1.1.3 Mixing Section

Mixing sections are regions on the screw geometry where the most intensive mixing will occur. KBs are commonly used in mixing sections as the primary mixing elements, and are frequently followed by reverse conveying elements or neutral KBs. These restrictive elements create pressure flow, filling up a length of the KBs in the mixing section. Experiments considering the stress in a twin-screw compounding process will typically focus on the mixing section, due to the relative magnitude of the stress generated in that region.

2.1.2 Operating Conditions

Once a screw geometry has been developed for a compounding process, an operator can alter the final product through the operating conditions. The most common operating conditions on a TSE are the screw speed (N), the feed rate ($\dot{m}$), and the barrel temperatures (T_b). The feed rate can be expressed as the throughput (Q), the volumetric flow rate through the extruder, which can be calculated with a known $\dot{m}$ and the density of the melt. The volumetric flow rate is commonly of interest due to the signficance of volume on flow behavior and mixing. The specific throughput (Q/N) is a measure of the volume conveyed per revolution.

2.2 Mixing Mechanisms

In a TSE, mixing of a solid into a molten polymer can be separated into two distinct mechanisms: distributive and dispersive mixing. Distributive mixing is the process of increasing the distance between the solids, tending towards a homogeneous melt. Dispersive mixing is the process of reducing the size of the solid filler by breaking apart or eroding the solids. These two mechanisms are displayed in Figure 2.3.

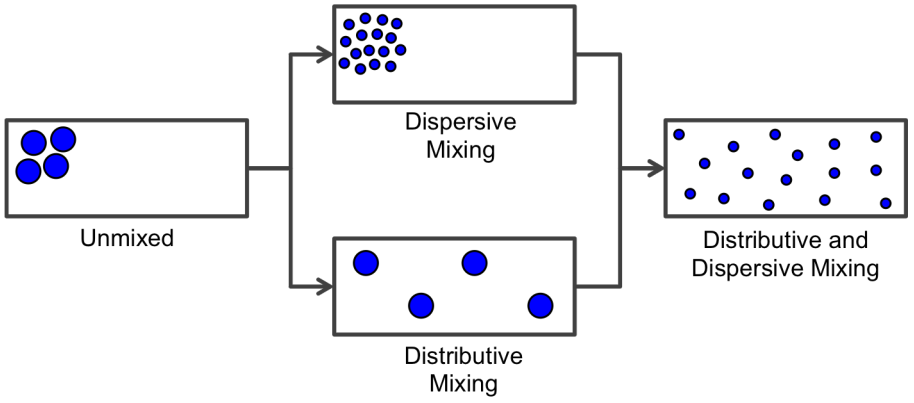

FIGURE 2.3: Distributive and dispersive mixing mechanisms. Both mechanisms are required for good mixing in twin-screw compounding.

2.2.1 Distributive Mixing

In twin-screw compounding of solids, distributive mixing can be defined as continually rearranging the solid phase in the polymer melt in order to improve the spatial homogeneity of the composite melt [19]. Distributive mixing is achieved by the screw elements splitting and recombining the polymer melt, therefore distributing the contained solids. This mixing mechanism can be characterized by the total strain the screw elements induce on the composite melt. Insufficient distributive mixing can cause local

variations in solid concentration, resulting in non-uniform or unpredictable final product properties.

The operating conditions and screw geometry of a TSE can be designed to improve the distributive mixing. Using reactive polymer tracers, Shearer and Tzoganakis investigated the effect of KB conveying direction, N, and Q on the distributive mixing behavior in a twin-screw extruder. The authors found that the screw geometry and operating conditions interact to affect distributive mixing. At high N (or high shear rates), decreasing N improves the distributive mixing for forward, reverse, and neutral KBs due to the increase in the average time material remains in the extruder (t_{mean}). However at low N, decreasing N worsened the distributive mixing of both the neutral and reverse KBs: the decrease in shear rate was more significant at low N. The fill length displayed the same relationship to screw speed and KB geometry. Both plots are shown in Figure 2.4 [20].

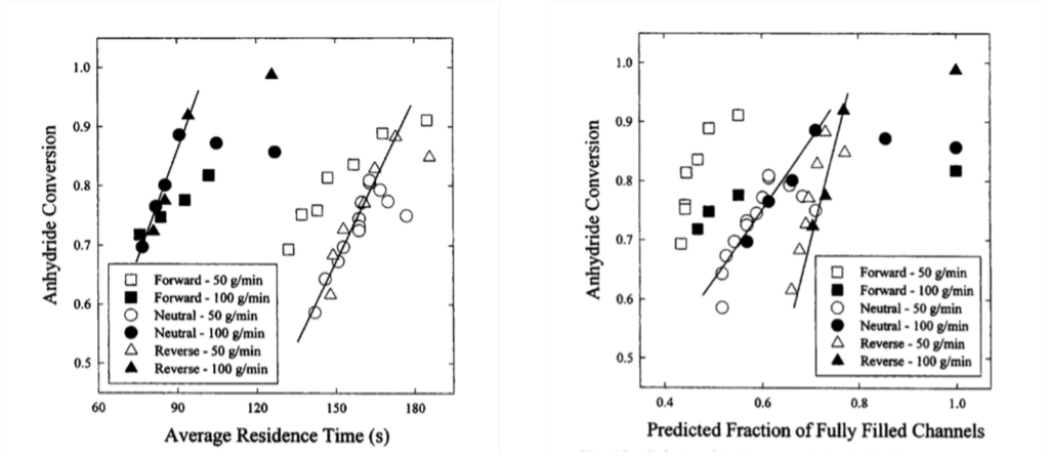

(a) t_{mean} (b) Fill length

FIGURE 2.4: Distributive mixing quality (measured by anhydride conversion) versus mean residence time and fill length for various KB orientations and feed rates [20]

Other authors have shown that reverse kneading blocks lead to the greatest distributive mixing through optical analysis of an extrudate [21] and FEM simulations [22]. This is attributed to the melt remaining in the kneading blocks for a greater number of revolutions, allowing for more straining. In twin-screw compounding, right-handed narrow kneading blocks are typically used to simultaneously convey and distribute the flow. These kneading blocks have slender paddles that split and recombine the flow. The narrow disks on these kneading blocks result in less backflow [23], which has been shown to improve distributive mixing [24].

2.2.2 Dispersive Mixing

When solids are compounded into a molten polymer, they are commonly introduced as large agglomerates and aggregates, or solid clusters held together by cohesive forces. Dispersive mixing is the process of overcoming the cohesive strength of the clusters, separating smaller aggregates and primary particles and therefore reducing the average size of the clusters. In a twin-screw compounding process, the flow field generates the stresses that induce dispersive mixing.

In a standard conveying element (Section 2.1.1.1), shear stress is generated by the rotating screw dragging the melt along the stationary barrel wall. If the channel is fully filled, the shear stress within the melt can be approximated as a simple shear flow using Equation 2.1 [1].

$$\tau = \mu \cdot \dot{\gamma} = \mu \cdot \frac{\pi D_s N}{60 \cdot H} \tag{2.1}$$

In Equation 2.1, D_s is the diameter of the screw, H is the screw channel depth, N is the screw speed, $\dot{\gamma}$ is the shear rate, and μ is the viscosity. N is divided by 60 in this equation to convert from revolution per minute to revolutions per second. Typically for a given extruder, conveying elements have the same D_s and H, regardless of pitch. Therefore in Equation 2.1 the only way to increase the shear rate in a conveying element is to increase the N. However, there are limits for N based on the maximum rotational speed and the torque limit of an extruder motor. Additionally, many polymers display shear-thinning behavior, so increasing the shear rate will decrease the viscosity, and may limit the increase in shear stress.

Due to limitations of purely conveying elements in generating stress, mixing sections are added to screw designs, commonly comprised of KB elements. Wide KBs in particular are frequently used due their wide paddles squeezing and accelerating the flow in the axial directions, producing strong shear and extensional stresses [25]. Other authors have attributed the high stresses generated by wide KBs to the flow over the KB paddles in the narrow clearance region between the paddle tip and the barrel wall [17]. This region will generate much higher shear rates, but volumetrically represents a small portion of the flow. Compared to narrow KBs, wide KBs are worse distributive mixers, but better dispersive mixers. Simulations of wide KBs have shown that the wide paddles limit recirculation, but increase the average shear rate in the flow [26].

While stress analysis in a TSE primarily considers the shear stress, there is evidence that extensional stress may also contributed to dispersive mixing. There is limited experimental work examining the effect of extensional stress on cluster dispersion during twin-screw compounding due to the difficulty in constructing a controlled extensional flow similar to the real flow in a TSE. Kao and Mason [27] discussed the difference in dispersive mixing capability between simple shear and purely extensional flows using strain rates much lower than a typical TSE flow. Figure 2.5 shows the dispersive mixing of poly(methyl methacrylate) (PMMA) spheres in silicone oil. Their results indicated a distinct difference in dispersion behavior in the two flow fields.

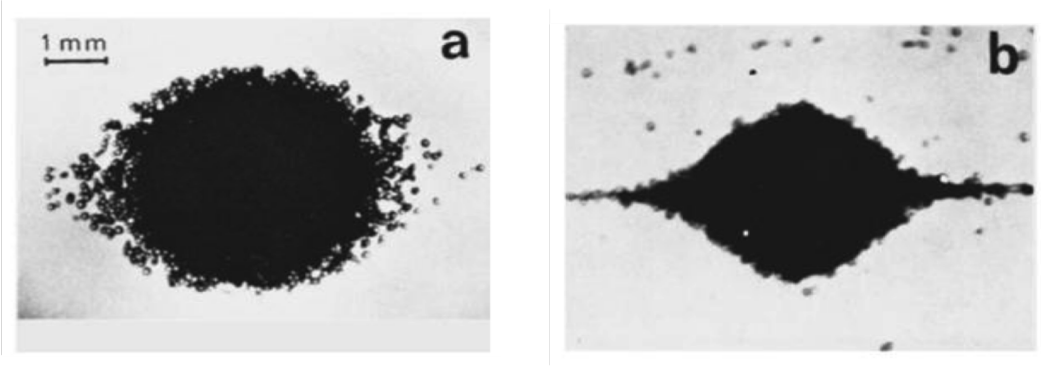

(a) Simple shear flow (b) Extensional flow

FIGURE 2.5: PMMA cluster dispersing in silicone oil under simple shear flow and extensional flow [27]

Simulations by Higashitani et al. [28] investigated the effect of simple shear and extensional flows on the total number of particles in an cluster. Results indicated that elongational flow more effectively dispersed clusters than simple shear flow. The greater dispersion efficiency has been explained by the fact that simple shear flow expends energy rotating the agglomerate instead of dispersing.

2.3 Kinematic Approaches

Due to the complex flows that develop inside a TSE, modeling and simulation of mixing is challenging. For this reason, kinematic approaches are commonly used to characterize the flow in a TSE. Kinematic approaches do not require calculation of the flow fields that develop in the machine, but instead measure the behavior of tracer particles placed within the flow.

2.3.1 Residence Time Distribution

The Residence Time Distribution (RTD) is the most popular kinematic approach used in twin-screw extrusion. An RTD measures the amount of time required for fluid particles to travel a set, axial length in a TSE. The travel time is recorded using an impulse of tracer at the beginning of the section of interest. Due to the non-uniform velocity profiles across screw channels, the initial impulse of tracer transforms into a distribution as it travels downstream. At a location downstream of the tracer injection point, a measurement system records the strength of the tracer in a local section of the flow. Typical RTD techniques use a visible dye tracer that stains the polymer melt, allowing for visual observation as well as measurement of dye concentration by reflected or transmitted light [29–32]. Newer methods use near-IR spectroscopy to quantify the color change in the stained melt [33, 34]. While light measurement methods are more common, RTDs have been measured using the magnetic susceptibility [35], electrical

conductivity [36], and surface emissivity [37] of the melt as well changes in ultrasonic signal strength [38].

The mean residence time (t_{mean}) is often used to evaluate the effect of operating conditions on the RTD. The t_{mean} represents the mean travel time for the tracer particles used to measure the RTD. Kao and Allison investigated the effect of N, Q, and T_b on t_{mean} and found that only N and Q significantly affected t_{mean}. With all other factors constant, increasing both N and Q independently resulted in decreases in t_{mean} [39]. The results for t_{mean} versus N and Q are displayed in the two plots in Figure 2.6.

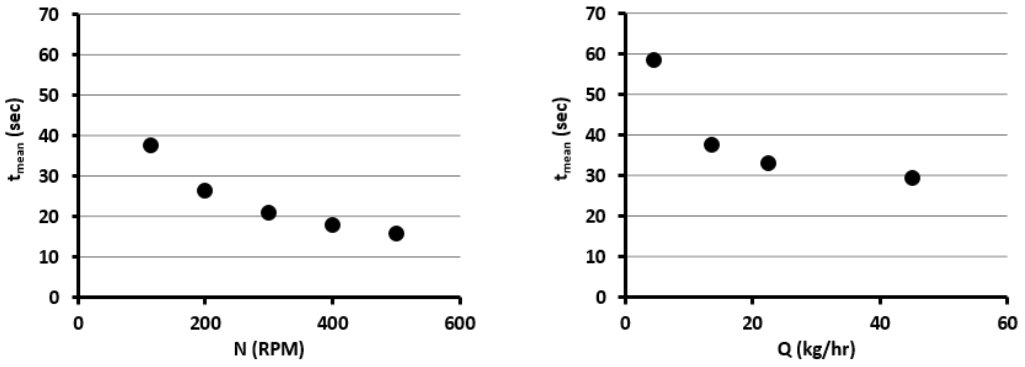

(a) t_{mean} versus N (constant Q = 13.6 kg/hr)

(b) t_{mean} versus Q (constant N = 155 RPM)

FIGURE 2.6: The effect of N and Q on t_{mean} [39]

Other authors have confirmed the significance of N and Q on t_{mean} [40, 41] and investigated the effect of additional parameters. Altomare et al. examined the effect of N, Q, T_b, screw geometry, moisture content, and die diameter on t_{mean} during a twin-screw extrusion cooking process. In addition to N and Q, the authors found that the introduction of more kneading blocks in the screw geometry significantly increased t_{mean}. The other factors were found insignificant [40]. While the majority of the literature indicates that t_{mean} is not affected by T_b, some authors have found t_{mean} to decrease as the T_b is

increased [42, 43]. Gautam et al. investigated the difference in t_{mean} between screw geometries containing either KBs or reverse conveying elements in a polypropylene twin-screw extrusion process. The reverse conveying elements resulted in even larger t_{mean} than the KB geometries [44].

2.3.2 Residence Revolution and Residence Volume Distributions

Using t_{mean} results from several authors, Gasner et al. plotted regression lines as a function of N and Q. The basic form of the regression equation is shown in Equation 2.2 [45].

$$t_{mean} = \frac{A}{N} + \frac{B}{Q} \tag{2.2}$$

In Equation 2.2, the coefficient A is determined by the geometry of the partially-filled section of the extruder screw while B is determined by the geometry of the fully-filled section. This equation can be used to predict the t_{mean} with changes in N and Q, assuming a constant screw geometry.

Gasner et al. also used the regression equation to transform from the time domain to the revolution and volume domains. By multiplying both sides of Equation 2.2 by N, the equation transforms into a linear equation for t_{mean} times N, or the mean number of residence revolutions (R_{mean}). R_{mean} represents the average number of revolutions

required for particles to travel the tested axial length. The transformed R_{mean} equation is shown in Equation 2.3.

$$R_{mean} = A + B\left(\frac{N}{Q}\right) \tag{2.3}$$

By multiplying both sides of Equation 2.2 by Q the equation becomes a linear function for t_{mean} times Q, or the mean number of residence volumes (V_{mean}). V_{mean} represents the average amount of displaced volume required for particles to travel the test length. The transformed V_{mean} equation is shown in Equation 2.4.

$$V_{mean} = A\left(\frac{Q}{N}\right) + B \tag{2.4}$$

The equations for R_{mean} and V_{mean} both depend on a single variable, Q/N (or Q/N inverse). The variable Q/N is the specific throughput, or the volume of material conveyed per revolution of the screw. Using these relationships, Gasner et al. replotted t_{mean} data (Figure 2.6) as a function of Q/N and its inverse to display the linear trends of R_{mean} and V_{mean}. These plots are recreated in Figure 2.7 [45].

The plots in Figure 2.7 are both strongly linear ($R^2 > 0.99$). The intercept and slope terms in both regression equations are similar, representing the same geometric coefficients A and B seen in Equation 2.3 and 2.4.

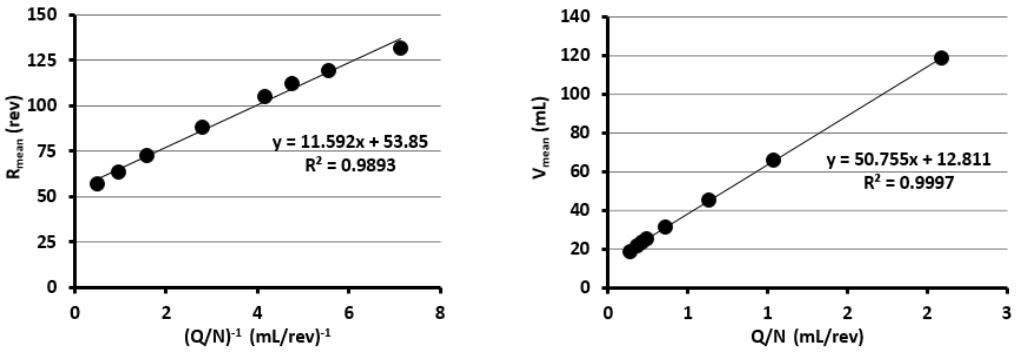

(a) R_{mean} versus $(Q/N)^{-1}$

(b) V_{mean} versus Q/N

FIGURE 2.7: Experimental t_{mean} data transformed into R_{mean} and V_{mean} as a function of Q/N inverse and Q/N.

While Gasner et al. demonstrated the significance of Q/N on the R_{mean} and V_{mean}, Gao et al. transformed entire RTDs to determine the effect of Q/N on the residence revolution distribution (RRD) and residence volume distribution (RVD) [31]. The RRD and RVD were determined by applying the transformations shown in Equation 2.3 and 2.4 to the entire distribution. The RTDs were collected on a 30 mm extruder with HDPE at varying N and Q, and tracer concentrations were recorded with reflective optical probes. All RTDs are shown in Figure 2.8, with the legend in the center of the graph indicating the operating conditions for each numbered curve. The individual curves are difficult to distinguish, indicating distinctly different RTDs among the 12 conditions.

The RTDs were transformed into RRDs by multiplying the time for each curve by the N at each condition, as shown in Figure 2.9. In this new domain, there are groupings of curves that have the same distribution. These overlapping curves (1, 7, 11 and 2, 8, 12) have different N and Q values, but the same Q/N. This indicates that at equivalent Q/N, the tracer particles follow the same path through the extruder.

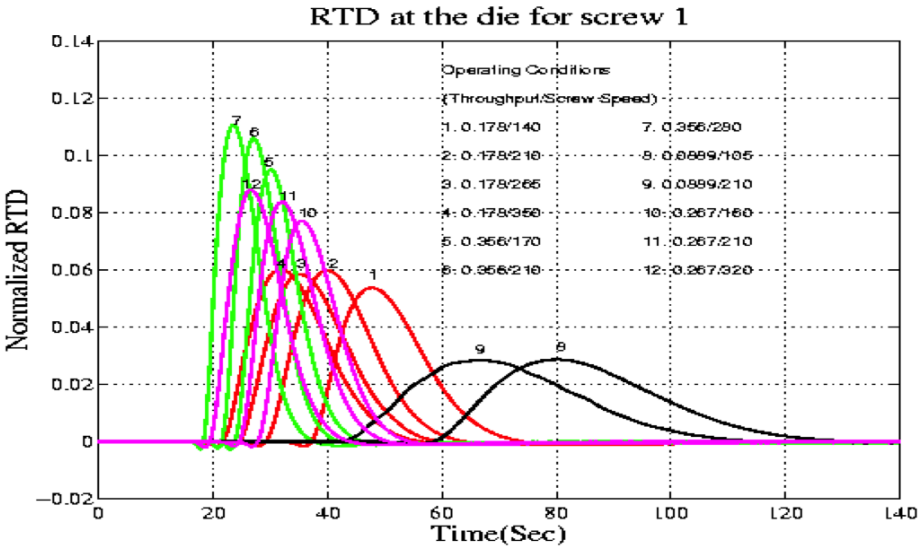

FIGURE 2.8: RTDs collected by Gao et al. on a 30 mm extruder with HDPE. Distributions for 12 different sets of N and Q operating conditions were collected [31]

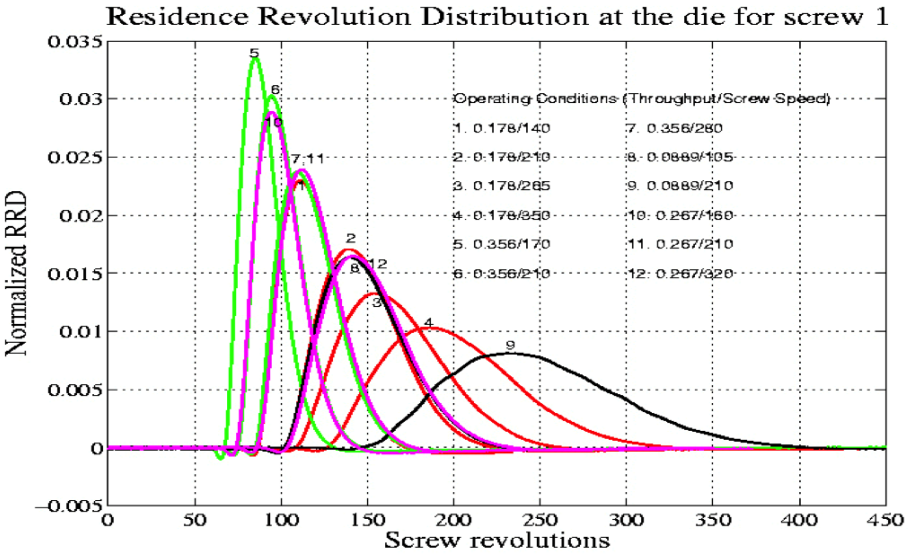

FIGURE 2.9: RTDs transformed in RRDs. Conditions with equivalent Q/N have the same distribution [31].

The transformed RVDs are shown in Figure 2.10. In the residence volume domain, curves with equal Q/N overlap. In this domain, matching RVDs indicate equivalent axial mixing profiles, or the same number of conveyed volumes.

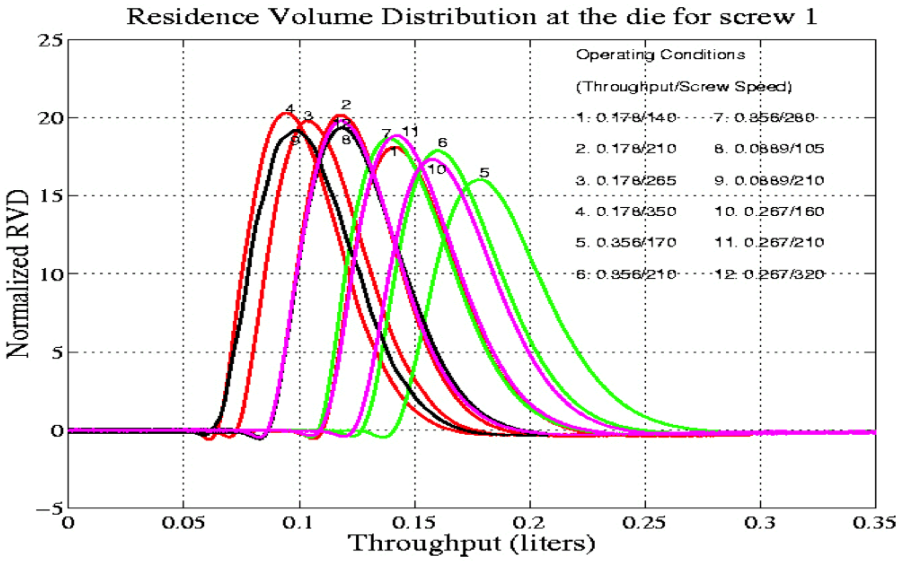

FIGURE 2.10: RTDs transformed in RVDs. Conditions with equivalent Q/N have the same distribution [31].

The significance of Q/N on RRDs and RVDs was also confirmed theoretically and experimentally by Zhang et al. [46]. Elkouss et al. investigated the effect of material on RVDs. With primarily viscous polymers, the authors found the RVD did not change significantly with different viscosity materials, even with non-Newtonian behavior. However, with strongly elastic polymers, the RVDs did not overlap at equivalent Q/N, and the material properties had a significant effect [47].

2.3.2.1 Percent Drag Flow

Using the RRD and RVD, the significance of Q/N on particle path and axial mixing profile was established. However, in these experiments, the screw geometry and extruder scale were held constant. With different screws and extruder geometries, the volume conveyed per revolution can be expressed non-dimensionally for each element

filled with material. The percent drag flow ($\%DF$) is a measure of the percentage of volume conveyed per revolution compared to the maximum pumping capacity of an element. The pumping capacity of an element is maximum volume conveyed per revolution $(Q/N)_{100\%}$ before pressure develops. Below 100% drag flow, the screw channel is partially-filled and the flow is driven by the screw dragging the melt against the barrel wall. This relationship is shown in Equation 2.5.

$$\%DF = \frac{\frac{Q}{N}}{\left(\frac{Q}{N}\right)_{100\%}} \tag{2.5}$$

In Equation 2.5, the Q/N is determined by the operating conditions for the extruder. The $(Q/N)_{100\%}$ can be predicted theoretically [48–50] or calculated experimentally [51, 52]. The simplified form of the theoretical $(Q/N)_{100\%}$ equation is shown in Equation 2.6.

$$\left(\frac{Q}{N}\right)_{100\%} = \frac{2n-1}{2}\pi D_s W H cos(\phi) F_d \tag{2.6}$$

In Equation 2.6 n is the number of lobes in the extruder, D_s is the diameter of the screw, W is the width of the screw channel, H is the height of the channel, ϕ is the helical angle, and F_d is a shape factor that accounts for the restricting effect of screw flights on the flow between infinite parallel plates. Typically, the variables n, D_s, and H are constant for all elements on a given twin-screw extruder. The variables W, ϕ, and F_d will change depending on the type of element (conveying, kneading block, etc.)

or the pitch of the element. Combining Equation 2.6 with Equation 2.5 shows that unique elements in a twin-screw geometry will have different $\%DF$. Elements with more pumping capacity (a larger pitch) can convey more volume per revolution than smaller-pitched elements. The Q/N, and hence $\%DF$, has been shown previously to dictate the particle paths and axial mixing in a TSE through the RRD and RVD analysis. Furthermore, increasing $\%DF$ has been experimentally shown to increase the length of a fully-filled region resulting from a reverse or neutral conveying element [53, 54]. By maintaining equivalent $\%DF$ and fill length, particles will travel the same path through an extruder regardless of the extruder size.

2.4 Residence Stress Distribution

Due to its effects on product properties, the dispersion in a TSE is a key parameter to consider when designing and controlling a compounding process. As discussed, the hydrodynamic stress developed in a TSE is one of the most significant factors affecting the dispersion behavior of compounded solids. While the RTD is commonly used to quantify mixing quality, it does not represent the magnitude of the hydrodynamic stresses developed in the melt. Curry and Kiani developed a direct measure of the stress in a TSE by introducing hollow glass spheres into a polybutene matrix. The glass beads had predetermined failure strength so the percent rupture during processing indicated the stress level developed in the TSE. In their first experiment, the authors evaluated the

effect of screw geometry on the rupture of the glass beads. Comparing neutral conveying KBs and reverse conveying elements, the authors found that the reverse conveying elements broke more glass beads [55]. In their second experiment, the authors examined the effects of material viscosity and bead failure strength on the rupture of the glass beads. By maintaining constant Q and increasing N, the results showed that the increases in resulted in a higher percentage of broken spheres [56].

The experimental procedure follow by Curry and Kiani was an off-line method, requiring post-processing of the extruded materials to analyze stress history. In addition, the experiment required manual counting of the broken spheres, a time consuming and error-prone practice. To counter these limitations, Bigio et al. developed the Residence Stress Distribution (RSD), a continuous, kinematic measure of stress history in a TSE. The RSD method utilizes polymeric beads with known failure strength, filled with a colorful dye. During a polymer extrusion process, the stress beads are injected into the melt and a percentage break as they experience their critical stress. As the beads break they release the encapsulated dye, staining the surrounding polymer melt. The percentage of broken beads, or the percent break-up ($\%BU$), is quantified by the intensity of the stained polymer, which is measured by a reflective light probe. This $\%BU$ metric represents the percentage of the material in a TSE process that experiences the critical strength of the stress beads [57].

In the first RSD study, Bigio et al. investigated the effect of N and Q/N on the $\%BU$. These operating conditions were chosen due to their predicted significance on the stress history in a TSE. The N influences the shear rate in the melt, which directly affects

the developed shear stress as seen in Equation 2.1. The Q/N, or the non-dimensional $\%DF$, dictates the particle paths through the extruder and the fill length in the mixing section. The authors found that increases in N and Q/N both significantly increased the $\%BU$. The interaction term, Q, and the second order terms for N and Q/N were all found to be statistically insignificant [57].

Successive experiments have established the validity of the RSD experiment to measure stress history in a TSE. Pappas et al. and Fukuda et al. evaluated the $\%BU$ response with different bead critical strengths [58, 59]. Both sets of authors confirmed the significance of N and Q/N on the $\%BU$ of all evaluated bead strengths. Bigio et al. expanded the range of N and Q/N operating conditions beyond the standard operating domain and confirmed the same $\%BU$ trends [60].

2.5 Applications of the Residence Stress Distribution

Due to the significance of stress on dispersion, several works have used the RSD method to predict and evaluate the stress generated in a compounding processes. Fukuda et al. used the RSD experiment to quantify the stress generated by different mixing section screw geometries. Results confirmed the established theory that wide KBs generate higher stress than narrow KBs, and are therefore more efficient dispersive mixers. In addition, increasing the length of KB elements resulted in higher $\%BU$ values [61]. Fukuda et al. and Dryer et al. evaluated the scale-up of operating conditions between

three extruder sizes using the RSD method, with a goal of maintaining equivalent dispersive mixing performance across all extruders. Results showed that maintaining equivalent N and $\%DF$ across all sizes led to the most similar $\%BU$ behavior [51, 59].

While several works have used the RSD experiment to determine the effect of operating conditions on stress, these experiments do not consider the mechanisms for dispersive mixing induced by increasing the hydrodynamic stress. In addition, the RSD experiment has not been previously applied to determine the significant factors affecting other product properties and the relationship between stress and property response. In the following section, the physics of dispersion will be detailed in order to clarify the effect of stress on the cluster size distribution within an extruded composite. This will be followed by a discussion of properties resulting from twin-screw compounding of pharmaceuticals, and the significant factors affecting their response.

2.5.1 Dispersion Modes

Sufficient dispersive mixing, or dispersion, of a solid during compounding has been shown to improve mechanical, electrical, and thermal properties of extruded composites when compared to poorly dispersed composites [2, 3, 9]. In addition, well-dispersed pigments result in fewer optical imperfections and higher gloss [5, 10]. The RSD experiment can be used to measure the dispersive mixing potential of a compounding process

and select the operating conditions and screw geometries to increase dispersion. However, in order to relate the results from the RSD experiment to the dispersion of a solid cluster, the physics behind dispersion needs to be developed.

The occurrence of dispersive mixing is predicted by the Fragmentation number, Fa. The Fa number is the relationship between the hydrodynamic stresses in the flow and the cohesive strength of the clusters, as defined in Equation 2.7.

$$Fa = \frac{5}{2}\frac{\mu\dot{\gamma}}{\sigma_c} \tag{2.7}$$

In Equation 2.1, the hydrodynamic stress has been represented as the shear stress in a viscous fluid, which is the product of μ and $\dot{\gamma}$. The cohesive strength (σ_c) varies as a function of cluster properties. At high Fa numbers, the dispersion is likely to demonstrate abrupt rupturing, or fracturing into two or more large clusters. At lower Fa numbers, the dispersion is more likely demonstrate gradual erosion, or the shedding of small aggregates and primary particles. At sufficiently low Fa numbers, the cluster will not disperse [62].

2.5.1.1 Rupture

Early analysis of dispersion behavior primarily investigated the rupture mode. By limiting analysis to rupture, many authors simplified the dispersion of a cluster to the splitting into two equal sized aggregates or agglomerates, each equal to half the volume of

the original cluster. Using this simplification, Adler and Mills evaluated the rupturing of spherical, porous clusters in a simple shear flow. Their analysis highlighted the effect of cluster radius on its critical shear strength, or the yield stress for each cluster size. Figure 2.11 compares cluster critical strength (Ω_c) against dimensionless radius, ξ. Each curve on the plot represents a cluster with different mechanical properties. The mechanical properties are expressed as a single variable, M, representing a combination of the Lamé constants for the porous solid. At all evaluated mechanical properties, decreases in dimensionless radius increased the yield stress of the cluster [63].

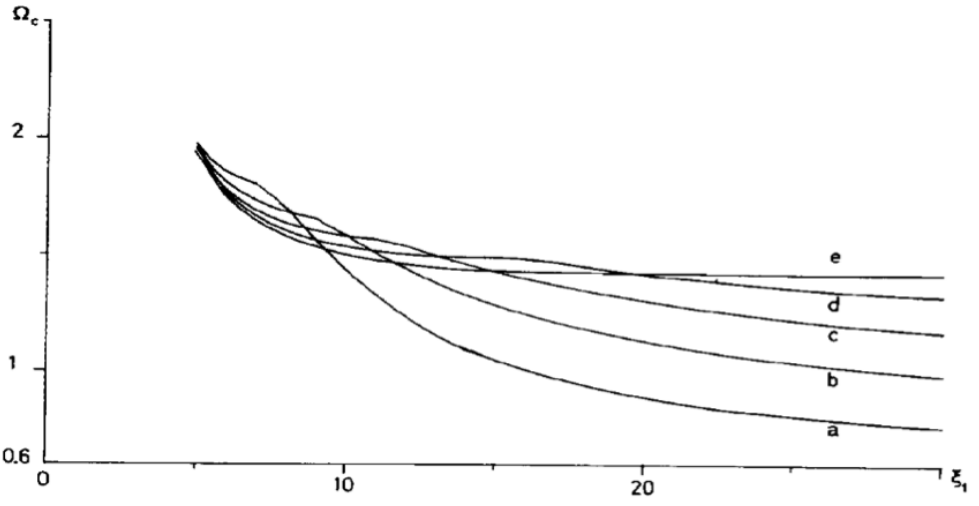

FIGURE 2.11: The yield strength of a porous solid versus the radius at several values of M: (a) = -0.75; (b) = 0.5; (c) = -0.25; (d) = 0.0; (e) = 0.25 [63]

Using similar assumptions, Manas et al. modeled the dispersion of clusters in the high shear regions of internal batch mixers. Similar to Equation 2.7, the authors developed a ratio between hydrodynamic and cohesive forces. The ratio was not a function of cluster size, but was proportional to the diameter of the aggregates that made-up the larger agglomerates [64]. Sonntag and Russel experimentally measured rupture using a

Couette rheometer to evaluate existing rupture models. They found that models failed to account for the non-uniform density of clusters, with density decreasing radially away from the center [65].

Although these models predict only the rupture of a cluster, dispersion in a TSE is a typically a combination of rupture and erosion. Bohin et al. distinguished between dispersion behaviors through fragment diameter distributions. Using a cone and plate rheometer, a single silica agglomerate was dispersed into silicone (PDMS) at various shear rates, resulting in a size distribution for the dispersed aggregates and the parent agglomerate. Figure 2.12 shows the size distribution for the aggregates and agglomerate (termed fragments) at two different shear rates and approximately the same shearing time. At the higher shear rate, the parent agglomerate is completely dispersed, indicating rapid rupturing. At the lower shear rate, the parent agglomerate was still present [8]. Rwei et al. distinguished between erosion and rupture using the resultant cluster radius distribution from a dispersed sample. Their results indicated that for erosion, the distribution is similar to the right-half of a Gaussian distribution. Conversely, for rupture the authors expected a more heterogeneous distribution [66].

Result by Bohin et al. and Rwei et al. indicate that the rupture mechanism results in smaller cluster sizes than erosion, making it the ideal dispersion technique. However as the size of the agglomerates and aggregates decreases, their cohesive strengths increase, decreasing the Fa number and increasing the probability of solely erosion [67, 68]. Rupture and erosion are not mutually exclusive processes; in most instances of rupturing, erosion occurs concurrently.

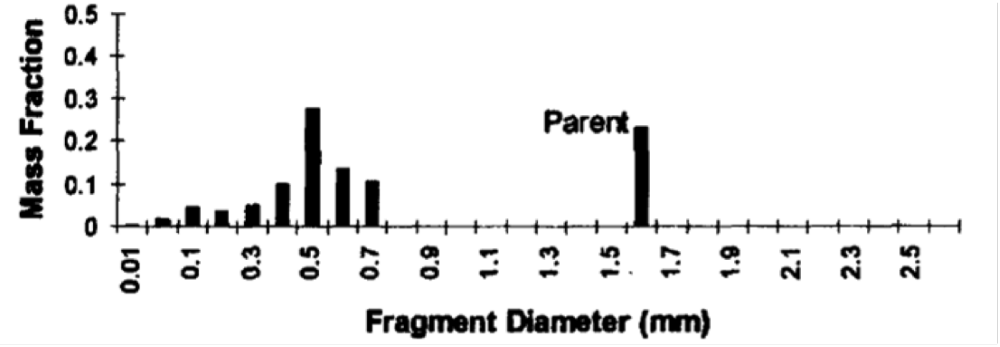

(a) $\dot{\gamma}$ = 57.1 s^{-1}, t = 0.215 s

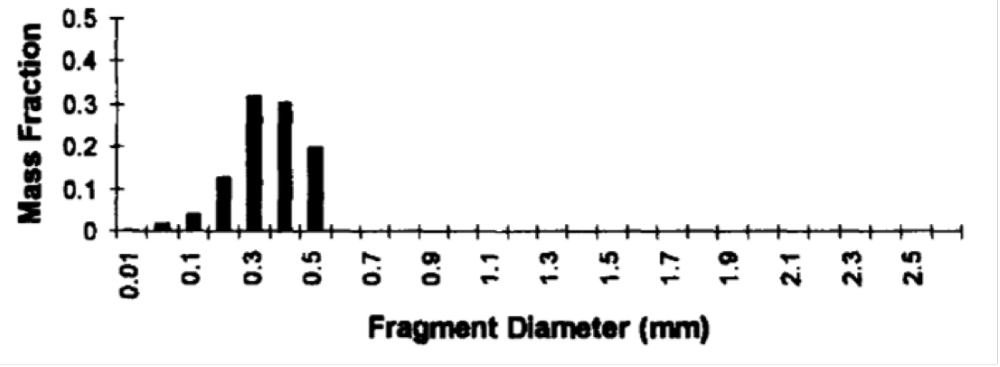

(b) $\dot{\gamma}$ = 126.8 s^{-1}, t = 0.2 s

FIGURE 2.12: The cluster size distribution of silica in PDMS at two shear rates [8].

2.5.1.2 Erosion

Several authors have predicted the erosion of a single cluster as a linear function of time. The previously mentioned work by Rwei et al. predicted the erosion of a single carbon black cluster to be a function of time (t), shear rate ($\dot{\gamma}$), and a linear fitting constant (k). The authors saw good agreement with experimental data below the perceived occurrence of rupture [66]. Lee et al. expanded upon this equation by splitting the constant k into variables for the work of adhesion (W_a), the cohesive strength of the cluster (σ_c), the fluid viscosity, and a new erosion rate constant (k''). The equation is shown in Equation 2.8, with R representing the radius of the cluster with an initial radius R_0

[5, 69].

$$\frac{R_0 - R}{R_0} = \frac{k''}{\sigma_c} W_a \mu \dot{\gamma} t \tag{2.8}$$

Other authors have created models predicting the rate of erosion over time by expanding the relationship between hydrodynamic stresses and cohesive strength. These models predict that larger differences between the hydrodynamic stresses and the cohesive strengths (or increasing Fa numbers) induce faster rates of erosion [8, 68]. These models can also predict the relationship between erosion rate and the size of the cluster. At a constant hydrodynamic stress, the cluster will erode, increasing the cohesive strength and decreasing the erosion rate. This behavior was experimentally observed by both Scurati et al. and Boyle et al. for silica clusters in PDMS. Figure 2.13 shows experimental results collected by both sets of authors for the change in radius of single cluster over time using different viscosities of PDMS yet maintaining the same average shear stress. As the dispersing time increases, the change in cluster size decreases, indicating an increase in cohesive strength with constant hydrodynamic stress [68, 70]. Theoretical models and experimental results for erosion indicate that at constant hydrodynamic stress, there is a critical radius at which clusters will no longer disperse

Another apparent conclusion from Figure 2.13 is the influence of time on dispersion. With both results, the cluster radius continued to decrease over time albeit with decreasing rates. This would appear to indicate a direct correlation between dispersion and time that varies with the viscosity of the dispersing fluid. However, when both

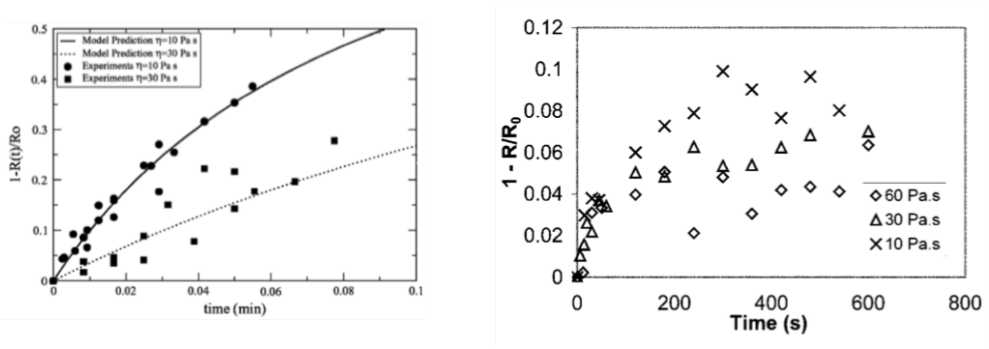

(a) Scurati et al. [68] (b) Boyle et al. [70]

FIGURE 2.13: Cluster size over time with different viscosity PDMS at the same shear stress [68, 70].

data sets are converted to total strain instead of total time (Figure 2.14), the different viscosity curves fall on the same line. This shows that dispersion is directly correlated with total strain, not elapsed time. The significance of total strain was also observed by Komoda et al for silica agglomerates in EMMA [71].

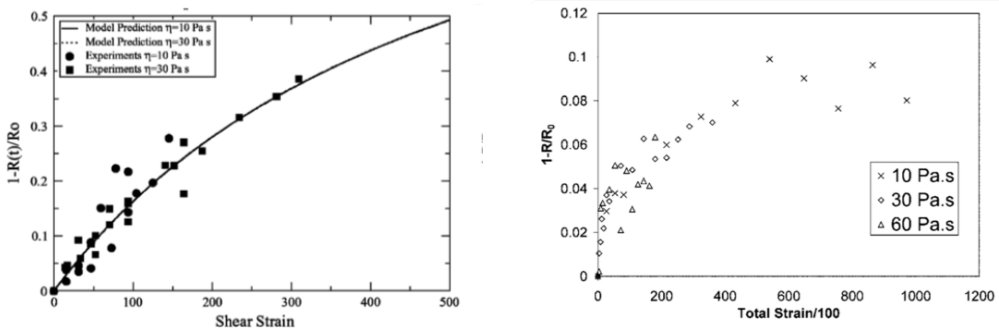

(a) Scurati et al. [68] (b) Boyle et al. [70]

FIGURE 2.14: Cluster size versus total strain with different viscosity PDMS at the same shear stress [68, 70].

While processing parameters such hydrodynamic stress and total strain have been shown to affect dispersion, characteristics of the solid additive and the dispersing fluid will also affect the dispersion rate. In a study of TiO_2 dispersion, Lee et al. investigated the effect of porosity on the erosion rate constant (k'' in Equation 2.8). The authors found that the

erosion of low porosity TiO_2 grades followed Equation 2.8. However, higher porosity grades of TiO_2 did not follow this erosion model, and are strongly dependent on the infiltration of the dispersing medium [69].

Bohin et al. investigated infiltration by soaking clusters of silica for 2 to 30 minutes prior to dispersion. The clusters with longer soaking times eroded more quickly and to smaller radii than the shorter soaking times [8]. Kasaliwal et al. investigated infiltration of polycarbonate (PC) into MWCNT clusters during twin-screw extrusion. Results showed that at low mixing speeds, the higher viscosity PC resulted in better dispersion due to the increase in shear stress. However, at higher screw speeds, the low viscosity PC resulted in dispersion equivalent to more viscous grades even with lower equivalent stress. The authors concluded that at high screw speeds the infiltration of the fluid became more significant, allowing for low viscosity PC to achieve dispersion quality comparable to higher viscosity grades with lower torque requirements [3].

Villmow et al. extruded MWCNT in PLA and investigated the effect on MWCNT concentration on dispersion. When the concentration of MWCNT was increased from 7.5 to 15.0 wt%, a greater percentage of the filler was dispersed. This is attributed to the composite melt viscosity increasing with higher MWCNT concentrations, resulting in high shear stresses [72].

2.5.2 Pharmaceutical Properties

One emerging utility of twin-screw compounding is the manufacturing of pharmaceuticals. By compounding an API into a water-soluble polymer, the dissolution and absorption behavior of an ingested drug can be vastly improved [12–14]. However, while twin-screw compounding can improve the bioavailability of a poorly soluble API, the extrusion process can introduce adverse effects, resulting in an unsafe or ineffective drug. As a result of extrusion, high water content in the extrudate can alter the bioavailability of the drug, effecting the safe storage times and temperatures for the drug. Extrusion can also induce degradation of the API, making the drug dangerous to ingest. The factors affecting the bioavailability, water content, and degradation need to be understood and predicted in order to allow for viable extrusion of a pharmaceutical compound. The experimental method used in the RSD experiment can be used to determine the significance of operating conditions on these pharmaceutical properties as well as evaluate relationships between the property responses and $\%BU$. Using established theory, the response of pharmaceutical properties to operating conditions can clarify the significant physical processes inducing the property changes.

2.5.2.1 Bioavailability

Bioavailability of a drug is strongly determined by its permeability and solubility. Due to the difficulty of altering the permeability, improvements in solubility are typically investigated [12]. Sekiguchi and Obi first investigated improving the solubility of an API

by dispersing the API into a solid, water-soluble carrier forming a solid dispersion. The authors were able to improve the solubility of the API by melting then rapidly solidifying a physical mixture of API and carrier, producing a eutectic mixture [73]. While a eutectic mixture is a type of solid dispersion, the API is not dissolved in the carrier. Today, solid or glassy solutions are the more common forms of solid dispersions because they dissolve the API into either a crystalline or amorphous carrier, achieving molecular dispersion [74, 75]. Molecular dispersion is the greatest possible size reduction for the API [12], with the small API particles resulting in much higher dissolution rates [13, 76]. Numerous authors have demonstrated the improvement in solubility achieved with a solid dispersion compared to both the pure API as well as a physical mixture of the API and carrier [77, 78]. With these improvements in solubility, solid dispersions were adapted to twin-screw extrusion due to the benefits of continuous processing, scale-up potential, and relatively short processing times [12].

Twin-screw extrusion compounding has been shown as a viable way to generate solid dispersions with improved solubility compared to both the pure API and the physical mixture of the API and the excipient [11]. For pharmaceutical applications, the extrudate is commonly pelletized into granules, which are later pressed into pills or tablets [75]. In these instances the TSE is responsible for the majority of mechanical and chemical interactions during processing. In order to achieve high drug bioavailability, the extrusion process needs to convert crystalline API to amorphous form by dissolving it in an amorphous polymer carrier. Amorphous solutions and APIs have higher solubility during ingestion due to the lower lattice energy presenting a weaker thermodynamic

barrier to dissolution [74, 79].

Several works have investigated the effects of extrusion operating conditions on the solubility of the final composite drug. Shibata et al. investigated the effect of N, T_b, and residence time on the crystallinity of an API, indomethacin, in crospovidone, a water-soluble carrier. The results for T_b and N are shown in Figure 2.15, with crystallinity measured by x-ray diffraction peaks: higher intensity indicates more crystalline API. As seen in 2.15, increases in T_b decreased the crystallinity, while increases in N increased the crystallinity. The authors also found that increases in retention time decreased the crystallinity [80]. Similar results were observed by Nakamichi et al. on a twin-screw extruder with only conveying elements. As N increased, the crystallinity increased, and as residence time increased, crystallinity decreased [81]. While these studies investigated T_b, N, and time as variables with independent effects, their physical effects will interact. As previously shown in Equation 2.2, N will affect the residence time. In addition, N and T_b will both affect the temperature of composite melt. These interaction effects could explain the contradictory results observed by other authors. Liu et al. found that in addition to increasing T_b, increasing N decreased the crystallinity of an API [82]. Lyons et al. found that neither T_b or N had an effect on the crystallinity [83].

The screw geometry within an extruder can also be designed to maximize dissolution of an API into an excipient. Studies have shown that introducing KBs into a screw geometry reduces crystallinity and improves dissolution behavior of the API [81, 84]. This can be attributed to the previously described effects of KBs on distributive and dispersive and mixing in a TSE. By increasing the distributive mixing in a pharmaceutical

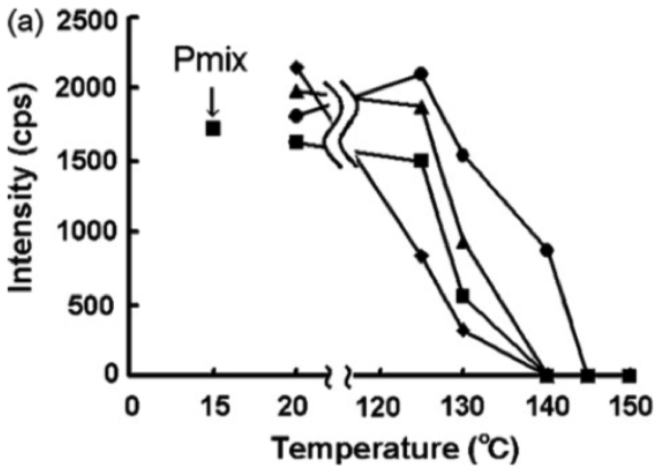

FIGURE 2.15: The effect of N and T_b on crystallinity, as measured by the intensity of x-ray diffraction peaks [80]: N = (•) 200 min^{-1}; (▲) 50 min^{-1}; (■) 30 min^{-1}; (♦) 15 min^{-1}

composite melt, the API is further homogenized into the melt, improving its dissolution rate into the polymer carrier. Similarly, by improving the dispersive mixing, agglomerated API is dispersed [85], reducing the average size of the API clusters and therefore improving dissolution of API into a polymer [84].

2.5.2.2 Water Content

In order to create an amorphous solution, the API and excipient need to be mixed at a high-energy state then stabilized to prevent recrystallization. This can be achieved by storing the composite below its glass transition temperature, which physically obstructs API recrystallization. However, the API has been shown to recrystallize even below the glass transition temperature [86, 87]. This recrystallization can be induced by water content in the extrudate. The presence of water acts a plasticizer, reducing

the glass transition temperature of the composite and therefore encouraging recrystallization of the API. This effect was demonstrated by Hancock et al. with the excipient poly(vinylpyrrolidone) (PVP) and is shown in Figure 2.16. As the weight fraction of water in the PVP increased, the glass transition temperature decreased [88]. High water content has also been shown to decrease the glass transition temperature of the API [87]. Physically, high water content has been shown to increase the crystallization of the API after a four week drug storage time [11] and decrease the storage time before recrystallization [78].

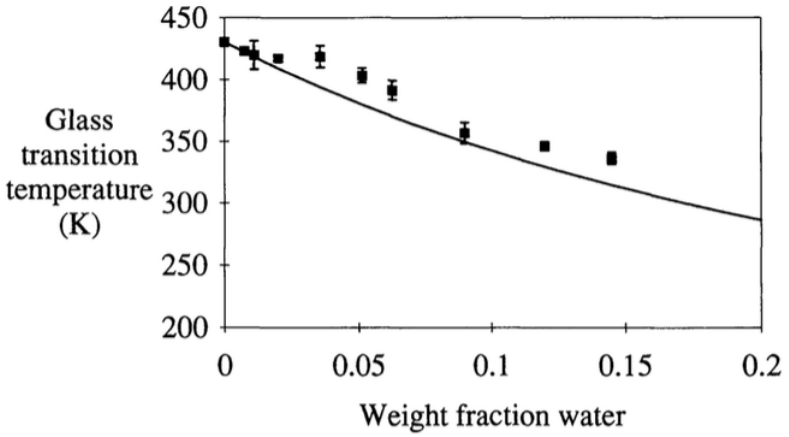

FIGURE 2.16: The effect of water content in PVP on the glass transition temperature [88].

To reduce the water content in the composite melt, residual water is evaporated and vented away during extrusion in a process termed devolatilization. Devolatilization is driven by the concentration gradient between the surface and pool of the melt. As water is evaporated away from the surface, water content in the pool diffuses towards the surface, continuing the evaporation process. This behavior occurs within the melt in the screw channels [89] and in the thinner layers of melt deposited along the barrel

walls with every revolution [50]. The devolatilization process is a function of several variables, including the screw geometry and vent design, as well as the operating conditions of N, Q/N, and T_b. As N is increased, the melt on the surface regenerates more quickly, allowing for more efficient removal of water. Increasing N also decreases Q/N, increasing the surface-to-volume ratio in the channel which provides more avenues for vapor evaporation per unit volume [90]. Increasing T_b will add heat that encourages evaporation as well as decreasing the viscosity of the melt, allowing for more efficient vapor diffusion.

2.5.2.3 Degradation

While twin-screw extrusion can lead to strong improvements in the bioavailability of a drug, the process is often limited by the degradation behavior of the API. Degradation of an API is a chemical reaction that converts the API into unsafe or ineffective forms. The occurrence of degradation during processing may necessitate additional safety testing of the final drug or potentially inhibit the ability of extrusion to produce a viable final product. The degradation behavior can be difficult to universally predict and prevent due to the unique APIs for every pharmaceutical extrusion process. API degradation is commonly attributed to processing for long residence times at high melt temperatures that drive the degradation reaction [11, 12, 76, 85]. The mean residence time has been previously presented as a function of N and Q (Equation 2.2), with increases in either operating condition resulting in decreased t_{mean}. The temperature of the melt is strongly affected by the operating T_b for an extrusion process as well as the viscous heating that

occurs due to the shearing of the melt. The viscous heating is a function of several variables, but is commonly controlled by the operating N.

Feng et al. investigated the degradation behavior of bifendate, an API, compounded with polymer carriers in a co-rotating TSE. The results for the effect of T_b on degradation of 10 wt% bifendate in PVP are plotted in Figure 2.17. The degradation was measured as a weight-percentage of the degradant in the final drug (initial degradant concentration was .08 wt%). Up to 160°C, as the T_b increased, the degradation displayed minor increases. At 180°C, there was a stark increase in the presence of the degradant. This indicates a threshold behavior, where degradation is not significantly initiated until an activating temperature is reached. Using a different water-soluble carrier, Feng et al. also found that higher N during extrusion resulted in lower degradation, attributed to the decreased residence times [91].

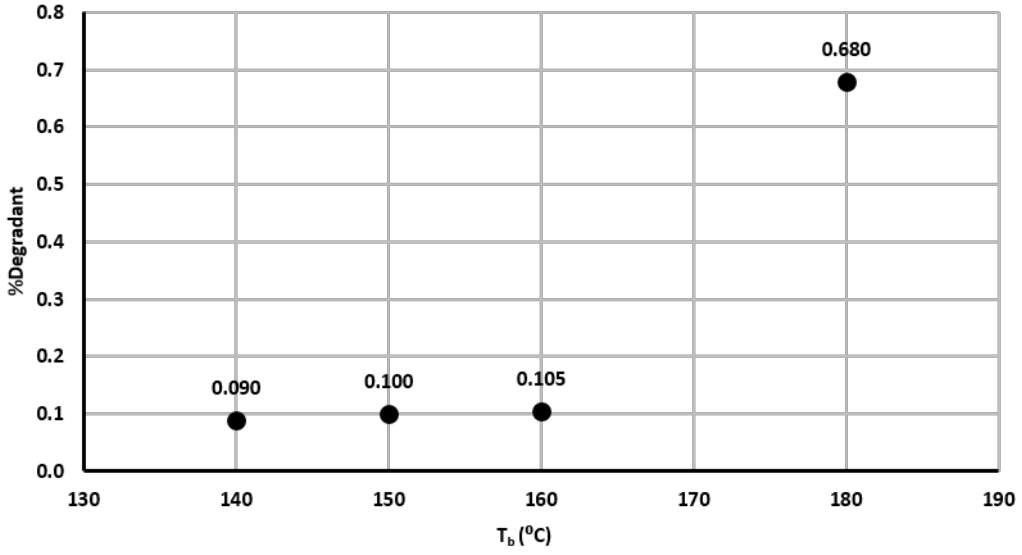

FIGURE 2.17: The effect of T_b on the degradation of an API in PVP. [91].

Results by Feng et al. indicated an adverse effect of increasing N on degradation, suggesting that residence time makes a stronger contribution to degradation than viscous heating. However, viscous heating has been experimentally demonstrated to increase the degradation of an API. Lakshman et al. found that including up to 10 wt% of a plasticizer in an extruded API/PVP compound significantly reduced the degradation. The presence of a plasticizer decreased the viscosity of the melt, reducing the degree of heating by viscous dissipation [92].

Chapter 3

Residence Stress Distribution Experiment

The Residence Stress Distribution (RSD) experiment will be introduced in the following section. The RSD was used in both experiments presented in this thesis in order to quantify the stress developed during a twin-screw compounding process. In addition, the statistical methods used in the RSD experiment were used to determine the effect of operating conditions on other properties. While each experiment used different materials and extruders, the operating principles for the RSD remain the same.

3.1 Materials

The key premise behind the RSD is the usage of polymeric stress beads of known failure strength to measure the stress developed in an extruder flow. The stress sensitive beads used for all RSD testing were Calibrated Microencapsulated Sensor Beads (CAMES beads) provided by MACH I Inc. The CAMES beads are polymeric micro-beads filled with Automate 8A blue dye that stains the polymer melt when the beads rupture. The failure strength of the CAMES beads is dependent upon two parameters: the wall thickness and the bead diameter. The beads are stronger with larger wall thickness and smaller diameters. For the TiO_2 dispersion study, the CAMES beads had a critical strength of 221 kPa, while for the pharmaceutical property experiment, beads with a failure strength of 194 kPa were selected. Bead strengths were selected for each experiment in order to achieve a range of responses across the typical operating range. If the bead critical stresses were too low or too high, no response variation would be observed. A microscopic image of CAMES beads is shown in Figure 3.1.

In order to measure the percent break-up of the CAMES beads, a representative value of 100% break-up is required. This value was generated with an RTD captured using a volume of dye equivalent to 100% break-up of the CAMES beads. The tracer particles used to capture the RTD were produced by dissolving 6.57 grams of high-impact polystyrene (HIPS) in 55 mL of xylene and blending the mixture with .73 mL of Automate 8A blue dye. Once blended, the mixture was left until residual xylene evaporated

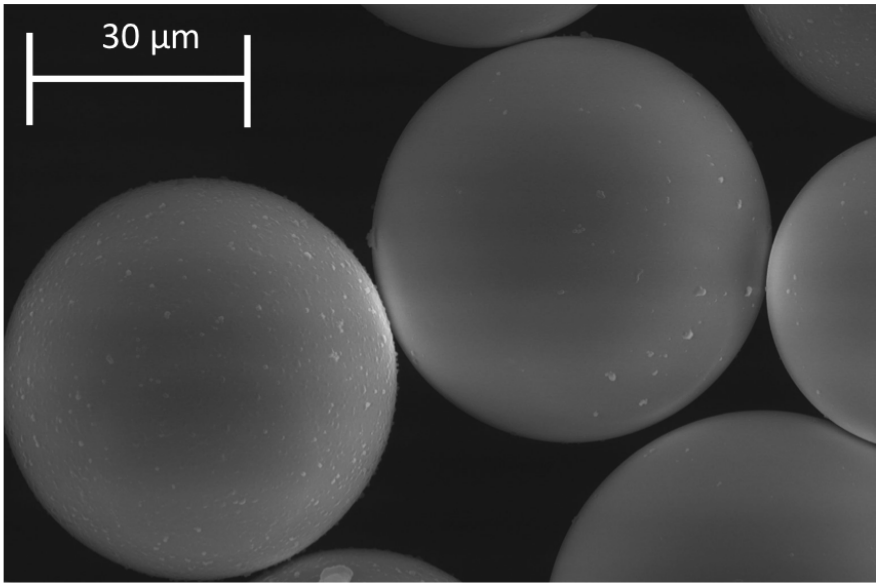

FIGURE 3.1: Microscopic image of CAMES beads. As the bead diameter decreases, the critical stress increases. (*Courtesty of Brendon Ricart, Merck & Co., Inc.*)

away, leaving a solid blue disk. This disk was then cut into small pieces termed ink shots that could easily be injected into a screw channel.

RTDs and RSDs were measured two and three times respectively in order to ensure accuracy of the results. If there was an error during the recording of a distribution, the measurement was repeated. The weight of ink shots and CAMES beads inserted for RTD and RSD measurement was a function of the extruder size. On large extruders, a greater volume of tracer was required in order to observe the signal in the flow. On small extruders, the volume was minimized in order to fit all tracer particles into approximately a single screw channel. While the volume of ink shot and CAMES beads changed depending on extruder size, the ratio between ink shot and CAMES shot was maintained. This ensured that the volume of Automate blue 8A contained in the ink shot

represented 100% CAMES bead break-up. On the 30 mm extruder used for TiO_2 dispersion study, the ink shot and CAMES beads injections were .63 and .51 grams respectively. For the pharmaceutical extrusion study, the 18 mm extruder required .315 grams of ink shots and .255 grams of CAMES beads.

3.2 Equipment

Completion of the RSD experiment requires the installation of light-sensing equipment that captures the dye staining from the ink shots and CAMES beads. For both experiments, the same sensing equipment was used and the installation procedure was the same.

In order to measure the light reflectance of the melt, a steel shell with a transparent viewing window is inserted into the extruder. The shell (Figure 3.2) is a hollow stainless steel cylinder with 1/2-20 UNF threading allowing it to be screwed into a port. The transparent window is made up of sapphire and is fitted into the end of the shell. The tip of the shell fills a section of the barrel wall, allowing it to observe the melt dragged against it.

FIGURE 3.2: Steel shell inserted into an extruder for RSD experiments. The narrow end has a sapphire window that transmits light to the melt and back.

Inserted into the steel shell is a bifurcated light probe that both transmits light to the melt and collects the reflected light. One leg of the light probe is inserted into an adjustable halogen light source while the other leg transmits the reflected light to a light sensor. The light sensor is a photodiode that transforms the intensity into a voltage response, which is then channeled to an amplifier, then a connector block that interfaces with a computer. For RTD measures, a battery-powered button is attached to the connector block as well. This button is used as a binary impulse to indicate when the ink shots have been injected.

In order to ensure consistent injection of the ink shots and CAMES beads, a shot dropper tool was developed. The shot dropper uses a swinging door design to deposit the tracer as quickly as possible; ideally the entirety of one drop would be injected into a single screw channel. The shot dropper was also designed tall enough to reach the edge of the screw channels from the top of an open port, limiting scatter of the tracer during injection. The shot dropper tool is shown in Figure 3.3 with both the open and closed door position.

3.3 Experiment

Once the RSD components are installed, the operating conditions for N and mass feed rate ($\dot{m}$) are set and extrusion can begin. Before RTD and RSD measurement, the process is allowed to reach steady state to ensure accurate measurement of the desired operating conditions. Once steady state is reached, the ink shots or CAMES beads are

(a) Closed Door (b) Open Door

FIGURE 3.3: The shot dropper used to injected ink and CAMES into an extruder.

loaded into the shot dropper and dropped through the injection port. When the tracers are dropped, the button is pressed to indicate the time of injection.

As the ink or CAMES travel through the flow, the dye stains the polymer melt and reduces the intensity of reflected light as measured by the light probe. This change in light intensity is measured by the probe system, sampled at a rate of 1200 Hz. The voltage response is read in LabVIEW in order to display a real-time output. Initial filtering is completed in LabVIEW, with further filtering and processing completed in MATLAB. The final output from MATLAB is a continuous, normalized distribution. A sample RTD and RSD output are shown together in Figure 3.4.

A metric for stress history was generated using the ratio of the areas of the RSD and RTD curves (Equation 3.1). Since the RTD represents 100% break-up of the beads, the ratio of area under the RSD and RTD curves equals the percentage of beads that broke

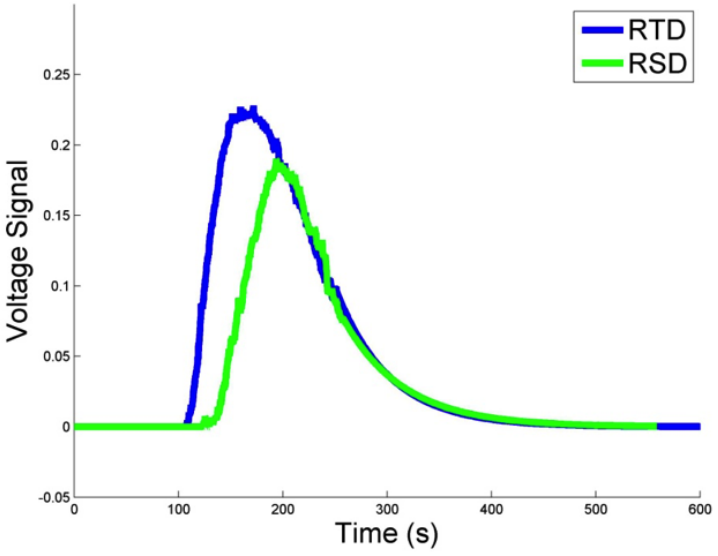

FIGURE 3.4: An RTD and RSD curve output after MATLAB processing.

during the processing, or the percent break-up ($\%BU$).

$$\%BU = \frac{Area_{RSD}}{Area_{RTD}} \cdot 100\% \tag{3.1}$$

The $\%BU$ represents the percentage of the melt that experiences the critical strength of the CAMES beads during processing. For example, 40 $\%BU$ of beads with a 100 kPa critical strength indicates that 40% of the melt will experience a stress of at least 100 kPa or greater.

3.4 Statistical Methods

3.4.1 Design of Experiments

Understanding of the stress developed across an operating domain allows for refined process control. Through a Design of Experiments approach, the $\%BU$ response was investigated as a function of the operating conditions N and Q/N. A central composite design (CCD) grid was used as the experimental design in RSD experiments. The CCD grid consists of nine sets of operating conditions for two variables, spanning five factors levels. The design of the CCD grid allows for the determination of the significance of two variables, their interaction, and second order effects. For these experiments, CCD grids were used to evaluate the significance of N and Q/N on the $\%BU$. For statistical analysis and comparison, the operating conditions need to be expressed as their normalized coordinate location in the DoE realm. This allows for direct comparison of the N and Q/N effects across the operating domain. The typical CCD design is shown in Figure 3.5 with the coordinate value indicated at every set of operating conditions.

3.4.2 Predictive Equations

Once experiments for all nine conditions on a CCD grid are completed, the significance of the operating conditions is analyzed using a standard least-squares regression in JMP Pro 11.0.0. The significance of N, Q/N, and higher order terms and interactions is evaluated with a significance level of α = .05 and quantified with coefficient values.

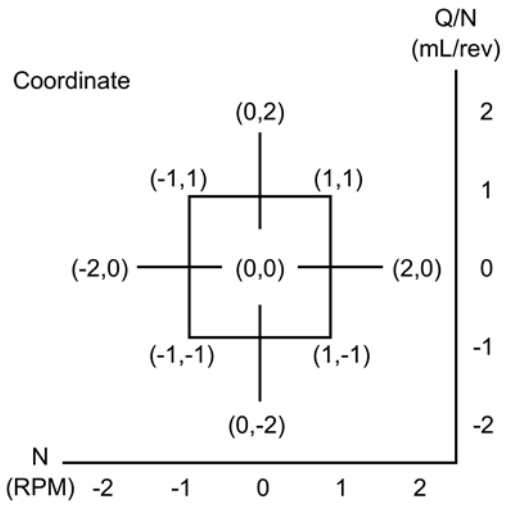

FIGURE 3.5: The coordinate values on a CCD grid.

These coefficients were combined with an intercept term to construct predictive equations for $\%BU$ as a function of the statistically significant variables. The significant variables were selected using a top-down approach. Initially regression analysis considered N and Q/N as well as second order terms and interactions. Insignificant higher order terms were removed in succession until only significant terms remained. The 2-D equations will be presented with these significant terms as well as the associated R^2 term, indicating the degree of fit of the predictive equations.

If no second order terms or interactions are significant, the predictive equation takes the form of Equation 3.2, where I is the intercept value and X represents the coefficients for N and Q/N. If additional variables are determined to be significant, Equation 3.2 would require additional coefficients.

$$\%BU = I + (X_N \cdot N) + (X_{Q/N} \cdot Q/N) \tag{3.2}$$

Equation 3.2 represents the response surface for $\%BU$ over the N and Q/N operating domain. The intercept term (I) in Equation 3.2 indicates the predicted $\%BU$ value at the (0,0) coordinate in Figure 3.5. If the $\%BU$ is a function of only linear coefficients, I will represent an average $\%BU$ over the tested operating domain. The X_N and $X_{Q/N}$ coefficients indicate the sensitivity of $\%BU$ to N and Q/N respectively. Large coefficients indicate a greater control over $\%BU$ with the corresponding operating condition.

Chapter 4

Titanium Dioxide Dispersion Study

Titanium dioxide (TiO_2) is one of the most commonly used pigments due to its high refractive index and its ease of use [93]. Agglomerated TiO_2 is commonly compounded into a polymer matrix using a TSE, resulting in a composite final product. In order to achieve exceptional mechanical and optical properties, agglomerated TiO_2 needs to be dispersed during processing [5, 10].

For this experiment, preliminary testing is completed to identify the dispersion behavior of TiO_2 and its relationship to the applied hydrodynamic stress. Using this relationship, the dispersion behavior of TiO_2 clusters is related to the stress level within a TSE. The RSD experiment is used to determine the amount of material that experiences a certain stress level within a twin-screw compounding process as well as investigate the effect of process variables on stress. Within a twin-screw extrusion process, the stress can be predicted by the operating conditions N and Q/N [57–60] as well as the

design of the screw geometry [61]. In this experiment, these three factors are evaluated in a standard LDPE/TiO_2 compounding process. Three screw designs are evaluated with different mixing sections across the same set of N and Q/N operating conditions. Results show how the screw designs affect the stresses developed in a melt and how sensitive each geometry is to changes in N and Q/N. Considering dispersion theory and the preliminary experiments, stress history results are used to relate the operating conditions and screw geometry to the dispersive mixing capability of a process.

4.1 Titanium Dioxide Dispersion Behavior

In preliminary experiments, TiO_2 dispersion is directly investigated by applying a constant stress and observing the dispersion behavior. By observing the size of the dispersed aggregates and agglomerates, the occurrence of erosion and/or rupture is predicted. In addition, the relationship between hydrodynamic stress and TiO_2 cluster diameter is determined. By establishing the behavior of TiO_2 dispersion at constant stress, dispersive mixing during twin-screw compounding can be related to the stress developed within a TSE.

4.1.1 Experiment and Operating Conditions

The dispersion behavior of TiO_2 was investigated using a Texas Instruments ARES G2 cone and plate rheometer run at different set shear stresses. The cone and plate geometry

had a diameter of 40 mm and a cone angle of 4°. Due to the angle of the cone, the cone and plate rheometer allowed for nearly constant shear rates along the radial direction, ensuring that the majority of the sample experienced the desired shear stress.

For the experiment, samples of undispersed TiO_2 were combined with a transparent polymer and a blue dye prior to shearing. The TiO_2 used in this experiment was grade R-104, supplied by Chemours Inc. This TiO_2 is hydrophobic and has a density of 4.2 g/cc. The primary particle size for this grade of TiO_2 is approximately .2 μm, representing the minimum dispersion size. The primary particles of this size can be seen on the SEM image of a TiO_2 cluster in Figure 4.1.

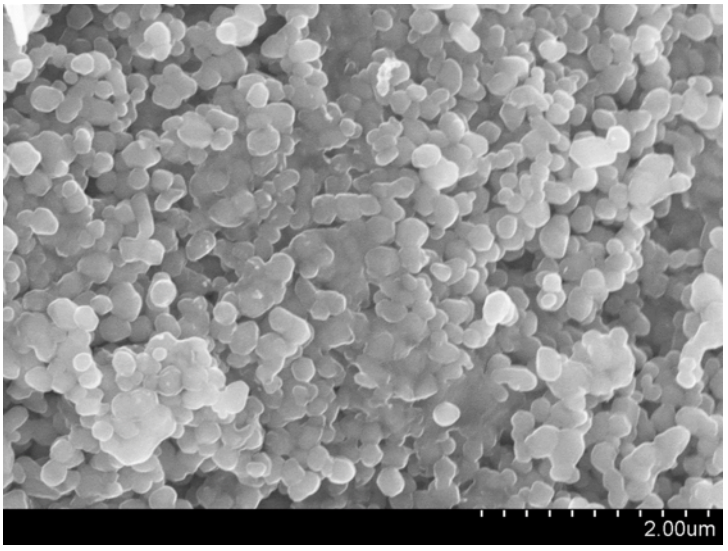

FIGURE 4.1: Primary particles for TiO_2 R-104 are approximately .2 μm in size.

The polymer used to disperse the TiO_2 was polybutene Indopol H-300, supplied by INEOS. This polybutene is relatively Newtonian, with an approximate viscosity of 70 Pa-s. The Newtonian behavior of the polybutene is confirmed by the linear relationship between shear rate and shear stress observed in Figure 4.2. A Newtonian polymer was

selected to ensure equivalent melt infiltration at different shear stresses. The density of this material was 0.904 g/cc.

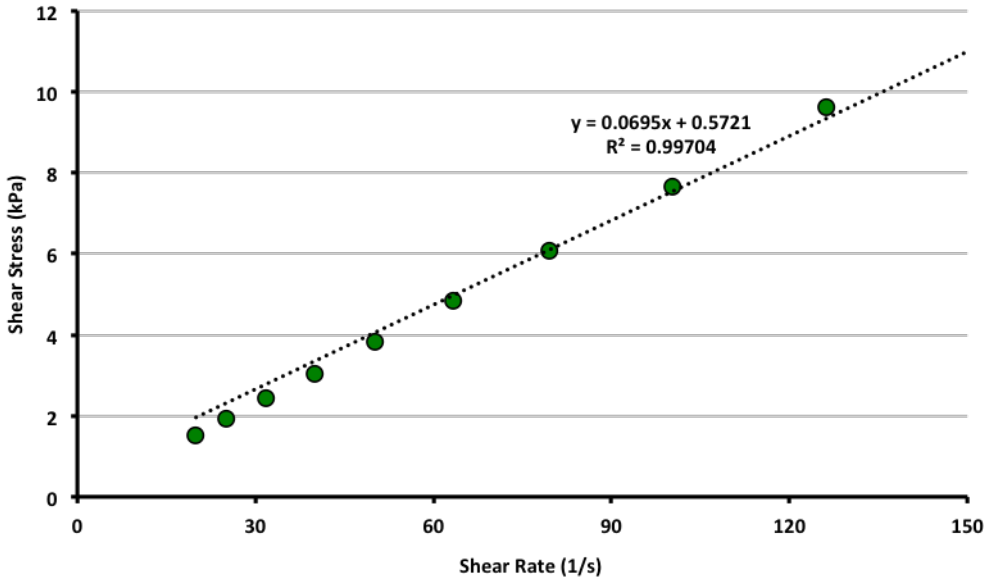

FIGURE 4.2: The shear rate and shear stress relationship of the polybutene used during TiO_2 dispersion testing. The linear relationship is classified as Newtonian behavior.

The mixture of TiO_2 and polybutene was prepared with 0.1 g of TiO_2 and 25 g of polybutene. In addition to these two materials, 0.1 mL of Automate Blue 8A dye (provided by Keystone Inc.) was added to the mixture to reduce optical interference effects. The blue dye dampened optical noise from well-dispersed TiO_2 during imaging, an effect shown by the sparkling effect in Figure 4.3.

Once prepared, the mixture was placed on a sheet of thin, transparent Mylar that was attached to the bottom plate of the rheometer to allow for easy removal of the sample after testing. Samples were run for 4 min, each at a different constant shear stress. This time was selected to ensure rapid rupturing until a critical diameter is reached, while erosion will continue to slowly disperse. Approximately 30 seconds of ramp-up time

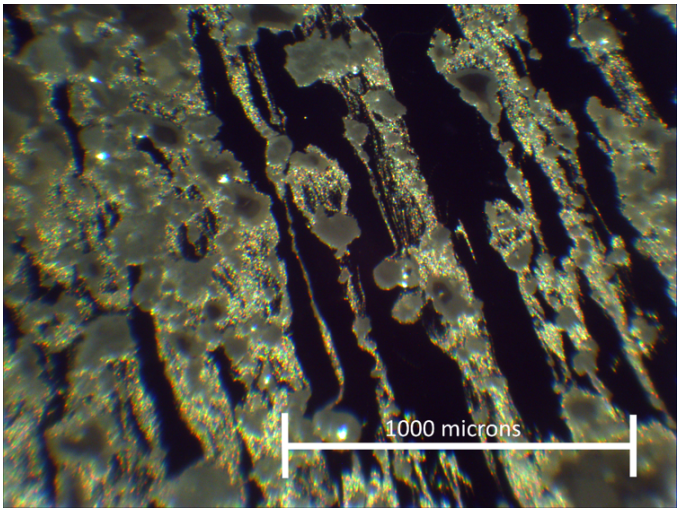

FIGURE 4.3: The optical interference caused by small diameter TiO_2.

was required for the samples to reach their desired stress level without splattering. The following shear stresses were investigated: 100 Pa, 1,000 Pa, 5,000 Pa, and 10,000 Pa. The 100 Pa value was chosen as a control condition to reflect the dispersion induced through preparing, testing, and analyzing the sample since 100 Pa is too low to induce significant dispersion. The 10,000 Pa was chosen as the upper-limit for the stress testing due to torque and speed limitations of the rheometer. These stresses are much lower than the stresses developed in a TSE mixing section, but still allow for development of dispersion behavior. Previous authors who investigated TiO_2 dispersion have achieved results well below 10,000 Pa [5, 69].

Once samples were run on the rheometer, they were removed and optically analyzed. Optical imaging was completed using a UNITRON Versamet-2 optical microscope with images captured using an OptixCam camera. Micrographs were recorded in 30 locations across the sample and analyzed in MATLAB with an in-house code (see Appendix

A). The code removed gradient background noise, filtered local color variations, converted the image to black-and-white, and isolated all of the clusters. The image analysis process is shown in Figure 4.4.

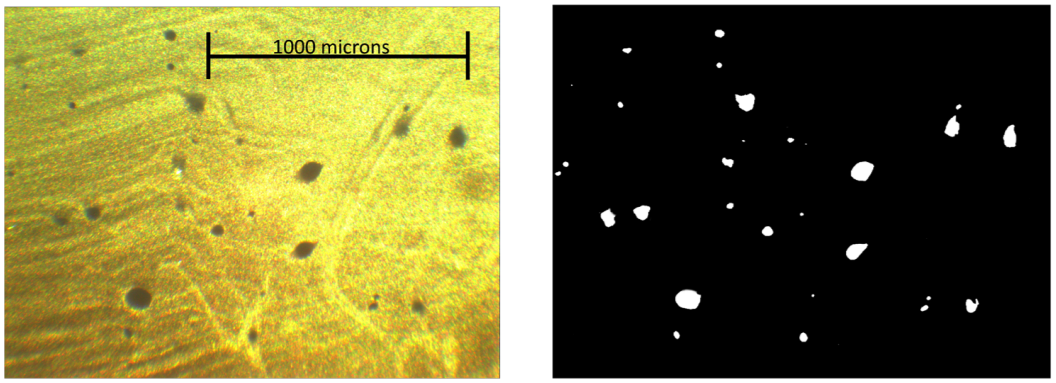

(a) Raw Image (b) Processed Image

FIGURE 4.4: The image analysis process for TiO_2 run at a constant stress on a cone and plate rheometer.

Using the cluster sizes in the analyzed images, diameters and volumes were estimated using a spherical approximation. Results from all analyzed pictures were summed and used to generate a final diameter and volume distribution. This process was repeated for each stress level investigated.

4.1.2 Results

4.1.2.1 Diameter Distribution

The range of cluster diameters identified post-shearing was binned in 10 μm increments to allow for creation of histograms. Figure 4.5 shows the number of clusters identified in each bin. The x-axis in Figure 4.5 has been abridged to 0 to 250 to allow for an

adequate viewing window of the results, but there were four agglomerates beyond that threshold (260, 360, and 440 μm at 100 Pa and 330 μm at 1000 Pa).

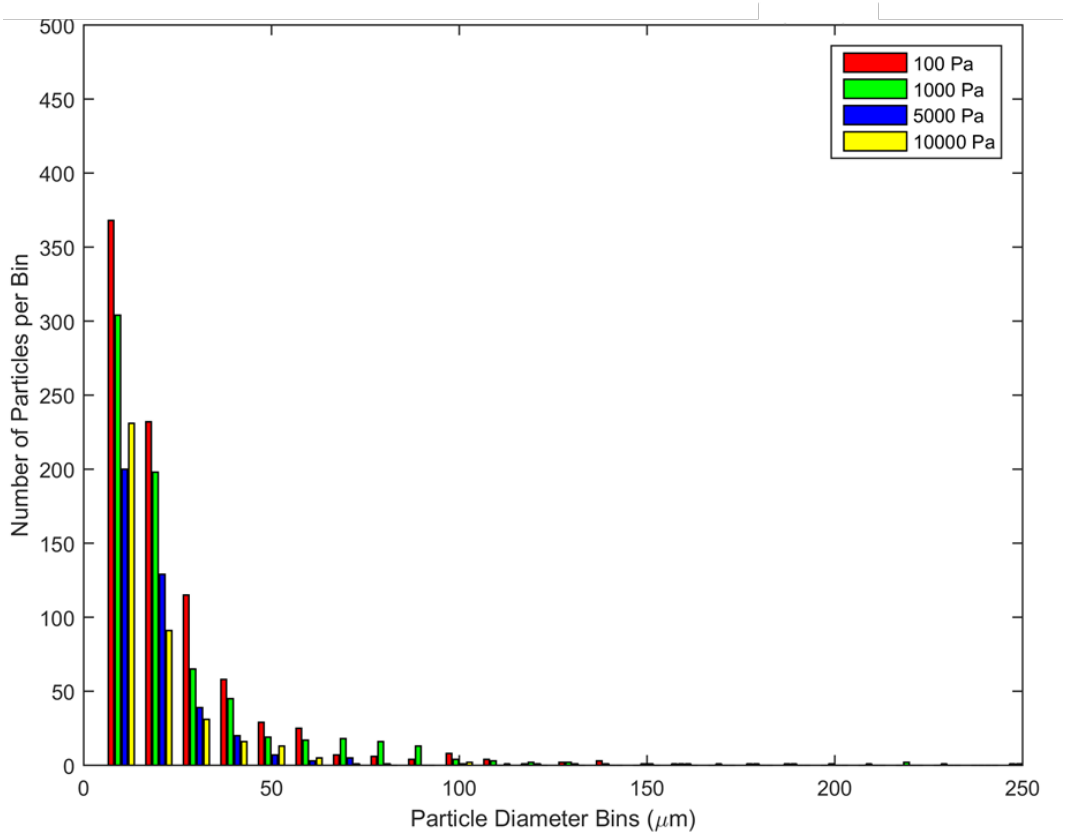

FIGURE 4.5: Diameter distribution of TiO_2 clusters after 4 min on rheometer at different shear stresses.

The results in Figure 4.5 show that regardless of shear stress, the shape of the cluster diameter distribution are similar. With every shear stress tested, the most populated diameter bin was <10 μm with the majority of clusters under 100 μm in diameter. At every shear stress level, the distribution is continuous up to the 60 μm bin. Increasing the shear stress decreased the total number of aggregates and agglomerates, behavior observed in nearly every bin. Additional statistics about the diameter distribution are shown in Table 4.1.

TABLE 4.1: TiO_2 diameter distribution statistics.

Stress Level (Pa)	Total number of clusters	Maximum cluster size (μm)	Clusters greater than 20 μm
100	869	440	269 (31%)
1000	719	330	217 (30%)
5000	409	150	80 (20%)
10000	391	100	69 (18%)

The second column in Table 4.1 shows the total number of clusters found at each stress level. As the stress level increased, less clusters were observed. Although higher stresses should break large clusters into more, smaller clusters, continuous erosion is producing smaller particles than the the observable resolution of the micrograph (approximately 1 pixel or 1.35 μm). The camera cannot capture aggregates or primary particles below 1.35 um. Completely dispersed TiO_2 would result in zero observable clusters.

Another value presented in Table 4.1 is the maximum cluster size found at each stress level. Again, this is found to decrease with increasing shear stress. This is a relationship observed by several authors for both rupture [63] and erosion [68, 69] where the critical strength of an agglomerate or aggregate is a function of its diameter. If the applied stress is high enough, clusters should rupture until they achieve a diameter too small for the rupture mechanism, then they will solely erode. Erosion will continue again until a critical diameter is reached at which dispersion will stop. The largest particles at each shear stress are an indication of the largest particles sizes that will not abruptly rupture.

The final column in Table 4.1 shows the total number of clusters that were greater than the 20 μm bin. Through discussions with operators, this bin was selected as the desired TiO_2 diameter in order to produce acceptable dispersion quality in a composite product. Clusters below 20 μm are generally considered well-dispersed, while clusters greater than 20 μm are not sufficiently dispersed. Included with the number of well-dispersed clusters is the percentage of well-dispersed clusters as a ratio of the total identified clusters. Increasing the shear stress from 100 to 1,000 Pa reduced the total number of clusters and the maximum cluster size, but it did not significantly reduce the number of clusters greater than 20 μm. However, increasing from 1,000 to 5,000 Pa resulted in a noticeable decrease in the number and percentage of clusters greater than 20 μm. This indicates a clear change in dispersion behavior between 1,000 and 5,000 Pa.

4.1.2.2 Volume Distribution

Dispersion quality is strongly influenced by the volume of the undispersed clusters in addition to the number. A single undispersed large agglomerate can produce thousands of aggregates and primary particles. In order to determine the size of the clusters in this study, spherical volumes were assumed from the 2-D images. Volumes were calculated by considering the equivalent volume of the imaged clusters, and binned by diameter. While a volumetric representation portrays the same information as Figure 4.5, it presents new ways to view and interpret the data. The new distribution is shown in Figure 4.6 with a logarithmic y-axis.

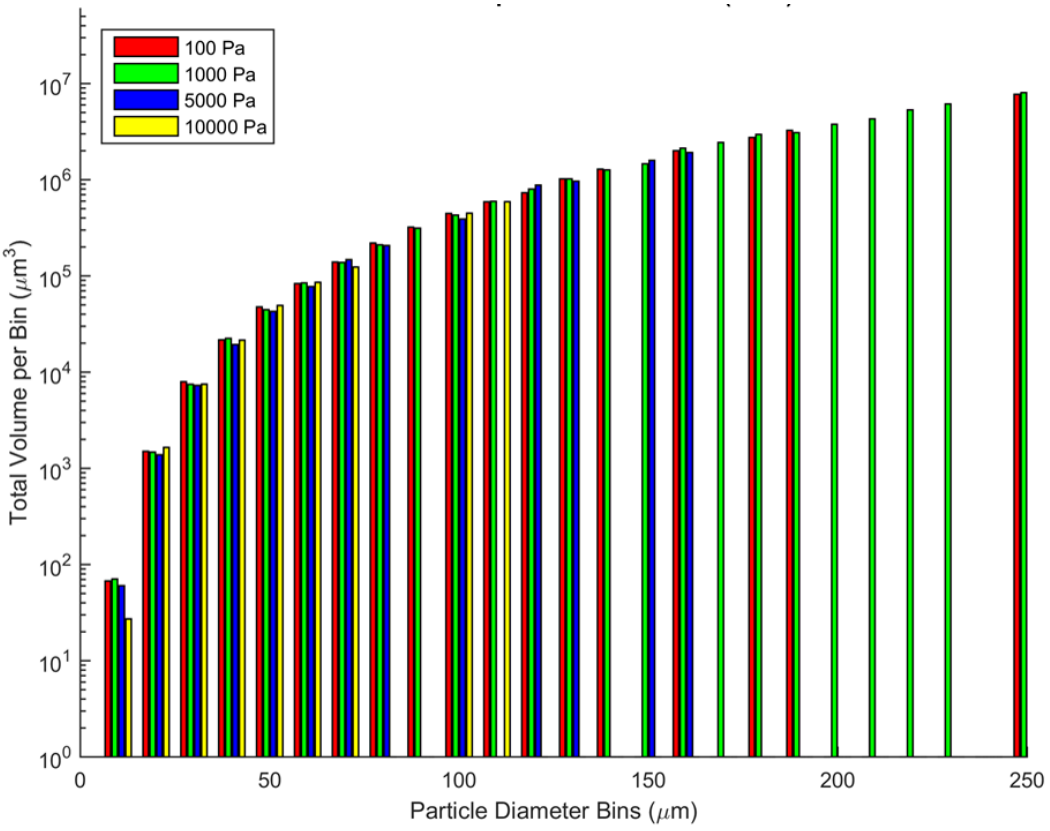

FIGURE 4.6: Distribution of TiO_2 clusters after 4 min on rheometer at different shear stresses, weighted by volume per bin.

Figure 4.6 shows the same information as Figure 4.5, but also illustrates the significance of the large cluster volume. At low diameters, the volume distribution is relatively similar across all shear stresses. At higher diameters though, the higher shear stress conditions are not continuous with populated and unpopulated bins interspersed. This discontinuous distribution is characteristic of rapid rupturing of a cluster into two or more aggregates. The volume of the large agglomerates present at 100 and 1,000 Pa is divided between several, smaller aggregates at higher stresses; this is not indicative of a single agglomerate slowly eroding. Additional information about this distribution is provided in Table 4.2.

TABLE 4.2: TiO_2 volume distribution statistics.

Stress Level (Pa)	Volume % of Largest Cluster	Equivalent 20 μm undispersed
100	45.5%	23,000
1000	28.8%	15,000
5000	30.7%	1,500
10000	44.4%	320

The second column in Table 4.2 shows what percentage of the volume is represented by the largest cluster, as seen in Table 4.1. There does not appear to be a relationship between the volume of the largest cluster and the applied stress. At both 100 and 10,000 Pa, the volume percentage of the largest cluster was almost 50% of the total measured volume. The third column is titled "equivalent 20 μm undispersed." This value is calculated by taking the total volume in the diameter bins greater than 20 μm and determining how many 20 μm clusters could recreate that equivalent volume. For example, at 100 Pa, 23,000 of the 20 μm diameter clusters are essentially encased in the undispersed volume. As the shear stress in increased in Table 4.2, the number of equivalent undispersed 20 μm clusters decreases, reaching a low value of 320 at 10,000 Pa. The equivalent 20 um dispersed totals are a representative metric of dispersion progress. The results were plotted versus shear stress and fit with an exponential decay function, show in Figure 4.7. The exponential decay shows good agreement (R^2 = .9778) with the experimental data. This type of fit indicates that rapid reduction in undispersed volume can be achieved at low shear stresses, however, significantly higher shear stresses need to be

reached in order to achieve entirely well-dispersed clusters. Using the fitting equation in Figure 4.7, in order to disperse down to a single undispersed cluster, 25 kPa of stress is required.

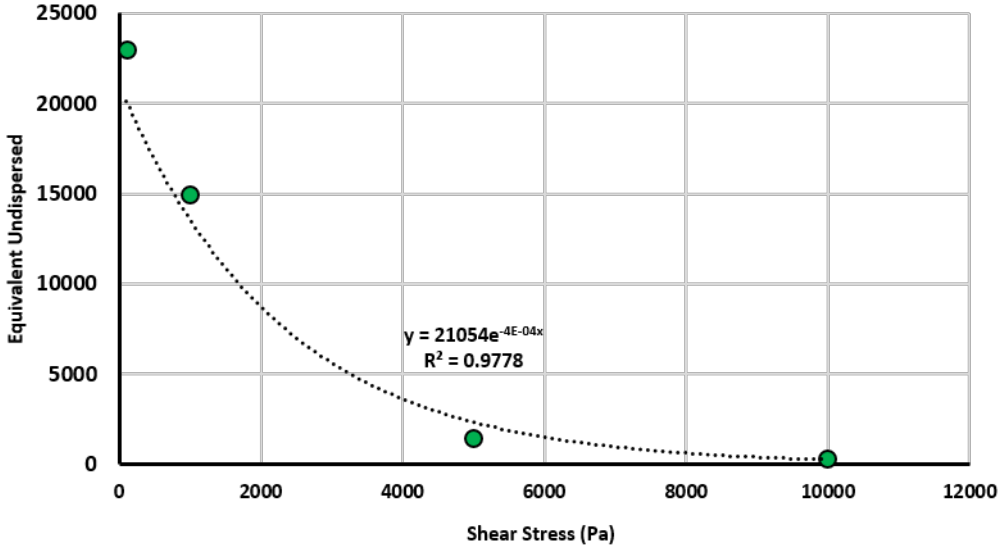

FIGURE 4.7: Equivalent number of undispersed 20 μm clusters versus shear stress.

4.1.3 Discussion

Results from the TiO_2 dispersion experiments showed the effect of shears stress on dispersion behavior. For all shear stresses tested, the shapes of the diameter distributions were similar. However with increasing stresses, the total number of clusters, the maximum cluster size, and the number of clusters greater than 20 μm decreased. This result can be attributed to higher shear stresses increasing the hydrodynamic stress in the Fa number, inducing rupture even with increases in cohesive strength. Differences in dispersion behavior were observed to occur between 100 and 10,000 Pa. At stresses 1,000

Pa and lower, the TiO_2 clusters primarily eroded, indicated by the continuous distributions in Figure 4.5 and 4.6. Between 1,000 and 5,000 Pa, the dispersion behavior transitions to a combination of erosion and rupture and the distribution became discontinuous at large diameters. At the 5,000 and 10,000 Pa conditions, rupture occurred at cluster diameters above approximately 60 – 70 μm, with erosion occurring at smaller diameters. In order to reduce cluster diameters below 20 μm, the rupture threshold diameter needs to be decreased by applying higher stresses.

The 5,000 and 10,000 Pa conditions also resulted in significantly less volume at diameters greater than 20 μm. This behavior was seen in Table 4.2 and plotted in Figure 4.7. The exponential decay behavior in Figure 4.7 highlights a common issue with dispersing TiO_2 in a polymer. While increased stresses can disperse the majority clusters below 20 μm (or any other benchmark diameter), significantly higher stresses are required to ensure no clusters are undispersed. The presence of a single undispersed cluster can introduce mechanical failure and ruin optical quality.

In the twin-screw extrusion of a TiO_2 composite, stress levels of several hundred kPa are usually achieved within the composite melt. However, the largest stresses in the TSE occur in the mixing sections, and TiO_2 clusters remain in these regions for times much less than 4 min. In order to reduce the probability of poorly dispersed TiO_2 in an extruded composite product, the process should be controlled and designed to maximize stress in the mixing sections. As seen in these dispersion experiments, increasing the stress will improve the dispersion of the TiO_2 by increasing the probability of rapid rupture.

4.2 Mixing Section Stress

The results in Section 4.1 show that the shear stress applied to a TiO_2 cluster has a significant effect on the dispersion quality. Increasing the shear stress within a melt increases the Fa number, improving the probability of dispersion and increasing the likelihood of the rupture dispersion mechanism. Due to the relatively short processing times in a TSE, rapid rupture is preferred to more gradual erosion. However as TiO_2 clusters disperse, their cohesive strengths will increase, resulting in a critical diameter as a function of the applied hydrodynamic stress [63, 68].

In order to induce rupture of the TiO_2 clusters, hydrodynamic stress should be maximized during processing. The applied shear stress stress can be increased by changes in the operating conditions and screw geometry. In the following sections, these changes will be quantified across a range of N and Q/N operating conditions and three screw geometries in order to determine the conditions that maximize dispersion and allow for the most control over the applied stress.

4.2.1 Materials

The LDPE used in this study was Petrothene NA206000 provided by Equistar Chemicals in Houston, TX. LDPE is transparent, so TiO_2 was added at a 5 wt% to give the melt a baseline white color for optical measurements. The TiO_2 was grade R-104, provided by Chemours Inc. Viscosity measurements for neat LDPE were recorded on a parallel

plate rheometer and compared to data provided by Chemours Inc. for the viscosity of LDPE and 10 wt% TiO_2, show in Figure 4.8. Both response were measured with a melt temperature of 125°C. The shear-thinning behavior of both melts was fit with a power law curve in agreement with shear-thinning theory. The rheological response for the 95/5 wt% concentration used in this study will lie between this two curves.

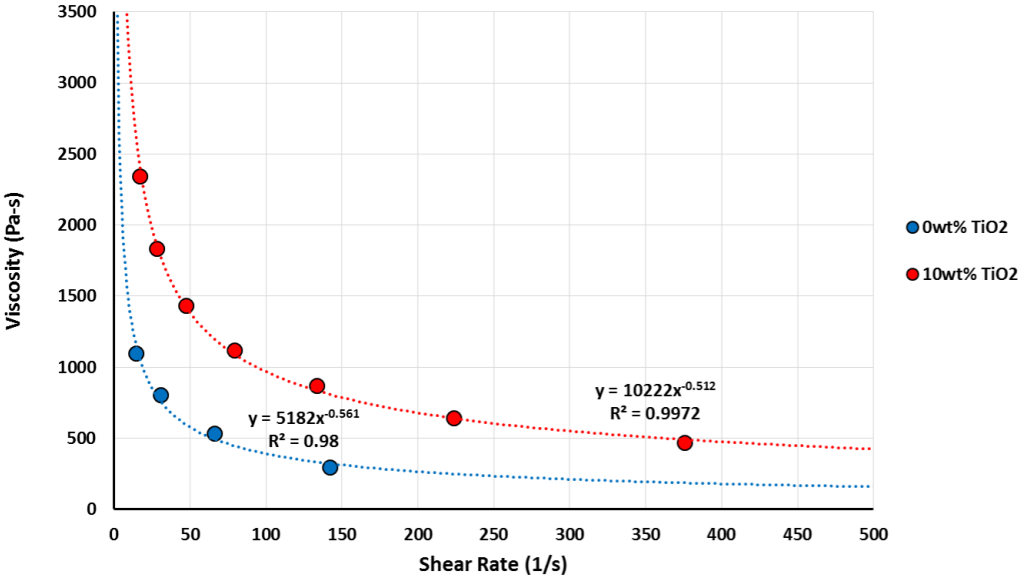

FIGURE 4.8: The viscosity and shear rate relationship for neat LDPE and LDPE with 10 wt% TiO_2.

For the RSD experiment, CAMES beads with a critical strength of 221 kPa were used. A total of .51 grams of CAMES beads were injected for every RSD measurement, while .63 grams of ink shots were used to measure the RTD.

4.2.2 Equipment

The extruder used for compounding was a 30 mm, bi-lobal, Werner & Pfleiderer fully-intermeshing, co-rotating TSE with a length-to-diameter (L/D) ratio of 39. The pre-blended LPDE/TiO_2 pellets were fed into an upstream, loss–in–weight feeder. Extrudate was collected from a strand die, plunged into a water bath, and pelletized. Three unique screw designs were tested during this experiment, with different mixing section geometries. The mixing section geometries are shown in Figure 4.9 below, and the full geometries can be found in Appendix B. The mixing sections were isolated in order to determine the stress developed only in those sections. Between the tracer injection port and the mixing section, only conveying elements were included so as to limit the generation of stress before the KB geometries.

The narrow KB screw geometry consists of six successive narrow KBs (KB45/5/14-RH), totaling 84 mm in length. This section is back by a 20/10RH and a 20/10LH element. The LH element fills up the narrow KBs, while the RH element was included to introduce a short section of a fully-filled conveying element over which the optical probe could be placed. Similarly, the wide KB screw geometry has two successive wide KBs (KB45/5/42-RH), totaling 84 mm in length. The same elements are included before and after the KBs. The mixing section 1 (MS1) screw geometry is a portion of the standard processing screw used by Chemours Inc. to compound LDPE and TiO_2. This screw design has a section of four narrow KBs, totaling 56 mm in length, followed by a 42/21RH conveying element. After the 42/21RH conveying element, two medium KBs

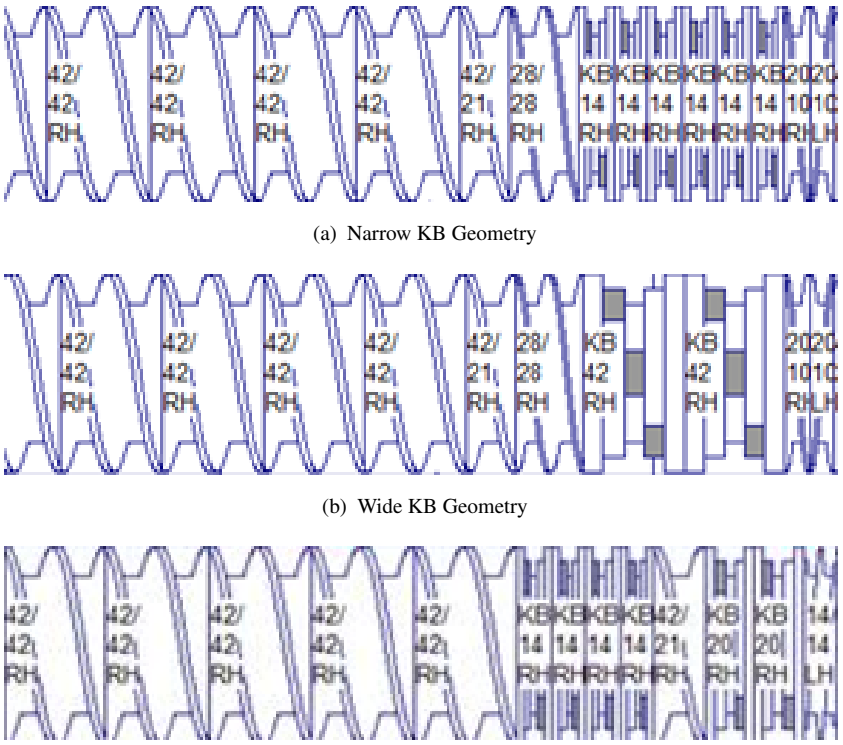

(a) Narrow KB Geometry

(b) Wide KB Geometry

(c) MS1 Geometry

FIGURE 4.9: The mixing section geometries evaluated during the RSD experiments.

(KB45/5/20-RH) are backed by a 14/14LH conveying element over which the optical probe was placed. The MS1 screw design will behave differently from the narrow and wide KB geometries. The 14/14LH conveying element will partially or fully fill the medium KBs, but it will not completely fill the upstream narrow KBs. Also, while the total length of KBs is similar between all three screw geometries (84 mm in the wide and narrow KB geometries and 96 mm in MS1), the KBs in MS have different paddles widths and are separated by a conveying element.

The temperature profile during processing is determined by the set temperature for each barrel (T_b). The temperature profile was design to maintain constant T_b in each mixing section, and is shown in Appendix B with the screw geometries. In general, the T_b was

set to 125°C in the mixing section and 150°C elsewhere. The low temperature in the mixing section increases the viscosity of the melt, increasing the shear stress developed in the mixing section.

4.2.3 Operating Conditions

Using the coordinate locations in Figure 3.5, nine sets of operating conditions were determined with varying N and Q/N. These conditions were selected encompass a range of standard processing conditions as well as produce a variable $\%BU$ response. The conditions shown in Figure 4.10 were repeated for narrow, wide, and MS1 screw geometries.

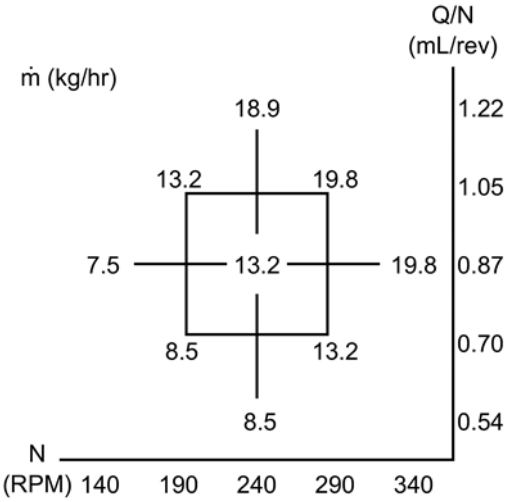

FIGURE 4.10: The operating conditions for the mixing section dispersion experiment.

4.2.4 Results

The RSD experiment was completed at every conditions shown in Figure 4.10 for all three screw geometries. The $\%BU$ values were generated from these results, and are shown in Figure 4.11.

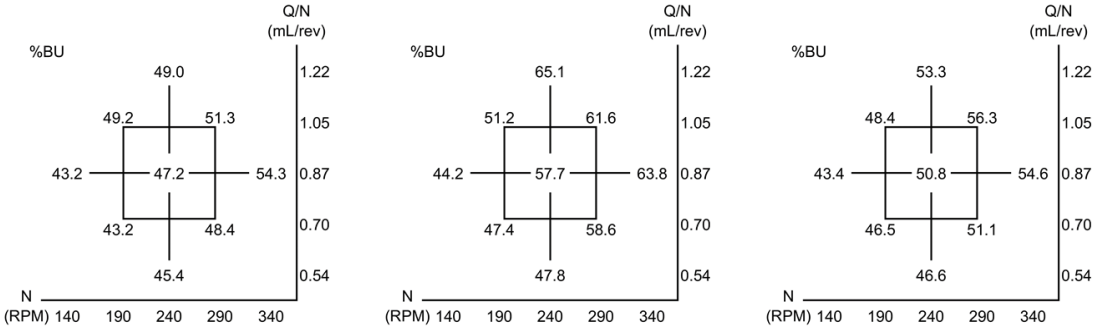

(a) Narrow KB (b) Wide KB (c) MS1

FIGURE 4.11: The $\%BU$ results for all three screw geometries.

The largest $\%BU$ values in Figure 4.11 were induced by the wide KB geometry, while the lowest $\%BU$ results belong to the narrow KB geometry. The MS1 geometry had $\%BU$ results lying in between the narrow and wide results. At the lowest N and Q/N conditions, the $\%BU$ is similar between all three geometries, with the responses diverging as N and Q/N increase. The wide KB geometry had the largest range in $\%BU$ across the operating domain (20.9 $\%BU$), indicating more control over the stress history with this geometry. The narrow KB and MS1 geometries had much lower ranges (11.1 and 12.9 $\%BU$ respectively), limiting the stress control with changes in operating conditions on these geometries.

Using the results in Figure 4.11, predictive equations were generated as a function of the significant operating conditions (α = .05) as explained in section 3.4.2. The equations

are shown in Table 4.3 with only significant coefficients and the intercepts. The R^2 term indicates how well the predictive equation fits the experimental data.

TABLE 4.3: Predictive equations for $\%BU$ with all three screw geometries.

Screw Geometry	Intercept	N	Q/N	R^2
Narrow	47.8	2.46	1.42	0.90
Wide	55.2	5.10	3.44	0.83
MS1	50.3	2.91	2.03	0.88

The equations in Table 4.3 indicate unique stress behavior with each screw geometry. For all three screw geometries, the only significant variables were N and Q/N as well as the intercept term. In addition, all geometries were more sensitive to N than Q/N across the operating domain. In order to compare the magnitude of the coefficients and intercepts, confidence intervals for each term were calculated. The intercept values for all three equations are compared in Figure 4.12, with the error bars representing 95% confidence intervals. In an equation with linear coefficients, the intercept term represents the average $\%BU$ over the entire operating domain.

Since the wide KB confidence interval does not intersect with any other geometry, it is concluded that the wide KB geometry generates a significantly higher average $\%BU$ across the operating domain than the other geometries: with the wide KB geometry, more material will experience 221 kPa of stress. With higher levels of stress, larger cohesive strengths can be overcome, and the minimum critical diameter for solid cluster rupture and erosion is decreased. The MS1 intercept is significantly lower than

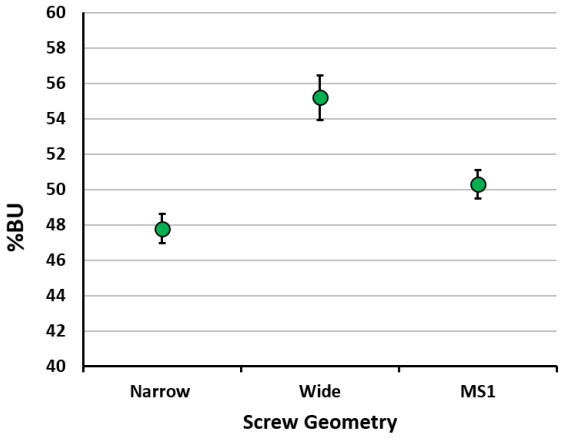

FIGURE 4.12: 95% confidence intervals for the intercept terms in the predictive equations.

the wide KB geometry, indicating that even with the increased total KB length (96 mm versus 84 mm), the medium and narrow KBs in MS1 cannot generate higher stresses than the wide KBs. In addition, the confidence interval for the MS1 geometry slightly overlaps the narrow KB interval, indicating similarity between the two geometries. The MS1 mixing section is comprised of 56 mm of narrow KBs, so similar behavior is expected. While the addition of 40 mm of medium KBs increased the stress developed in the MS1 geometry, it did not result in an average $\%BU$ significantly higher than the purely narrow KB geometry.

The confidence intervals for the N and Q/N coefficients are shown in Figure 4.13. The wide geometry is significantly more sensitive to changes in both N and Q/N than the narrow geometry. The MS1 geometry has coefficient values lying in between the narrow and wide KBs. The N coefficient for MS1 is significantly lower than the wide coefficient, but not significantly higher than the narrow value. For the Q/N coefficient,

MS1 is not significantly different from either the wide or narrow geometry. The combined behavior of the coefficients and intercepts indicates that the MS1 mixing section behaves similarly to a basic narrow KB geometry; none of the terms in the predictive equation are significantly different between the two geometries. Compared to the wide KB geometry however, MS1 generates significantly lower stress and is less sensitive to N.

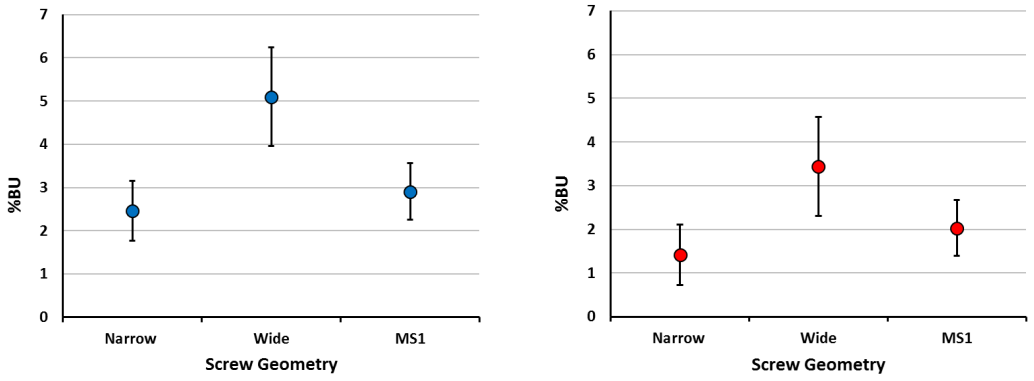

(a) Confidence intervals for N coefficients.

(b) Confidence intervals for Q/N coefficient.

FIGURE 4.13: 95% confidence interval analysis for coefficients in predictive equations.

In order to visualize the differences between predictive equations in Table 4.3 response surfaces were generated over the operating domain. The response surfaces for all three screw geometries are presented in Figure 4.14.

The wide KB geometry was more sensitive to N and Q/N, reflected in the large slopes of the wide KB surface. The top and bottom views of the response surfaces show a convergence of $\%BU$ results at low N and Q/N. The bottom view indicates the geometry that produces the lowest $\%BU$ at every set of operating conditions. While the majority of the bottom view is dominated by the narrow KB geometry, at the lowest N

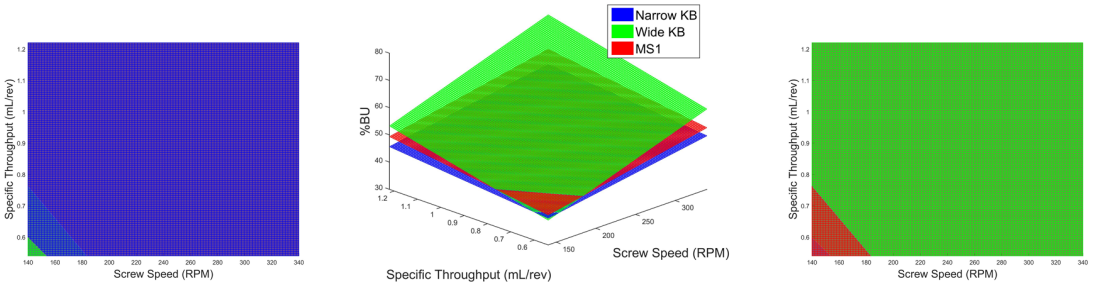

(a) Bottom View (b) Full View (c) Top View

FIGURE 4.14: Response surfaces for $\%BU$ with different view angles.

and Q/N, the wide KB geometry generates the lowest $\%BU$. The top view represents the geometry that results in the highest $\%BU$ across the operating domain. For most of the operating domain, the wide KB geometry generates the largests $\%BU$, however, again at low N and Q/N, the MS1 geometry results in the highest stress levels. The overlapping behavior of all three geometries at low N and Q/N indicates that screw geometry does not affect the flow of the melt at low shear rates and degree of fill. At low N and Q/N, the geometries converge to a baseline behavior.

4.2.5 Discussion

Results from this experiment indicates that the MS1 geometry behaves similarly to the narrow KB geometry, even with the inclusion of the medium KBs, a RH conveying element, and a unique LH pressure-building element. However, the MS1 behavior was significantly different than the wide KB geometry, indicated by the difference in intercepts and N coefficient. These two relationships indicate that paddle width is the most significant parameter effecting the stress magnitude and sensitivity within the mixing

section. Even with the differences between the narrow KB and MS1 geometry, the similarity between the KB paddle widths resulted in similar $\%BU$ response. However, the wide KBs have more than double the paddle width of the KBs in MS1 therefore inducing significant differences in $\%BU$ behavior.

Paddle width has been previously determined to affect the stress behavior in a mixing section [61]. This is due to wider paddles providing a greater obstruction in the flow, with the intermeshing of these paddles resulting in rapid accelerations of the melt. These high accelerations are critical in order to achieve significantly higher shear stresses, due to the shear-thinning behavior of the melt. Figure 4.15 shows the relationship between shear rate and shear stress for LDPE and LDPE with 10 wt% TiO_2. This figure is a re–representation of the data presented in Figure 4.8.

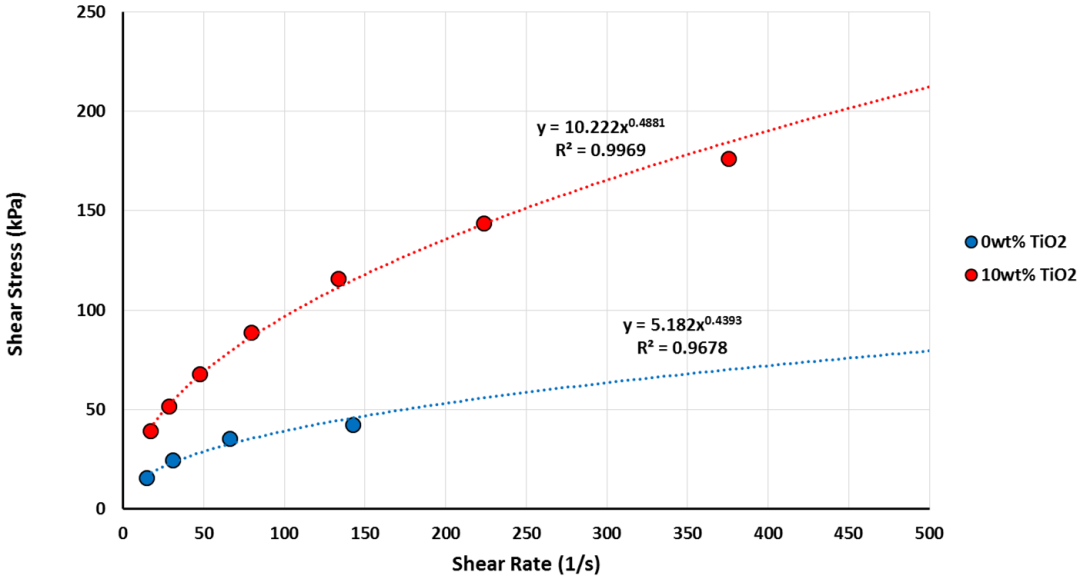

FIGURE 4.15: The viscosity and shear stress relationship for neat LDPE and LDPE with 10 wt% TiO_2.

As seen in Figure 4.15, at low shear rates large increases in shear stress can be obtained

with incremental increases in shear rate. However as shear rate is increased, the material shear-thins due to the aligning and disentangling of the polymer chains. This results in shear stress gradually increasing as shear rate increases. In order to overcome the shear-thinning behavior and achieve significantly higher shear stresses, large shear rates need to be obtained. The rapid accelerations caused by wide KB paddles provide the large shear rates required to achieve improvements in shear stress.

4.3 Conclusions

Results from the RSD experiment indicate that the MS1 mixing section generates weaker stresses with less process control than a wide KBs mixing section. The wide KBs generate higher accelerations in the melt, which increases the average shear stress in the melt as well as the sensitivity of shear stress to N. Considering just the numerator of the Fa number, the wide KB geometry will generate higher hydrodynamic stresses and improve the quality of dispersion. With larger stresses, the minimum cluster diameter will decrease and the likelihood of rapid rupture will increase for all cluster sizes. However, these experiments do not consider the effect of screw geometry on the cohesive strength of the clusters, the denominator in the Fa number. Cohesive strength is a function of several variables and can be affected by the screw geometry. Narrow KBs may better distribute the agglomerates and aggregates, increasing the infiltration of the melt and improving the dispersion [3, 8, 69]. In addition, the presence of a RH element between KB sections (the 42/21RH element in MS1) may reorient and reset the flow,

ensuring a more even distribution of cluster diameters. Evaluation of the effect of screw geometry on these cohesive strength parameters requires off-line analysis of extruded samples. The benefit of the RSD experiment is that it can be applied to a continuous process to determine the variation in the hydrodynamic stresses inducing dispersion. While the $\%BU$ does not completely predict dispersion, it is an essential comparative tool to relate operating conditions and screw geometry to the dispersing potential of a process.

Chapter 5

Pharmaceutical Extrusion Process-Property Relationship

Twin-screw compounding has been heavily studied in the pharmaceutical realm due to its ability to improve bioavailability of a poorly soluble API by dissolving the API in a water-soluble polymer. While twin-screw extruded drugs can achieve more efficient dissolution after ingestion, extrusion can also induce adverse properties in the final product. Extrusion has been shown to degrade the API, which has been previously attributed to the high temperatures and long exposure times in a TSE [11, 12, 76, 85]. In addition, water content in an extruded drug can cause the API to recrystallize, resulting in inferior and unpredictable dissolution behavior.

In this experiment, the crystallinity, API degradation, and water content of a pharmaceutical extruded composite is investigated. Specifically, the effect of the operating

conditions of N, Q/N, and T_b is determined. By establishing the response of key pharmaceutical properties to the controllable operating conditions, optimal processes can be designed. In addition, developing the property response interactions will allow for intuitive evaluation of trade-offs in a pharmaceutical extrusion process.

After determination of properties, the property response will be related to scale independent parameters that represent the physical interactions occurring within the TSE. The RSD will be used to generate the $\%BU$ as a representation of the degree of stress developed in the melt. In addition, the T_{melt} and t_{mean} will be used to determine the effect of temperature and time respectively. Consideration of these three properties will allow for future development of physical relationships between different extruder scales.

5.1 Experimental Procedure

5.1.1 Materials

The polymer carrier used in this study was copovidone of brand Kollidon VA 64, manufactured by BASF. Kollidon VA 64 is water-soluble, encouraging its use as a solvent in solid dispersion formulation. This polymer is also hygroscopic, absorbing and retaining water. The glass transition temperature of Kollidon VA 64 is approximately 101°C. The viscosity of Kollidon VA 64 varies depending on temperature and shear rate. Experimental plots of shear rate versus viscosity are shown in Figure 5.1, measured using a

cone and plate rheometer. Kollidon VA 64 has increasing viscosity as temperature decreases. In addition, as the temperature decreases, the shear-thinning behavior becomes more pronounced.

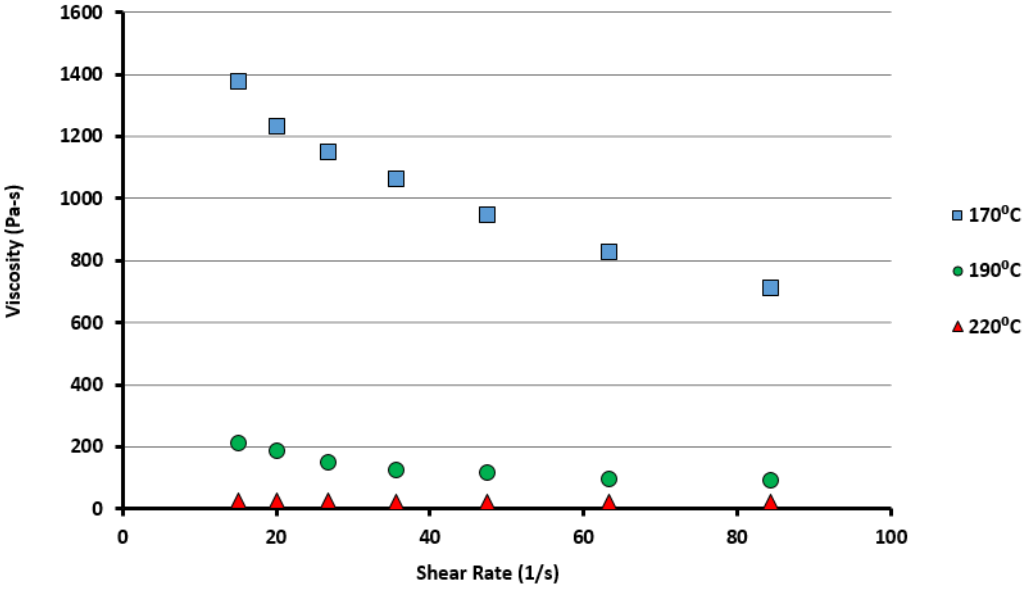

FIGURE 5.1: Viscosity versus shear rate for Kollidan VA 64 at various temperatures.

The active pharmaceutical ingredient (API) in this experiment was provided by Merck & Co., Inc. and will be termed MK-A. This API is a tri-hydrate, releasing water as it transforms from crystalline to amorphous form. Kollidon VA 64 and MK-A were compounded with a surfactant resulting in a final weight ratio of 72/23/5 of carrier/API/-surfactant. The surfactant lowers the glass transition temperature of the carrier during processing and improves the solubility of the API [94]. Before extrusion, the blend was mixed in a powder mixer to ensure uniform concentration during feeding.

During extrusion, TiO_2 was added to the carrier/API/surfactant melt in order to give the melt an opaque white color used to establish the baseline for RSD experiments. The

TiO_2 was added at rates corresponding to 2 wt% of the feed rate at each condition. TiO_2 is relatively dense so a 2 wt% concentration represents an even lower volume concentration. Preliminary analysis indicated that pharmaceutical property testing was not influenced by the presence of TiO_2.

The RSD measurements required the ink shots and CAMES beads presented in section 4.2.1. At every operating condition, two ink shots were dropped to measure RTDs, with each shot weighing 0.32 g. Three CAMES drops were completed at every operating condition as well, with a weight of 0.25 g of CAMES beads per drop. These weights were selected to ensure the ink shot represented 100 $\%BU$. The CAMES for this experiment had a failure strength of 194 kPa.

5.1.2 Equipment

For this experiment, a 16 mm Thermo extruder with an L/D of 40 was used for all compounding. The carrier/API/surfactant blend was fed at the furthest upstream port on the extruder. A separate feeder was used to feed the TiO_2 into the same port. The extruder screw geometry consisted of a melting and mixing section, separated by a section of purely conveying elements. In this conveying section, an open-air vent was included to allow for escape of evaporated vapors. The mixing section was built-up from individual kneading paddles to form KB elements. The individual paddles had an axial length of 4 mm and could be staggered incrementally. The furthest upstream element in the mixing section consisted of five consecutive paddles, staggered in 30°

increments. This combined KB element was geometrically similar to a standard narrow KBs. After this element, five more mixing paddles were placed, each staggered at 60°. It was theorized that the larger stagger angles would behave similarly to wide KBs, due to the increase in backflow and poor conveying ability. This element was followed by neutral KBs that were constructed by staggering ten successive paddles at 90° angles.

Property testing was completed for each condition by collecting extrudate formed by the die. For most conditions, a cylindrical die was used to form the composite (Figure 5.2), however, at some low temperature conditions the melt would freeze within the die so it needed to be removed. For water content testing, the collected extrudate was immediately placed in specialized vials in order to seal in the moisture content.

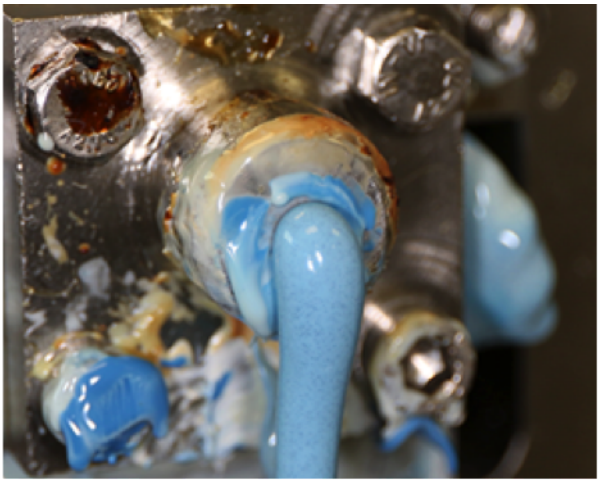

FIGURE 5.2: Extrudate exiting cylindrical die during pharmaceutical extrusion experiment (*Courtesy of Paul Blanchette, Merck & Co., Inc.*)

Crystallinity testing was completed using x-ray diffraction (XRD) of the samples at each condition. The presence of crystalline API in the composite creates a sharp peak in the diffraction pattern: fully amorphous API would not induce these peaks. The measured crystallinity was assessed as a binary threshold value for the magnitude of the

diffraction peaks and the presence of crystallinity will be reported as either a "Yes" or "No" state for analysis.

For water content testing, the sealed vials collected during the experiment were allowed to equilibrate for at least 24 hours at 25°C before an initial measurement, and were re-measured after 72 hours to ensure adequate equilibration. Measurements were performed using a Lighthouse Instruments FMS-1400H Water Activity Analyzer that measured the relative humidity ($\%RH$) in the vial by passing a laser through vial headspace to measure the moisture content.

Degradation of the API was measured using a reversed-phase high-performance liquid chromatography (HPLC) method. This method measures the amount of degraded API in the extrudate. Due to initial small concentration of degradation prior to processing extrusion, degradation results are present as a percent growth in degradation from initial (%deg). All pharmaceutical property testing was completed by colleagues at Merck & Co., Inc.

The RSD testing was completed with the same method and equipment presented in Chapter 3.

5.1.3 Experiment and Operating Conditions

The response of pharmaceutical properties to changes in operating conditions was investigated using CCD grids (Section 3.4.1). The CCD grid allowed for evaluation of a response over a range of two operating conditions (N and Q/N) and determination

of significant effect. Similar to the RSD analysis introduced in Section 3.4.2, the pharmaceutical property CCD grids were used to generate predictive equations for response surfaces over the operating domain. The operating conditions for the CCD grids is shown in Figure 5.3 with the feed rate shown at every tested set of operating conditions. The pharmaceutical properties measured at each operating condition were crystallinity, degradation ($\%deg$), and water content ($\%RH$).

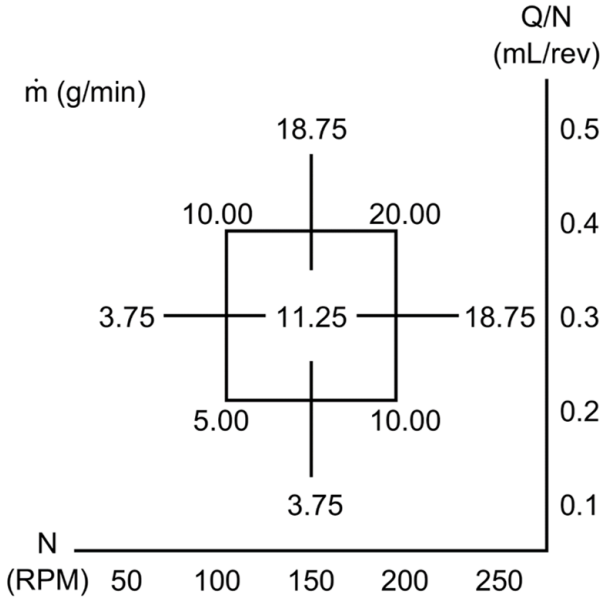

FIGURE 5.3: 2D CCD grid operating conditions for pharmaceutical property experiment.

Due to the significance of T_b on pharmaceutical properties, the CCD grid in Figure 5.3 was replicated three times for the following T_b: 170, 190, and 220°C. These temperatures were selected to encompass a range of feasible operating conditions for this compounding process. A T_b of 160°C was initially tested, but the composite melt could not exit the extruder without freezing. T_b above 220°C were not considered due to the extreme and unfeasible property response predicted above that temperature.

After each CCD grid was evaluated at an independent T_b, they were combined and evaluated by transforming the T_b into the CCD domain. Representation of T_b as a continuous variable allowed for creation of a single predictive equation. The T_b was normalized from 170, 190, and 220°C to -1.33, 0, 2.00 respectively in the CCD coordinate domain in order to compare its effect to the effects of N and Q/N. This 3-D space is represented physically in Figure 5.4.

For the 2-D predictive equations, in order to select the predictor terms to include in predictive equation the top down analysis method was used, as introduced in Section 3.4.2. In the 3-D predictive equations, the predictor terms included in each model were determined by the adjusted R^2 resulting from the inclusion of successive predictors. This method was used to limit the number of predictors when considering a model with nine predictors and an intercept term. The model was formed by adding significant predictors until the adjusted R^2 no longer increased. At this point, the model was abridged to include only the significant predictors that improve the adjusted R^2 term.

At every condition tested for pharmaceutical property response in Figure 5.3, the RSD experiment was completed to evaluate the stress developed in the melt, quantified by $\%BU$. Correlations between the pharmaceutical properties, operating conditions, and scale-independent parameters (such as the $\%BU$) were investigated.

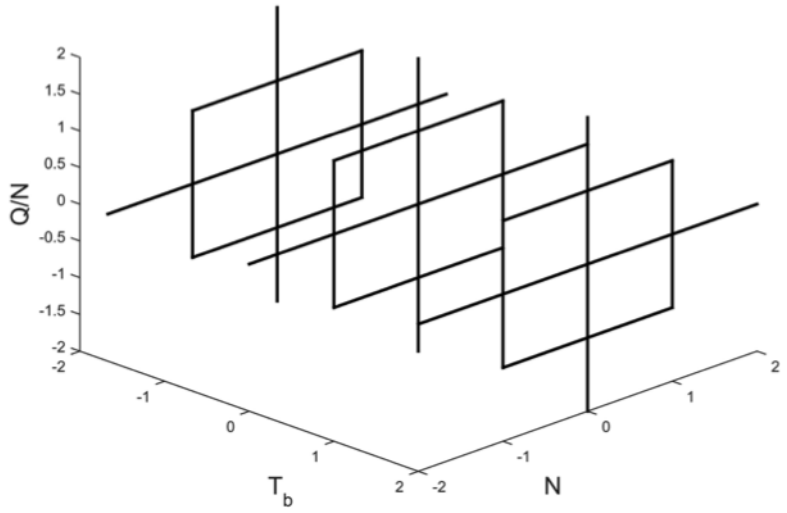

FIGURE 5.4: 3D representation of combination of 2D CCD grids.

5.2 Pharmaceutical Property Results

The results will be presented independently for each pharmaceutical property tested. Initially, 2-D CCD grid results will be discussed, resulting in a separate predictive equation at each T_b for every property. The 2-D CCD grid results are generated using the operating conditions shown in Figure 5.3. These N and Q/N conditions were held constant at all three T_b (170, 190, and 220°C), resulting in the same nine feed rates between grids. This will be followed by 3-D analysis where T_b is including as a continuous variable and a single predictive equation is generated for each property as a function of N, Q/N, T_b and any higher order terms.

5.2.1 Water Content

5.2.1.1 2-D Analysis

The 2-D results for the water content are shown in Figure 5.5, for all three T_b. The value at each coordinate location represents the $\%RH$ measured from the produced extrudate.

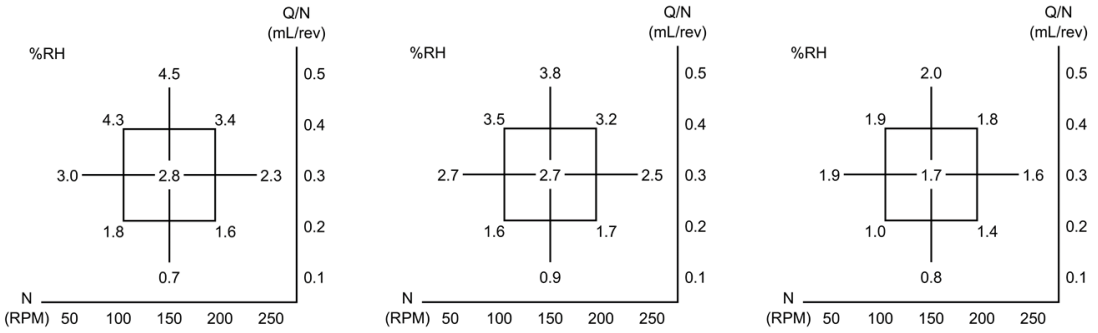

(a) 170°C (b) 190°C (c) 220°C

FIGURE 5.5: The 2-D water content results for all three T_b.

From Figure 5.5, the 170°C condition has the largest range in $\%RH$ values. At 150 RPM, the $\%RH$ was 4.5 at 0.5 mL/rev and 0.7 at 0.1 mL/rev, the maximum and minimum $\%RH$ values among all tested operating conditions. While the 170°C grid had the single lowest $\%RH$ value, overall it had the highest average water content, followed by the 190°C grid, which demonstrated similar behavior. The 220°C grid had the lowest average $\%RH$ and behaved uniquely. The highest water content on the 220°C grid was 2.0 $\%RH$: six conditions on both the 170 and 190°C grids had higher water content than 2.0 $\%RH$.

From the 2-D water content results, predictive equations were generated for the $\%RH$ response for each T_b . The equations were evaluated as a function of an intercept, N, Q/N,

and second order terms and interactions, but only significant terms (α = .05) were included in the final equations. The equation are shown in Table 5.1, with each column corresponding to either the intercept or coefficient term in the predictive equation. The N^2 and $(Q/N)^2$ coefficients were not significant, so their columns are not included in the table. If a variable was not significant at a certain T_b, its coefficient is represented with a "-". The R^2 term indicates how well the predictive equation fits the experimental data.

TABLE 5.1: Predictive equations for water content at three T_b

T_b (°C)	Intercept	N	Q/N	Q	R^2
170	2.72	-0.21	0.99	-0.17	0.99
190	2.51	-	0.77	-	0.97
220	1.57	-	0.31	-	0.80

The equations in Table 5.1 reflect the behavior seen in the 2-D CCD results. As the T_b increases, the intercept values decreases. The largest coefficients belong to the 170°C condition, reflecting the large range of the 170°C grid. Only at 170°C were N and Q significant, although their coefficients were relatively small compared to Q/N. The Q/N coefficient was significant at all three T_b, indicating that the degree of fill in the screw channels is the strongest determinant of water content at a constant T_b. The magnitude of the Q/N coefficient decreased as T_b increased, suggesting a decreased sensitivity to Q/N at higher temperatures.

The unique behavior of the three predictive equations is further clarified by generating response surfaces. These surfaces are created by mapping the $\%RH$ results predicted

by the equations across the CCD grid operating domain of N and Q/N. In Figure 5.6, the three T_b response surfaces are shown on the same axes.

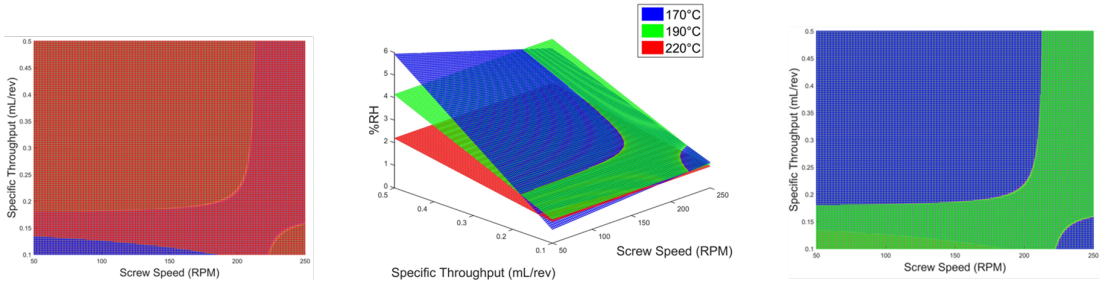

(a) Bottom View (b) Full View (c) Top View

FIGURE 5.6: Response surfaces for water content with different viewing angles.

The response surfaces illuminate the differences between the predictive equations. In the 3-D view of the surfaces, there are clear differences in the surface slopes at different T_b. The 170°C surface has the steepest slope, due to the large magnitude of its Q/N coefficient. This steep slope implies greater process variability and control, which may or may not be desired for a process design. If a process requires precise control over the water content, processing at low temperatures would be preferable. However, if a single, low water content is required, processing at high temperatures allows an operator to change N and Q/N to affect other properties without altering the water content.

The top and bottom views of the response surfaces show which T_b results in the maximum and minimum water content across the tested operating domain. For the majority of the bottom view, the 220°C surface results in the lowest $\%RH$. With the top view, the 170°C surface results in the lowest water content, except for at low Q/N and high N. At

low Q/N, there is significant overlap between all three surfaces, which indicates a convergence of water content behavior regardless of T_b. At low Q/N, the screw channels are relatively empty, so there is less material to devolatilize per revolution and therefore the water can easily reach the surface and evaporate. At high N, the 190°C surface results in higher water content than the 170°C surface, due to the negative N coefficient in the 170°C equation. This can again be explained by convergent behavior. At high N, the viscous heating begins to influence the melt temperature more significantly than a 20°C difference in barrel temperature.

5.2.1.2 3-D Analysis

In order to analyze the effect of T_b as a variable, the T_b was normalized and included in the standard least-squares fit for $\%RH$ along with the second order term and all interactions. The 3-D predictive equation for $\%RH$ is shown in Equation 5.1 with only significant terms (α = .05). The predictive equation for $\%RH$ has an R^2 value of 0.94.

$$\%RH = 2.35 + 0.74\frac{Q}{N} - 0.36T_b - 0.20\left(T_b \cdot \frac{Q}{N}\right) \tag{5.1}$$

Besides the intercept term, in Equation 5.1 the $\%RH$ across the operating domain is only a function of T_b, Q/N, and their interaction. The N and Q coefficients that were significant at 170°C are not significant when considering all T_b. The intercept in Equation 5.1 (2.35) is similar to intercept in the 2-D, 190°C equation (2.60), which is expected if all operating conditions are set to coordinate zero. The Q/N coefficient is the

largest coefficient in the 3-D predictive equation, indicating it is the most significant operating condition to affect water content across the tested operating domain. However, Equation 5.1 also indicates that T_b has a significant effect on water content, an effect predicted by the difference in equation intercepts in Table 5.1. The difference in Q/N coefficients in Table 5.1 is reflected in the significant Q/N and T_b interaction in the 3-D equation. Increasing T_b serves to dampen the effect of Q/N on water content, an effect seen in the flattening of the response surfaces in Figure 5.6.

5.2.1.3 Discussion

Results from water content analysis indicate a clear significance of two operating conditions, Q/N and T_b, on the water content. The operating conditions Q/N was shown to have the strongest effect on $\%RH$, with increases in Q/N increasing the $\%RH$ linearly. The significance of Q/N is due to the effect of surface-to-volume ratio on ease of devolatilization. At low Q/N, the surface-to-volume ratio is much higher, providing more avenues for vapor removal per unit volume. Increasing the T_b was shown to decrease the $\%RH$ significantly as well. This can be attributed to high T_b increasing the melt temperature, adding heat to drive evaporation and decreasing the melt viscosity. Lower melt viscosity will allow vapor bubbles to more easily escape the melt.

Through both 2-D and 3-D analysis, a interaction between Q/N and T_b was determined. As T_b increased, the 2-D equations displayed decreased sensitivity to Q/N resulting in a significant interaction term in the 3-D equation . The response surfaces also displayed a

convergent behavior at low Q/N regardless of T_b . At low Q/N, the negative coordinate values would result in a positive value for the interaction term in Equation 5.1, resulting in the dampening of temperature significance. This behavior has been attributed to low volumetric fills dominating the devolatilization behavior. At low Q/N, the small melt volume in each screw channel can be devolatilized rapidly to a near-zero value regardless of temperature effects.

Although it has been predicted by devolatilization theory, there was no significant effect of N on the water content. The increased surface regeneration from increased N did not result in reduced water content, which may be attributed to two likely causes. The impact of N may be insignificant in comparison to the other examined operating conditions. Although the 3-D predictive equation does not consider N significant, the constant N conditions on the CCD grids shows some variability in $\%RH$ with changes in N, especially at the 170°C . However, these changes in $\%RH$ are much smaller than the effects of Q/N and T_b, and in comparison, appear insignificant.

It is also possible that the operating condition N affects other variables within the process besides the surface regeneration, resulting in competing effects. In addition to the surface regeneration, increasing N decreases the melt viscosity through viscous heating and shear-thinning effects (Figure 5.1), which would allow vapor bubbles to more easily escape the melt. However, increasing N will decrease the mean residence time (Equation 2.2), limiting the time available for the hot barrels to drive evaporation of vapor from the melt. Regardless of competing physics within a TSE, during processing the

operator can only change the operating conditions to influence the final product characteristics. In regards to water content, only by decreasing Q/N and increasing T_b can an operator ensure decreases in water content across this operating domain.

5.2.2 Degradation

5.2.2.1 2-D Analysis

The three T_b CCD grid results for degradation are shown in Figure 5.7. The value displayed at each coordinate represents the $\%deg$ measured in the extrudate. As mentioned in Section 5.1.1, the $\%deg$ represents the increase in degraded material from pre- to post-processing.

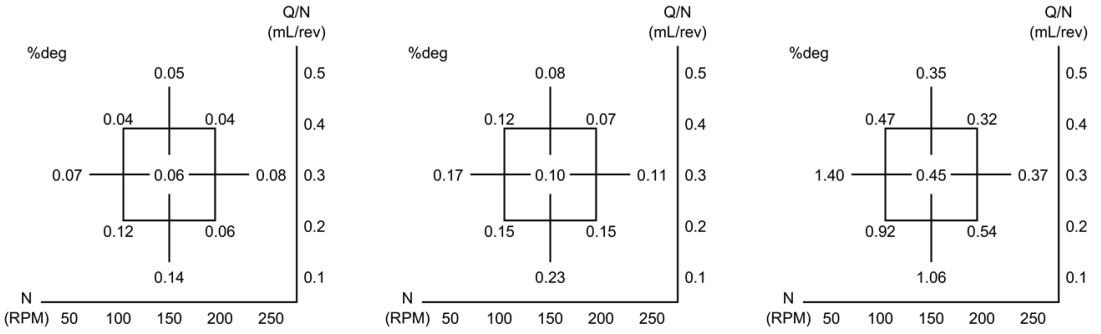

(a) 170°C (b) 190°C (c) 220°C

FIGURE 5.7: The 2-D degradation results for all three T_b.

While the 170 and 190°C results were similar, the degradation response at 220°C was unique. The lowest $\%deg$ at 220°C was 0.32, while the highest $\%deg$ on either of the lower temperature grids was 0.23. The 220°C grid also had the highest range in

$\%deg$ values between all T_b tested. The 220°C grid had a range of 0.74 $\%deg$, while the 170 and 190°C grids had a range of 0.10 and 0.16 $\%deg$ respectively.

Using the $\%deg$ results from the CCD grids, predictive equations were generated at every T_b as a function of N, Q/N, and their second order terms and interactions. The equations are shown in Table 5.2 with all intercept and coefficient terms. The N and Q/N interaction (Q) and $(Q/N)^2$ were insignificant (α = .05) at all T_b , so they were not included in Table 5.2.

TABLE 5.2: Predictive equations for degradation at three T_b

T_b (°C)	Intercept	N	Q/N	N^2	R^2
170	0.07	-	-0.02	-	0.71
190	0.13	-	-0.03	-	0.71
220	0.65	-0.22	-0.17	0.12	0.80

The results in Table 5.2 clarify the differences seen in the CCD results. The intercept and coefficients values for the 170 and 190°C equations are similar in magnitude, while the 220°C values are considerably higher. The intercept value at 220°C is five times higher than the 190°C intercept and nine times higher than the 170°C intercept. This change in intercept indicates T_b has a significant effect on $\%deg$ response. In addition, changes in T_b affected the sensitivity of $\%deg$ to the changes in N and Q/N. Although Q/N was significant across all T_b, the sensitivity was much higher at 220°C. While the magnitude of the Q/N coefficient was highest at 220°C, the N coefficient had the largest magnitude at this T_b . In addition to N and Q/N, the N^2 coefficient was significant at different 220°C.

The equations in Table 5.2 indicate several complex relationships between the operating conditions and $\%deg$ response. To clarify the predominant relationships, response surfaces for each T_b are plotted together in Figure 5.8.

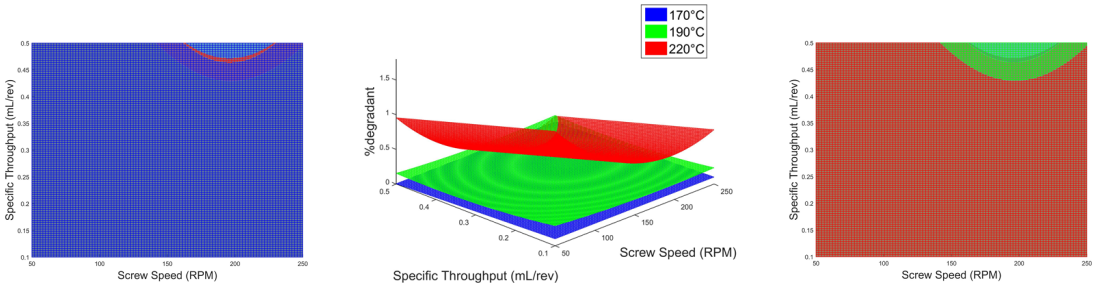

(a) Bottom View (b) Full View (c) Top View

FIGURE 5.8: Response surfaces for degradation with different viewing angles.

The response surfaces in Figure 5.8 clearly show the unique behavior of the 220°C property response compared to the lower temperatures. The 170 and 190°C surfaces are relatively flat, with near constant, low degradation values. The 220°C surface has a quadratic behavior, with very high degradation at low N.

The bottom view of the response surfaces is dominated by the 170°C surface, with a slight overlap from the 220°C surface at a high Q/N and high N condition. Similarly, the top view is dominated by the 220°C surface with an overlap with the 190°C surface at high N and high Q/N. The overlaps in both the top and bottom views occur at low $\%deg$ values. This indicates that at the largest N and Q/N operating conditions the effect of T_b is overcome and the degradation is minimized. At high Q/N, this can be attributed to the reduced total revolutions (Equation 2.3) or total strain the melt experiences in the extruder. At high N, the residence time is decreased (Equation 2.2) and the melt has less time at high temperatures. In order to clarify the significance of

these relationships across the entire operating domain, the 3-D predictive equation was generated.

5.2.2.2 3-D Analysis

The 3-D equation for degradation response is shown in Equation 5.2 as a function of significant variables (α = .05). The predictive equation for $\%deg$ has an R^2 value of .90.

$$\%deg = 0.13 + 0.13T_b - 0.07\frac{Q}{N} - 0.06N - 0.07(N \cdot T_b) + 0.07T_b^2 - 0.05\left(\frac{Q}{N} \cdot T_b\right) \quad (5.2)$$

Equation 5.2 has the N and Q/N coefficients seen in the 2-D equations in Table 5.2 as well as several newly significant coefficients. With six total coefficients, physical effects cannot be isolated, however, conclusions can be drawn based on the magnitude and sign of the coefficients. The largest coefficient in Equation 5.2 is the first order T_b coefficient (0.13). Considering the ${T_b}^2$ coefficient is also positive and large (0.07), it is clear than increasing T_b will increase the total degradation of the API. This can be attributed to increases in melt temperature driving the degradation reaction.

Evidence for the residence time affecting the degradation is inconclusive. At low T_b, increasing N increases the degradation. However, these degradations occurring at low T_b will generally not increase the degradation more than 0.03 $\%deg$ across this operating domain. At as T_b increases to neutral of positive coordinate values, increases in N

signficantly decreases the degradation. At 220°C and a constant Q/N, increasing N can decrease the degradation by 0.50 $\%deg$. Although mean RTD is also affected by Q, Q is not present in Equation 5.2.

The Q/N operating condition also displays similar dependence on T_b as the N operating condition. At the lowest T_b and a constant N, increasing Q/N increases the degradation approximately 0.10 $\%deg$ across the tested domain. However, at the largest T_b, across the Q/N operating domain the $\%deg$ can decrease about 0.80 $\%deg$ with increases in Q/N. This Q/N effect indicates that shorter flow paths result in less degradation of the API at higher temperatures. By decreasing the total strain of the melt, degradation can be reduced even at high T_b, as seen in the convergent response surface behavior.

The contradictory behavior of N and Q/N at low T_b is likely due to the low resolution of the degradation response at 170°C. Across the 170°C operating domain, the $\%deg$ response is low and the range $\%deg$ is small. However, at the highest T_b there are significant differences in $\%deg$ across the operating domain.

5.2.2.3 Discussion

The degradation results demonstrate a clear influence of T_b on degradation of the API. From the 2-D analysis, there appears to be a temperature threshold. In the 2-D equations (Table 5.2), the intercept and coefficient values are similar at 170 and 190°C, but significantly higher at 220°C. In the 2-D response surfaces the 220°C surface is significantly higher than the lower temperature surfaces. This threshold behavior is similar to

the relationship observed by Feng et al. for an API compounded with PVP, and previously shown in Figure 2.17 [91]. With MK-A, results indicate an activation T_b for the degradation of the API between 190 and 220°C . Experiments at smaller T_b intervals are required to determine the exact threshold temperature.

The operating Q/N was also shown to have a conclusive effect on the degradation of MK-A. Increases in Q/N decrease the mean number of residence revolutions, or the total strain of the melt through the extruder, resulting in decreases in degradation. The Q/N has also been shown to significantly affect the stress history in a TSE [57], a relationship that will be investigated in Section 5.4.

From operating condition analysis, the t_{mean} did not appear to have a conclusive effect on degradation, contrary to typical pharmaceutical extrusion theory [11, 12, 76, 85]. While N had a conclusive effect at high T_b, Q, did not have a significant effect on degradation. While decreasing the residence time may reduce degradation, increasing N introduces other physical behavior that may induce degradation, such as viscous heating; the effect of melt temperature on degradation was established with T_b so viscous heating may introduce a significant effect. In addition, increasing N increases the stress developed in a TSE [56, 57], which may induce degradation. The other variable in the mean residence time equation, Q, was not found to be significant in the 2-D or 3-D equations. The relationship between t_{mean} and $\%deg$ will be directly investigated in Section 5.4

5.2.3 Crystallinity

5.2.3.1 Analysis

Crystallinity results were reported on a Yes/No basis, indicating whether or not crystalline API was observed in the extrudate. If the XRD had crystalline intensity peaks, crystallinity was reported as "Yes" while the presence of no peaks was denoted with a "No" response. The three T_b CCD grids for crystallinity are shown in Figure 5.9.

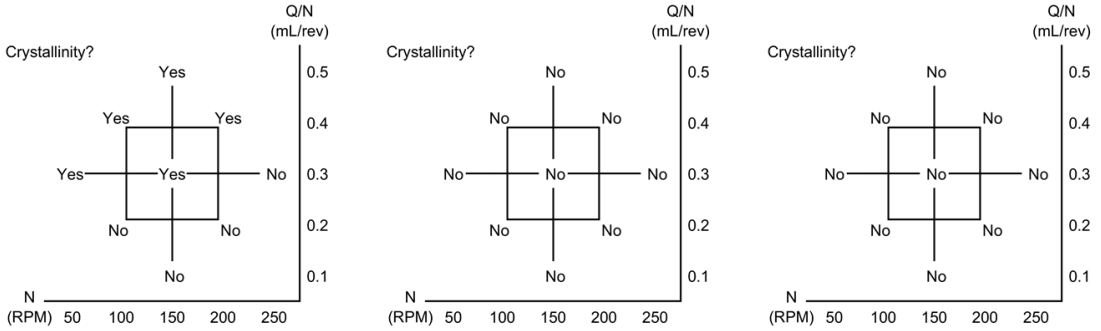

(a) 170°C (b) 190°C (c) 220°C

FIGURE 5.9: The 2-D crystallinity results for all three T_b.

The only CCD grid in Figure 5.9 with a crystalline API response is the 170°C grid, indicating a strong dependence of crystallinity on temperature. On the 170°C grid, five sets of operating conditions produced extrudate with crystalline API. The API crystallized at the three highest Q/N conditions, as well as two of the three intermediate Q/N conditions. The intermediate Q/N condition that did not result in crystallinity was processed at the highest N level. These results indicate that in addition to T_b, API crystallinity is strongly dependent on the degree of fill within the screw channels, but this effect can be mitigated by increasing the screw speed.

5.2.3.2 Discussion

The crystallinity results show that T_b, Q/N, and N all had a significant effect on the crystallization response. The T_b was the most significant operating condition, eliminating crystalline response at T_b of 190°C and above. This is consistent with the results observed by Shibata et al., and pictured in Figure 2.15, where increases in T_b decreased the amount of crystalline material [80]. Higher T_b increases melt temperature, which encourages dissolution of the API into the polymer matrix. Similarly, high N was shown to decrease crystallinity, possibly due to increases in the melt temperature by viscous heating, even though the residence time is decreased; Shibata et al. and Nakamichi et al. found that short residence time result in a larger amount of crystalline API [80, 81].

At a constant temperature, results showed that Q/N was the most significant operating condition. At 170°C, five of the six highest Q/N conditions resulted in crystallinity. As Q/N increases, the number of revolutions for the melt decreases (Equation 2.3), limiting the total strain of the melt. This could result in areas of high concentration of undissolved API that are not distributed and dissolved prior to exiting the die.

5.3 Percent Break-up Results

The RSD experiment was completed while samples were collected for pharmaceutical property measurements. The $\%BU$ values were measured at every condition pharmaceutical property testing was completed in order to determine if there were significant

relationships between the stress developed and the property response. The stress beads used for this RSD experiment had a failure strength of 194 kPa, so the $\%BU$ indicates what percentage of the melt experiences a stress greater than or equal to 194 kPa. The bead strength was selected in order to achieve a range of $\%BU$ within the operating condition domain.

5.3.1 2-D Analysis

The three constant T_b CCD grids for $\%BU$ are shown in Figure 5.10. The $\%BU$ values for every set of operating conditions is indicated at each coordinate location.

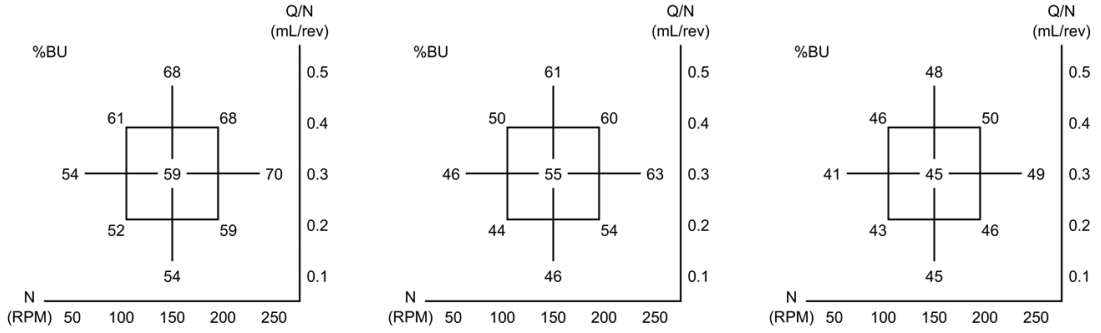

(a) 170°C (b) 190°C (c) 220°C

FIGURE 5.10: The 2-D percent break-up results for all three T_b.

In Figure 5.10, there are differences in the magnitude of $\%BU$ response between T_b grids. The 170°C grid had the largest $\%BU$ values, while the 220°C grid had the smallest. All three grids showed the expected correlation between increasing $\%BU$ with increases in N and Q/N, however, the magnitude of the correlation differed between T_b. Increasing N and Q/N on the 170 and 190°C grids resulted in $\%BU$ changes as large as 18 and 19

$\%BU$ across the 170 and 190°C grids respectively. On the 220°C grid, the sensitivity to N and Q/N was much lower, with a maximum difference across the grid of 9 $\%BU$.

From the 2-D $\%BU$ results, predictive equations were generated as a function of significant operating conditions. The equations are shown together in Table 5.3 with only significant operating conditions (α = .05). Only the intercept, N, and Q/N were significant.

TABLE 5.3: Predictive equations for $\%BU$ at three T_b

T_b (°C)	Intercept	N	Q/N	R^2
170	60.0	3.42	4.25	0.89
190	53.2	4.50	3.50	0.96
220	45.9	1.92	1.08	0.90

The equations in Table 5.3 show similarities and differences between $\%BU$ behavior at different T_b. As the T_b increases, the equation intercepts decrease. At 170 and 190°C the coefficients are similar in magnitude and larger than the 220°C coefficients: at 220°C, the $\%BU$ is much less sensitive to changes in operating conditions. The sensitivity of $\%BU$ to Q/N decreases as T_b increases. The N coefficient increases from 170 to 190°C , then sharply decreases in the 220°C equation, indicating a non-linear relationship between N and T_b.

Response surfaces were generated using the equations in Table 5.3. The three T_b surfaces are shown in Figure 5.11.

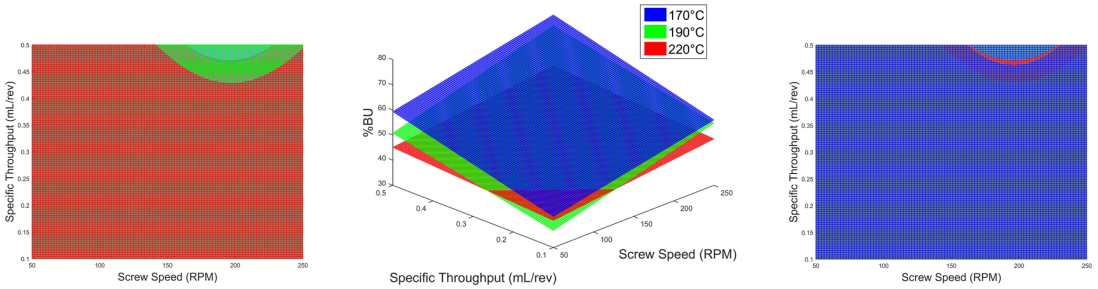

(a) Bottom View (b) Full View (c) Top View

FIGURE 5.11: Response surfaces for degradation with different viewing angles.

The response surfaces in Figure 5.11 shows three stacked planes, decreasing in height with decreasing T_b. The planes linearly increase along the N and Q/N axes due to the insignificance of second order terms. Within the entire operating domain, the $\%BU$ results on the 170°C plane are larger than the other temperatures. However, at low N and Q/N the three T_b planes converge, resulting in the 190°C surface overlapping the 220°C surface. This convergence is likely due to the insignificant non-linear effects at the edge of the CCD grid. At low N and Q/N, the results in the CCD grids in Figure 5.10 show similarities between the two higher T_b conditions, indicating a convergence to a minimum $\%BU$ value for this extrusion process. While increasing N and Q/N can increase the amount of material that experiences 194 kPa of stress, decreasing these operating conditions will not prevent less than approximately 40% of the material from experiencing 194 kPa.

5.3.2 3-D Analysis

A single predictive equation for $\%BU$ was generated using T_b as a continuous variable. The equation is shown in Equation 5.3. The predictive equation for $\%BU$ has an R^2 value of 0.93.

$$\%BU = 54.0 + 3.28N + 3.16\frac{Q}{N} - 4.19T_b - .97\Big(\frac{Q}{N} \cdot T_b\Big) \tag{5.3}$$

The 3-D predictive equation is a function of the intercept, N, Q/N, T_b, and the interaction between T_b and Q/N. The intercept value (54.0) is similar to the intercept of the 190°C condition (53.2), which should result if all variables were set to coordinate zero. While N and Q/N have been significant in every RSD study, in Equation 5.3, the T_b coefficient is more significant within this operating domain. In addition, the interaction between T_b and Q/N was significant, predicted by the decrease in the Q/N coefficients in Table 5.3 as T_b increased. Due to inconsistent trends in the N coefficient, the interaction between T_b and N was not found to be significant in the 3-D equation.

5.3.3 Discussion

The results of the RSD experiment are consistent with the established theory that increasing N and Q/N leads to increases in $\%BU$. At all three T_b, N and Q/N had a significant, positive impact on the $\%BU$, however, the magnitude of their effects varied.

At 170°C , changes in Q/N had the largest effect while at the two lower T_b, N had the largest effect.

This study was also the first RSD experiment to include a third continuous variable, T_b. The T_b had a significant effect on $\%BU$, as seen in the difference in 2-D equation intercepts and coefficient magnitudes. As the T_b increased, the intercept $\%BU$ value decreased as well as the sensitivity to Q/N. The T_b also effected the N sensitivity, but it did not linearly decrease as temperature increased. The N coefficient increased from 170 to 190°C , then sharply decreased at 220°C indicating that at high temperatures, the effect of N on $\%BU$ is dampened.

The relationship between stress and temperature can be explained by the effect of temperature on viscosity. In Figure 5.1, the effect of temperature on viscosity and shear-thinning behavior of Kollidon VA 64 was shown. By multiplying the viscosity by the shear rate, this information is replotted in Figure 5.12 as the shear stress versus the shear rate. It is important to note that the temperatures in Figure 5.1 and 5.12 are melt temperatures, while the T_b temperatures are set barrel temperatures that influence, but do not determine, the melt temperature. The melt temperature is typically higher than the operating T_b due to viscous heating of the melt. However, Figure 5.1 and 5.12 are still used to highlight the effect of temperature on the rheology of the melt and provide insights into the extruder behavior.

In Figure 5.12, the lowest temperature conditions, 170°C, resulted in much higher shear stresses than the lower temperature conditions, which would cause larger $\%BU$ values

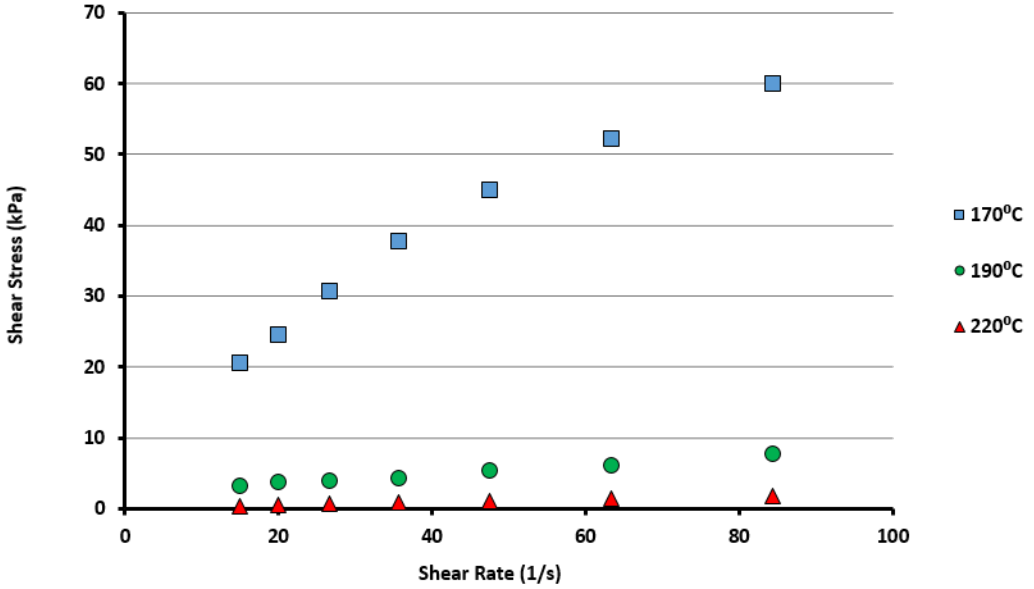

FIGURE 5.12: Shear stress versus shear rate for Kollidon VA 64 at 170, 190, and 220°C.

within the extruder. In addition, the 170°C condition has the steepest slope, indicating high sensitivity to changes in operating conditions, reflected by the large coefficient values at low T_b. At equivalent shear rates, the highest temperature condition, 220°C, resulted in much lower shear stresses, which results in the low $\%BU$ values on the 220°C grid. In addition, the 220°C curve remains nearly constant as shear rate increase, which shows that $\%BU$ has a lower sensitivity at high temperatures. At low shear rates, the 170°C curve approaches the lower temperature results. In addition, the 190 and 220°C curves are closest at the lowest shear rates, and only separate as the shear rate increases. This behavior can be related to the behavior seen at the low N and Q/N on the surfaces in Figure 5.11. At low N and Q/N, the average shear rates will be low, and different melt temperatures will behave similarly. As the shear rates increase, the shear stress results at each melt temperature will diverge.

5.4 Scale Independent Parameter Analysis

Previously, pharmaceutical properties have been modeled as a function of extruder operating conditions since these are directly controllable in a compounding process. While physical effects have been predicted by the significant operating conditions, like the significance of melt temperature due to T_b, the physics inducing the property responses cannot be directly concluded. Physical parameters such as temperature, time, and stress can be measured during an extrusion process but not independently predefined. In the following section the relationship between these physical parameters and pharmaceutical property responses will be investigated in order to develop the physics inducing changes in properties. Physical parameters will be investigated through scale-independent parameters, or variables that hold the same physical meaning on all extruder sizes. The temperature was measured through a melt temperature measurement (T_{melt}) taken as the melt exited the die. The time was evaluated as the t_{mean} measured by the RTD. Finally, the stress was included through the $\%BU$ value determined through the RSD analysis (Section 5.3). The T_{melt} and t_{mean} results are included in Appendix C.

The significance of T_{melt}, t_{mean}, and $\%BU$ was evaluated through a least-squares fit model run in JMP Pro 11.0. The fit model analysis generates an equation for the property responses as a function of the three scale-independent parameters. Since the scale-independent parameters were not predetermined through a DoE, only first order effects of the parameters are investigated. Predictive equations for $\%deg$ and $\%RH$ are both

shown in Table 5.4. The R^2 value in the tables represents how accurately the predictive equations fit the property responses. A "-" in the coefficient column indicates a parameters insignificant effect on the property response (α = .05). Since the scale-independent parameters were not normalized to a DoE grid, the magnitude of the coefficients cannot be directly compared.

TABLE 5.4: Predictive equations for $\%RH$ and $\%deg$ as a function of the selected scale-independent parameters.

Property	Intercept	T_{melt}	t_{mean}	$\%BU$	R^2
$\%RH$	-	-0.045	-	0.076	0.55
$\%deg$	-3.000	0.023	0.003	0.015	0.81

The $\%RH$ equation in Table 5.4 had a low R^2 of 0.55, indicating a weak correlation of the predictive equation. This suggests that more complex physical interactions affect the water content that are not quantified by the included parameters. The previously generated equation (Equation 5.1) for $\%RH$ as a function of the extruder operating conditions had a much high R^2 value of 0.93. The operating conditions in this predictive equation encompass more complex interactions that just time, temperature, and stress, such as the degree of fill and the screw channels as well as the path of the melt through the extruder. In addition, the operating conditions on a TSE can be predefined, unlike the scale-independent parameters, allowing for the DoE approach to determine interactions between operating conditions. Equation 5.1 introduced an interaction between T_b and Q/N, indicating a more complex relationship that was not captured by the equation in Table 5.4.

The $\%deg$ equation in Table 5.4 had a higher R^2 of 0.81, which indicates moderate agreement between the scale-independent parameters and the degradation response. Increases in T_{melt}, t_{mean}, and $\%BU$ all result in increases in degradation. Degradation is commonly attributed to the T_{melt} and the time the melt undergoes high temperatures [11, 12, 76, 85], but the relationship between stress and degradation has not been previously directly investigated. The effect of stress on degradation could be attributed to different effects. Increasing stress in a melt results in higher heat generation through viscous dissipation, however, this effect is already included within the melt temperature reading. Increasing the stress can also reduce the size of the API, similar to the dispersive mixing behavior observed with TiO_2 in Chapter 4. Gogos et al. investigated the effect of API cluster size on dissolution of an API into an polymer carrier. The authors found that smaller API clusters had larger surface areas and improved dissolution behavior [85]. The same relationship may hold true for degradation; increasing the surface area of the API increases the amount of API exposed to the hot melt.

While the $\%deg$ equation in Table 5.4 had a moderate R^2 value, the operating conditions predictive equations (Equation 5.2) had a higher R^2 value of 0.90. In addition, the variables in Equation 5.2 can be predefined, allowing for prediction and design of a process to produce a desired property response. The operating condition predictive equation also illustrated several complex physical interactions that are not clarified with the linear equations in Table 5.4. While degradation analysis typically examines the physical effects of time and temperature, consideration of the operating conditions results in improved accuracy and utility.

5.5 Conclusions

Experiments were completed to determine the effect of the N, Q/N, and T_b operating conditions on pharmaceutical properties. By developing the relationship between operating conditions and property response, operators can design and adapt a pharmaceutical extrusion process to produce safe and viable product. Three pharmaceutical properties were investigated: crystallinity, water content, and degradation. Crystallization was evaluated on a Yes/No basis, where the occurrence of crystalline API would lead to inconsistent dosage after ingestion. In addition, the existence of even a small amount of crystalline API can act as seed crystals, encouraging further recrystallization, and making the drug unsuitable for use. Water content was investigated due to its ability to reduce the glass transition temperature of the drug during storage, leading to recrystallization of amorphous API. Minimizing water content improves the storage life and temperature of the drug. Degradation of the API is a continuous measure, but at high levels, the drug could become unsafe for consumption and may not pass regulations. To maintain a safe product, degradation should be held significantly lower than dangerous levels.

Using the response and predictive equations, the final product properties can be optimized as a function of the operating conditions. Crystallinity was found to be a function of all three operating conditions, but was primarily dominated by T_b and Q/N. Crystalline API was only observed at the lowest T_b (170°C) and at the highest Q/N conditions at that temperature. Degradation was found to be strongly dependent on T_b as

well, with a threshold behavior observed above the 190°C T_b. In order to avoid safety concerns, and to simplify the variables in this analysis, the processing of MK-A will be optimized at 190°C. At 190°C, the 2-D equations for water content and degradation can be used to produce an ideal product. The contour plots for both property responses are shown in Figure 5.13.

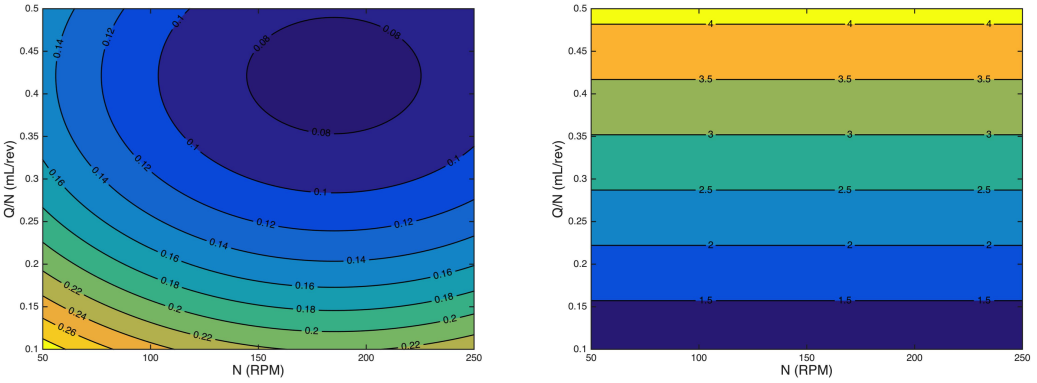

(a) Degradation (b) Water Content

FIGURE 5.13: Contour plots for pharmaceutical property response at 190°C.

The contours in Figure 5.13 can be used by operators to determine ideal operating conditions for extrusion of this drug. If operators need to minimize degradation and minimize water content, according to the contours, processing should be done at approximately 200 RPM. At this N level, the circular contours on the degradation plot reach their lowest value on the Q/N axis; due to the inverse linear relationship between water content and Q/N at 190°C, Q/N should be kept as low as possible. The operating Q/N can be selected based on the exact requirements of the product.

Using the response of pharmaceutical properties to operating conditions, scale-independent parameters were calculated and used to investigate the physical mechanisms behind

changes in properties. The parameters used were T_{melt}, t_{mean}, and $\%BU$, which physically represented the temperature, time, and stress within the extruder. Results poorly predicted the property response, indicating the operating condition approach was a more accurate model for the system. The scale-independent parameter analysis did suggest a potential relationship between degradation and stress, a relationship rarely investigated in the literature. Further investigation of this relationship could highlight a new utility for the RSD experiment in control of pharmaceutical extrusion process.

The collection of RSD data during this experiment also resulted in the novel inclusion a third variable in $\%BU$ analysis, the T_b. Previous RSD experiments had only considered the significance of N and Q/N, but the inclusion of the T_b as a variable provides an additional method of process stress control. Results indicated that T_b significantly affected the $\%BU$ in an extruder melt flow due to effect of temperature on melt viscosity. At high temperatures the viscosity of the melt was so low that $\%BU$ was minimally affected by N and Q/N. At high T_b, high stress levels are not possible to achieve within a reasonable range of extruder operating conditions.

Chapter 6

Conclusions

Conclusions from each experiment were stated at the end of every results section, but key results and contributions to the field will be reiterated in the following section. This will be followed by a description of possible future experimental work.

6.1 Summary of Results and Contributions

6.1.1 Titanium Dioxide Dispersion Study

The results from the Titanium Dioxide Dispersion Study illustrated the dispersion behavior of agglomerated TiO_2 and related it to the stress in a TSE. Preliminary experiments used a novel approach to illustrate the effect of shear stress on the cluster size distribution resulting from TiO_2 dispersion. The results of these experiments highlighted

two important characteristics of TiO_2 dispersion. The first major conclusion was that the rupture mechanism is essential in order to achieve sufficient dispersion in short processing times. The erosion mechanism will continue past the point where rupture ceases, but in comparison, the scale of pure erosion dispersion is significantly lower. During twin-screw compounding, TiO_2 clusters may remain in the mixing section for less than a minute, and potentially a matter of seconds. During these short times, gradual erosion will not sufficiently disperse the TiO_2, therefore mixing sections must be designed to encourage the rapid rupture of large clusters. The second conclusion from the preliminary experiments was the apparent exponential decay in dispersion with increasing stress. At low shear stresses, initial erosion or rupture of large agglomerates is readily improved with small increases in shear stress. However, as the dispersion improves, significantly higher stresses are required to achieve much smaller improvements in dispersion.

Results from the initial experiments demonstrated the importance of achieving large shear stresses within the mixing section of TiO_2 compounding screws. Using the RSD experiment, the stress level within a TSE was evaluated for a standard TiO_2 compounding process with changes in N and Q/N, as well as the screw geometry. As expected from previous RSD experiments, the stress level in the extruder was sensitive to changes in both N and Q/N for all screw geometries. Increases in both operating conditions resulted in increased in $\%BU$. Each screw geometry evaluated resulted in different $\%BU$ responses and differences in sensitivity to operating conditions. The mixing section comprised of entirely wide KBs had the highest average $\%BU$ as well as the greatest sensitivity to operating conditions. These high $\%BU$ values indicate that the

TiO_2 clusters will experience higher stresses, reducing the critical radius for the rupture mode. The MS1 mixing section was derived from the preliminary portion of a standard TiO_2 processing screw. While it generated higher average $\%BU$ than the purely narrow KB mixing section, it had significantly lower $\%BU$ than the wide KB geometry. The sensitivity of MS1 to both N and Q/N was also lower than the wide KB geometry, with behavior more similar to the narrow KB geometry. These results show that compared to the wide KB mixing section, large changes in N and Q/N are required to change the stress developed in MS1.

Another conclusion from the RSD experiment was the significance of paddle width on $\%BU$. The wide KB geometry had the largest KB paddles, but a shorter total length of KBs compared to MS1. Due to the shear-thinning behavior of LDPE, these large paddles are necessary to achieve the high accelerations and shear rates required to significantly increase the stress within the melt. Although MS1 had more KBs, larger KBs, and an intermediate conveying element, it did not achieve significantly different stress behavior than the narrow KB mixing section.

6.1.2 Pharmaceutical Extrusion Process-Property Relationship

The DoE approach used in the RSD experiment was applied to a pharmaceutical extrusion process in order to determine the physical processes affecting pharmaceutical properties as well as the required tradeoffs. In addition to the operating conditions

of N and Q/N, T_b was included in this analysis due to the significance of temperature on pharmaceutical properties. The properties of water content, degradation, and crystallinity were considered due to their significance on drug safety, durability, and effectiveness.

Water content in the extrudate was analyzed due to the ability of residual water to induce recrystallization of the API during storage. Generally, in a pharmaceutical extrusion process, the water content is minimized to improve the storage temperature and lifetime of a drug. Analysis of the water content in the extruded material indicated the significance of Q/N and T_b. In order to achieve low water content, Q/N should be decreased while the T_b should be increased. The effect of Q/N has been attributed to the decreased surface to volume ratio allowing more avenues for vapor removal. The effect of T_b was predicted due to the added heat for evaporation and reduced viscosity allowing for vapor bubble escape. The water content was not significantly affected by N.

Degradation of an API is a limiting factor in many pharmaceutical extrusion processes due to the safety concerns and legal limits for degraded API. In order to minimize degradation of the API, the T_b should be kept below an observed threshold limit. Degradations measurements indicated a threshold melt temperature occurring between the 190°C and 220°C T_b that induced a significant increase in degradation. This threshold temperature provides the energy and heat necessary to induce the degradation reaction. Below this threshold, degradation was a function of Q/N and N although above the threshold the effect of these operating conditions was much more significant.

Crystallinity was also measured across the operating domain to ensure purely amorphous API in the extrudate. Amorphous API results in the improved dissolution and absorption behavior desired from twin-screw compounding. Crystalline API was observed only at the lowest T_b of 170°C indicating that higher temperatures more readily form solid solutions. At 170°C, crystallinity was found at the highest Q/N conditions, or the conditions with the fewest revolutions within the extruder. Fewer revolutions equates to shorter flow paths, which could indicate insufficient distribution of the API to regions of low concentration where dissolution occurs more readily.

The RSD experiment was completed on this pharmaceutical extrusion process, and for the first time included T_b as a continuous independent variable. Results showed that $\%BU$ was highest at low T_b due to the higher viscosity of the melt at low temperatures. In addition, at high temperatures the melt viscosity was reduced so significantly that operating conditions had little effect on the $\%BU$. The $\%BU$ was used along with the measured T_{melt} and t_{mean} to investigate the physical relationships affecting the development of water content and degradation. Results did not produce a reliable predictive equation, indicating the operating condition approach as a superior technique. By predicting property response as a function of the operating conditions, a process can be designed to achieve a predetermined response. While physical parameters can be defined independent of scale, they must be evaluated during an extrusion process and cannot be directly controlled.

6.2 Future Work

Results presented in this thesis present several opportunities for future work in this field. The TiO_2 dispersion experiments demonstrate the utility of characterizing TiO_2 dispersion behavior under constant stress. These experiments could be repeated at higher stresses and shortened times in order to more closely approximate the stress behavior within a TSE. However, this may be limited by the torque limit of the rheometer and the scale of the ramp-up time compared to the total run time. In addition, the effect of extensional stress on dispersion could be investigated, which would require the development of a suitable testing apparatus and method. On a TSE, the stress developed during TiO_2 compounding could be evaluated with new mixing section geometries, including longer sections of a standard processing screw. Development of an offline method to measure the cluster size distribution in the extrudate would also help determine if other dispersing factors besides the stress are influenced by the mixing section design.

In pharmaceutical extrusion, future work could clarify the observed effects. For instance, smaller T_b intervals could be evaluated between 190°C and 220°C in order to pinpoint the threshold temperature for degradation. Similarly, a larger range of operating conditions could be evaluated at 170°C to clarify the N and Q/N conditions that result in crystallinity. For crystallinity measurements, a method to quantify the amount of crystalline material would allow for the creation of a predictive equation that would aid process design and control. Since many of the observed pharmaceutical property results have not been directly reported, future experiments could repeat these operating

conditions with a new excipient and API to determine if these relationships are material dependent.

Appendix A

Image Processing Code

A.1 Single Image Processing

```
close all
clear all
clc

filename = 'rawImage1.bmp';

%% Load and convert image to black and white

originalcolor = imread(filename);
original = rgb2gray(originalcolor);

figure(1)
imshow(original)

%% Determine the background color

background = imopen(original,strel('disk',250));

figure(2)
surf(double(background(1:8:end,1:8:end))),zlim([0 255]);
```

```
set(gca,'ydir','reverse');

%% Remove the background color

no_back = original-background;
figure(3)
imshow(no_back)

%% Increase image contrast

adjusted = imadjust(no_back);
figure(4)
imshow(adjusted)

%% Make all non-dark clusters white

for j = 1:numel(adjusted)
    if adjusted(j)>10
        adjusted(j)=255;
    else
        adjusted(j)=0;
    end
end

figure(5)
imshow(adjusted)

%% Apply a median filter to remove noise

filtered = medfilt2(adjusted,[20 20]);

figure(6)
imshow(filtered)

%% Remove clusters intersecting image border

b2w = imcomplement(filtered);
no_bord = imclearborder(b2w);
L = bwlabel(no_bord);

%% Plot the filtered image over the original

for j = 1:numel(no_bord)
    if no_bord(j)==255
```

```
        original(j)=0;
    end
end

figure(7)
imshow(original)

BaW_pic = figure(8)
imshow(no_bord)

%% Calculate the area and diameter of the clusters

stats = regionprops('table',L,'Area','centroid')

areas = cat(1,stats.Area);

pixels_to_um = 1.35;
um_areas = areas/(pixels_to_um^2);
um_diam= 2*sqrt(um_areas/pi);

%% Create a histogram of diameters for this image

figure(9)
histogram(um_diam,15)
xlabel('Diameter (um)')
ylabel('Count')

%% Output Files

fn = strsplit(filename,'.');
filename2 = 'Image1_processed.bmp';

dlmwrite([char(fn(1)),'_udiam'],um_diam);
print(BaW_pic,'-dpng','-r300',filename2)
```

A.2 Batch Image Processing for One Stress Level

```
close all
clear all
clc
```

```
%% Batch stress level analsysis
filetitle = '100 Pa Diameter Analysis';

%% Read diameter data

D1=dlmread('Image1_processed');
D2=dlmread('Image2_processed');
D3=dlmread('Image3_processed');
D4=dlmread('Image4_processed');
D5=dlmread('Image5_processed');
D6=dlmread('Image6_processed');
D7=dlmread('Image7_processed');
D8=dlmread('Image8_processed');
D9=dlmread('Image9_processed');
D10=dlmread('Image10_processed');
D11=dlmread('Image11_processed');
D12=dlmread('Image12_processed');
D13=dlmread('Image13_processed');
D14=dlmread('Image14_processed');
D15=dlmread('Image15_processed');
D16=dlmread('Image16_processed');
D17=dlmread('Image17_processed');
D18=dlmread('Image18_processed');
D19=dlmread('Image19_processed');
D20=dlmread('Image20_processed');
D21=dlmread('Image21_processed');
D22=dlmread('Image22_processed');
D23=dlmread('Image23_processed');
D24=dlmread('Image24_processed');
D25=dlmread('Image25_processed');
D26=dlmread('Image26_processed');
D27=dlmread('Image27_processed');
D28=dlmread('Image28_processed');
D29=dlmread('Image29_processed');
D23=dlmread('Image30_processed');

%% Combine all diameter info, sort

uD=sort([D1;D2;D3;D4;D5;D6;D7;D8;D9;D10;D11;D12...
    ;D13;D14;D15;D16;D17;D18;D19;D20;D21;D22;...
    D23;D24;D25;D26;D27;D28;D29;D30]);

%% Convert to spherical volume approximation
```

```
vD=(4/3)*pi*(uD/2).^3;
%% Statistics of total diameter data

min_diam_um = min(uD);      % Minimum
max_diam_um = max(uD);      % Maximum
mean_diam_um = mean(uD);    % Mean
std_diam_um = std(uD);      % Standard Deviation
n=numel(uD);                % Total clusters
med_uD = median(uD);        % Median
lower_quartile = quantile(uD,.25);      % 1st Quartile
upper_quartile = quantile(uD,.75);      % 3rd Quartile

% Histogram of diameter data

A = figure(1)
edges = [0:10:500];
H = histogram(uD,edges);
hold on
counts = H.Values;
conf_int = 1.96 * std_diam_um;
xlabel('diameter (um)');
ylabel('count');
title('Diameter Distribution Historgram 100 Pa');
axis([edges(1) edges(end) 0 500])

%% Approximate total volume in bins

index = 1;
counter = 0;

avg_d_in_bin = zeros(1,length(counts));

for i = 1:(length(counts))
    counter = counter+counts(i);
    tot_d_in_bin = sum(uD(index:counter));
    num_p_in_bin = counts(i);
    avg_d_in_bin(i) = tot_d_in_bin/num_p_in_bin;
    index = counter+1;
end

avg_v_in_bin = (4/3)*pi*(avg_d_in_bin/2).^3;

%% Histogram of volume data
```

```
B = figure(2)
xvals = 10:10:500;
bar(xvals,avg_v_in_bin)
xlabel('Particle Diameter Bins (um)')
ylabel('Total Volume in Bin (um^3)')
title('Particle Volume Distribution 100 Pa')
axis([0 500 0 6e7])
set(gca,'yscale','log')

%% Output files

print(A,'-dpng','-r300','diameter100')
print(B,'-dpng','-r300','volume100')

dlmwrite('diameter100',(counts));
dlmwrite('volume100',(avg_v_in_bin));
```

A.3 All Stress Analysis

```
close all
clear all
clc

%% Combined stress level analysis
filetitle = 'Combined Histogram Analysis';

%% Read All Data

D100=dlmread('diameter100')';
D1000=dlmread('diameter1000')';
D5000=dlmread('diameter5000')';
D10000=dlmread('diameter10000')';

V100=dlmread('volume100')';
V1000=dlmread('volume1000')';
V5000=dlmread('volume5000')';
V10000=dlmread('volume10000')';

%% Combine all data
```

```
D_total = [D100 D1000 D5000 D10000];
V_total = [V100 V1000 V5000 V10000];

%% Diameter \\bins

xvals = 10:10:500;

%% Count versus Diameter Plot

A = figure(1)
z = bar(xvals,D_total);
xlabel('Particle Diameter Bins (\mum)')
ylabel('Number of Particles per Bin')
title('Particle Diameter Distribution Plot All Stresses')
axis([0 250 0 500])
legend('100 Pa','1000 Pa','5000 Pa','10000 Pa')
z(1).FaceColor = 'r';
z(2).FaceColor = 'g';
z(3).FaceColor = 'b';
z(4).FaceColor = 'y';
z(1).EdgeColor = 'k';
z(2).EdgeColor = 'k';
z(3).EdgeColor = 'k';
z(4).EdgeColor = 'k';

%% Volume versus Diameter Plot

B = figure(2)
hold on
y = bar(xvals,V_total);
xlabel('Particle Diameter Bins (\mum)')
ylabel('Total Volume per Bin (\mum^3)')
title('Particle Volume per Bin All Stresses')
axis([0 250 1 6e7])
legend({'100 Pa','1000 Pa','5000 Pa','10000 Pa'}...
,'Location','northwest')
y(1).FaceColor = 'r';
y(2).FaceColor = 'g';
y(3).FaceColor = 'b';
y(4).FaceColor = 'y';
y(1).EdgeColor = 'k';
y(2).EdgeColor = 'k';
y(3).EdgeColor = 'k';
y(4).EdgeColor = 'k';
```

```
set(gca,'yscale','log')
hold off

%% Output files

print(A,'-dpng','-r300','diameterALL')
print(B,'-dpng','-r300','volumeALL')
```

Appendix B

Titanium Dioxide Dispersion Screw Designs

The three screw designs used in the titanium dioxide dispersion study are shown in Figure B.1 below. The T_b is indicated for each barrel on the 30 mm extruder.

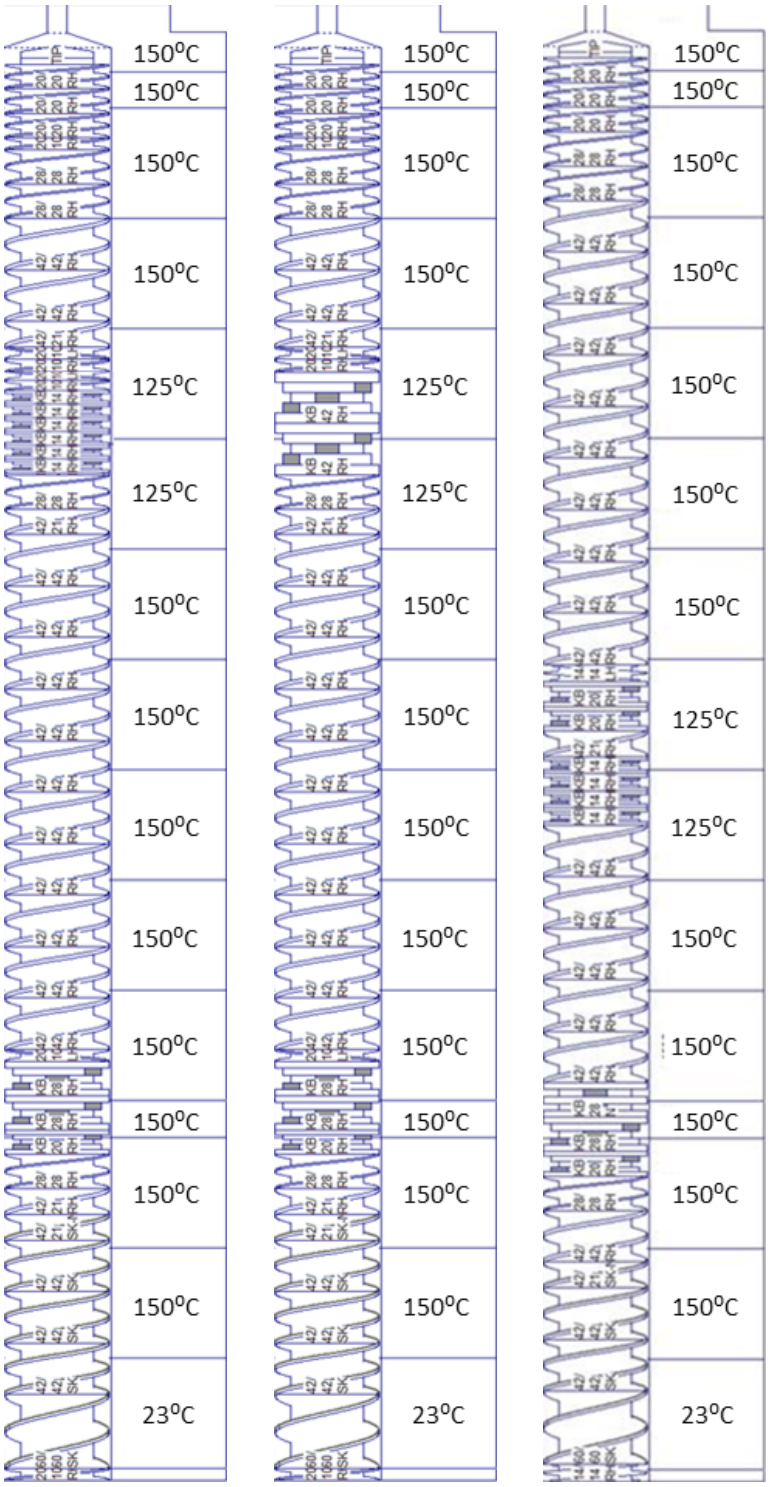

(a) Narrow KB (b) Wide KB (c) MS1

FIGURE B.1: Screw geometries for titanium dioxide dispersion study.

Appendix C

Scale Independent Parameters

The T_{melt} and t_{mean} data used in 5.4 are listed in Table C.1 below.

TABLE C.1: T_{melt} and t_{mean} data from pharmaceutical extrusion study.

T_b (°C)	N (RPM)	Q/N (mL/rev)	T_{melt} (°C)	t_{mean} (s)
170	50	0.3	135	189
	100	0.2	154	128
	150	0.1	160	161
	100	0.4	158	75
	150	0.3	161	77
	200	0.2	165	62
	150	0.5	161	51
	200	0.4	172	43
	250	0.3	175	41
190	50	0.3	143	257
	100	0.2	146	161
	150	0.1	151	197
	100	0.4	150	79
	150	0.3	154	71
	200	0.2	164	76
	150	0.5	161	50
	200	0.4	168	43
	250	0.3	170	50
220	50	0.3	161	336
	100	0.2	161	174
	150	0.1	169	169
	100	0.4	163	107
	150	0.3	165	88
	200	0.2	173	85
	150	0.5	172	65
	200	0.4	173	52
	250	0.3	176	50

Bibliography

[1] Harold F. Giles, John R. Wagner, and Eldridge M. Mount. *Extrusion: The Definitive Processing Guide and Handbook*. William Andrews Publishing/Plastics Design Library, 2004.

[2] Y.S. Song and J.R. Youn. Influence of dispersion states of carbon nanotubes on physical properties of epoxy nanocomposites. *Carbon*, 43(7):1378–1385, June 2005.

[3] G.R. Kasaliwal, A. Goldel, P. Potschke, and G. Heinrich. Influences of polymer matrix melt viscosity and molecular weight on mwcnt agglomerate dispersion. *Polymer*, 52(4):1027–1036, February 2011.

[4] J.R. Nixon, I. Lempert, H. Choi, J. McFarlane, and D.I. Bigio. Effect of variable fiber orientation on material properties in extruded polymer composites with multiscale additives. In *ANTEC*, 2015.

[5] Y.J. Lee, I. Manas-Zloczower, and D.L. Feke. Analysis of titanium dioxide agglomerate dispersion in linear low density polyethylene and resulting properties of compounds. *Polymer Engineering & Science*, 35(12):1037–1045, June 1995.

[6] Y. Zhu, G.G. Buonocore, M. Lavorgna, and L. Ambrosio. Poly(lactic acid)/titanium dioxide nanocomposite films: Influence of processing procedure on dispersion of titanium dioxide and photocatalytic activity. *Polymer Composites*, 32(4):519–528, April 2011.

[7] G. Nichols, S. Byard, M.J. Bloxham, J. Botterill, N.J. Dawson, A. Dennis, V. Diart, N.C. North, and J.D. Sherwood. A review of the terms agglomerate and aggregate with a recommendation for nomenclature used in powder and particle characterization. *Journal of Pharmaceutical Sciences*, 91(10):2103–2109, October 2002.

[8] F. Bohin, I. Manas-Zloczower, and D.L. Feke. Kinetics of dispersion for sparse agglomerates in simple shear flows: Application to silica agglomerates in silicone polymers. *Chemical Engineering and Science*, 51(23):5193–5204, December 1996.

[9] B. Mayoral, G. Garrett, and T. McNally. Influence of screw profile employed during melt mixing on the micro-scale dispersion of mwcnts in poly(propylene). *Macromolecular Materials and Engineering*, 299(6):748–756, June 2014.

[10] G.P. Milligan, G.M. McNally, W.R. Murphy, and M. Leathem. The effect of tio_2 pigment particle size and masterbatch rheology on the dispersion performance of tio_2 pigment within the polyethylene blow film process. In *ANTEC*, 2001.

[11] A. Forster, J. Hempenstall, and T. Rades. Characterization of glass solutions of poorly water-soluble drugs by melt extrusion wiht hyrdophilic amorphous polymer. *Journal of Pharmacy and Pharmacology*, 53(3):303–315, March 2001.

[12] C. Leuner and J. Dressman. Improving drug solubility for oral delivery using solid dispersions. *European Journal of Pharmaceutics and Biopharmaceutics*, 50 (1):47–60, July 2000.

[13] T. Vasconcelos, B. Sarmento, and P. Costa. Solid dispersions as strategy to improve oral bioavailability of poor water soluble drugs. *Drug Discovery Today*, 12 (23-24):1068–1075, December 2007.

[14] F. Zhang and J.W. McGinity. Properties of hot-melt extruded theophylline tables containing poly(vinyl acetate). *Drug Development and Industrial Pharmacy*, 26 (9):931–942, September 2000.

[15] M. Crowley, F. Zhang, M. Repka, S. Thumma, S. Upadhye, S. Battu, J. McGinity, and C. Martin. Pharmaceutical applications of hot-melt extrusion: Part i. *Drug Development and Industrial Pharmacy*, 33(9):909–926, September 2007.

[16] M. Repka, N. Langley, and J. DiNuzio. *Melt Extrusion: Materials, Technology and Drug Product Design*. Springer-Verlag New York, 1st edition, 2013.

[17] C. Martin. Twin screw extruders as a continuous mixer for thermal processing: A technical and historical perspective. *AAPS PharmSciTech*, 17(1):3–19, February 2016.

[18] Klemens Kohlgruber. *Co-Rotating Twin-Screw Extruders: Fundamentals, Technology, and Applications*. Hanser Publishers, 2008.

[19] W. Wang, I. Manas-Zloczower, and M. Kaufman. Characterization of distributive mixing in polymer processing equipment using renyi entropies. *International Polymer Processing*, 16(4):315–322, December 2001.

[20] G. Shearer and C. Tzoganakis. The effects of kneading block design and operating conditions on distributive mixing in twin screw extruders. *Polymer Engineering & Science*, 40(5):1095–1106, May 2000.

[21] D. Kalyon and H. Sangani. An experimental study of distributive mixing in fully intermeshing, co–rotating twin screw extruders. *Polymer Engineering & Science*, 29(15):1018–1026, August 1989.

[22] B. Alsteens, V. Legat, and T. Avalosse. Parametric study of the mixing efficiency in a kneading block section of a twin-screw extruder. *International Polymer Processing*, 19(3):207–217, September 2004.

[23] V.L. Bravo, A.N. Hrymak, and J.D. Wright. Study of particle trajectories, residence times and flow behavior in kneading discs of intermeshing co-rotating twin-screw extruders. *Polymer Engineering & Science*, 44(4):779–793, April 2004.

[24] G. Shearer and C. Tzoganakis. Distributive mixing profiles for co–rotating twinâĂŘscrew extruders. *Advances in Polymer Technology*, 20(3):169–190, July 2001.

[25] C. Rauwendaal. Mixing in extrusion: Part one, general considerations. In *ANTEC*, 2002.

[26] M.A. Huneault, M.F. Champagne, and A. Luciani. Polymer blend mixing and dispersion in the kneading section of a twin-screw extruder. *Polymer Engineering & Science*, 36(12):1694–1706, June 1996.

[27] S.V. Kao and S.G. Mason. Dispersion of particles by shear. *Nature*, 253:619–621, February 1975.

[28] K. Higashitani, K. Iiamura, and H. Sanda. Simulation of deformation and breakup of large aggregates in flows of viscous fluids. *Chemical Engineering Science*, 56 (9):2927–2938, May 2001.

[29] D.B. Todd. Residence time distribution in twin-screw extruders. *Polymer Engineering & Science*, 15(6):437–443, June 1975.

[30] O.S. Carneiro, G. Caldeira, and J.A. Covas. Flow patterns in twin-screw extruders. *Journal of Material Processing Technology*, 92-93:309–315, August 1999.

[31] J. Gao, G.C. Walsh, D. Bigio, R.M. Briber, and M.D. Wetzel. Residence-time distribution model for twin-screw extruders. *AIChE Journal*, 45(12):2541–2549, December 1999.

[32] T.J. Melo and S. Canevarolo. An optical device to measure in-line residence time distribution curvers during extrusion. *Polymer Engineering & Science*, 42(1):170–181, January 2002.

[33] A. Witschnigg, R.K. Selvasankar, S. Laske, and C. Holzer. An easy approach of measuring the residence time distribution with the use of nir-spectroscopy. *SPE ANTEC Orlando*, 2012.

[34] F. Apruzzese, J. Pato, S.T. Balke, and L.L. Diosady. In-line measurement of residence time distribution in a co-rotating twin-screw extruder. *Food Research International*, 36(5):461–467, September 2003.

[35] J. Puaux, G. Bozga, and A. Ainser. Residence time distribution in a co-rotating twin-screw extruder. *Chemical Engineering and Science*, 55(9):1641–1651, May 2000.

[36] R.M. van den Einde, P. Kroon, A.J. van der Goot, and R.M. Boom. Local mixing effects of screw elements during extrusion. *Polymer Engineering & Science*, 45 (3):271–278, January 2005.

[37] G. Shearer and C. Tzoganakis. Relationship between local residence time and distributive mixing in sections of a twin-screw extruder. *Polymer Engineering & Science*, 41(12):2206–2215, December 2001.

[38] Z. Sun, C.K. Jen, C.K. Shih, and D.A. Denelsbeck. Application of ultrasound in the determination of fundamental extrusion performance: Residence time distribution measurement. *Polymer Engineering & Science*, 43(1):102–111, January 2003.

[39] S.V. Kao and G.R. Allison. Residence time distribution in a twin-screw extruder. *Polymer Engineering & Science*, 24(9):645–651, June 1984.

[40] R.E. Altomare and P. Ghossi. An analysis of residence time distribution patterns in a twin screw cooking extruder. *Biotechnology Progress*, 2(3):102–111, September 1986.

[41] T.J.A. de Melo, L.A. Pinheiro, and S.V. Canevarlo. Factorial design to quantify the influence of extrusion parameters in the mean residence time. *Polimeros*, 20 (4):322–326, November 2010.

[42] S.Y. Lee, M.A. Hanna, and D.D. Jones. Residence time distribution determination using on-line digital image processing. *Starch*, 61(3-4):146–153, March 2009.

[43] A. Kumar, G.M. Ganjyal, D.D. Jones, and M.A. Hanna. Digital image processing for measurement of residence time distribution in a laboratory extruder. *Journal of Food Engineering*, 75(2):237–244, July 2006.

[44] A. Gautam and G. Choudhury. Screw configuration effects of residence time distribution and mixing in twin-screw extruders during extrusion of rice flour. *Journal of Food Process Engineering*, 22(4):263–285, October 1999.

[45] G.E. Gasner, D. Bigio, C.Marks, F. Magnus, and C. Kiehl. A new approach to analyzing residence time and mixing in a co-rotating twin screw extruder. *Polymer Engineering & Science*, 39(2):286–298, February 1999.

[46] X.M. Zhang, L.F. Feng, S. Hoppe, and G.H. Hu. Local residence time, residence revolution and residence volume distributions in twin-screw extruders. *Polymer Engineering & Science*, 48(1):19–28, January 2008.

[47] P. Elkouss, D.I. Bigio, M.D. Wetzel, and S.R. Raghavan. Influence of polymer viscoelasticity of the residence distributions of extruders. *AIChe Journal*, 52(4): 1451–1459, January 2006.

[48] M.L. Booy. Geometry of fully wiped twin-screw equipment. *Polymer Engineering & Science*, 18(12):973–984, Septermber 1978.

[49] C.D. Denson and B.K. Hwang Jr. The influence of the axial pressure gradient on flow rate for newtonian liquids in a self wiping, co-rotating twin screw extruder. *Polymer Engineering & Science*, 20(14):965–971, September 1980.

[50] Z. Tadmor and C.G. Gogos. *Principles of Polymer Processing*. Wiley-Interscience, Hoboken, New Jersey, 2006.

[51] B. Dryer, G. Fukuda, J. Webb, D. Bigio, M. Wetzel, and P. Andersen. Dispersive mixing consideration of twin-screw compounding scale-up methodologies. In *ASME IMECE Houston*, 2015.

[52] M. Suparno, K.D. Kolan, P.K.W. Ng, and J.F. Steffe. Average shear rate in a twin-screw extruder as a function of degree of fill, flow behavior index, screw speed and screw configuration. *Journal of Food Process Engineering*, 34(4):961–982, August 2011.

[53] J. Cheng, Y. Xie, and D. Bigio. Characterization of kneading block performance in a co-rotating twin screw extruder. In *ANTEC*, 1998.

[54] R. Mudalamane and D.I. Bigio. Experimental characterization of fill length behavior in extruders. *Polymer Engineering & Science*, 44(3):557–563, March 2004.

[55] J. Curry and A. Kiani. Measurement of stress level in continuous melt compounders. In *ANTEC*, 1990.

[56] J. Curry and A. Kiani. Experimental identification of the distribtuion of fluid stresses in continuous melt compounders. In *ANTEC*, 1991.

[57] D. Bigio, W. Pappas, H. Brown II, B. Debebe, and W. Dunham. Residence stress distributions in twin screw extruders. In *ANTEC*, 2011.

[58] W.L. Pappas, H. Brown II, G. Fukuda, R. Adnew, and D. Bigio. Variable strength stress bead analysis in a twin screw extruder. In *ANTEC*, 2012.

[59] G. Fukuda, R. Adnew, H. Brown II, and D. Bigio. An expanded residence stress distribution study in a twin-screw extruder: the effect of stress bead strength. In *ANTEC*, 2013.

[60] D. Bigio, G. Fukuda, R. Adnew, J. Kim, and B. Bhatia. Residence stress distribution using a robust design of experiment approach. In *ANTEC*, 2013.

[61] G. Fukuda, B. Dryer, J. Webb, D. Bigio, M. Wetzel, and P. Andersen. Combinatorial effects of kneading elements on mixing in twin-screw compounnding. In *ANTEC*, 2015.

[62] S.P. Rwei, I. Manas-Zloczower, and D.L. Feke. Observation of carbon black agglomerate dispersion in simple shear flows. *Polymer Engineering & Science*, 30 (12):701–706, June 1990.

[63] P.M. Adler and P.M. Mills. Motion and rupture of a porous sphere in a linear flow field. *Journal of Rheology*, 23(1):25–37, February 1979.

[64] I. Manas-Zloczower, A. Nir, and Z. Tadmor. Dispersive mixing in internal mixers–a theoretical model based on agglomerate rupture. *Rubber Chemistry and Technology*, 55(5):1250–1285, November 1982.

[65] R.C. Sonntag and W.B. Russel. Structure and breakup of flocs subjected to fluid stresses. *Journal of Colloid and Interface Science*, 113(2):399–413, October 1986.

[66] S.P. Rwei and I. Manas-Zloczower. Characterization of agglomerate dispersion by erosion in simple shear flows. *Polymer Engineering & Science*, 31(8):558–562, April 1991.

[67] M. Fanelli, D. Feke, and I. Manas-Zloczower. Prediction of the dispersion of particle clusters in the nanoscale - part i: Steady shearing response. *Chemical Engineering Science*, 61(2):473–488, January 2006.

[68] A. Scurati, D.L. Feke, and I. Manas-Zloczower. Analysis of the kinetics of agglomerate erosion in simple shear flows. *Chemical Engineering Science*, 60(23): 6564–6573, December 2005.

[69] Y.J. Lee, D.L. Feke, and I. Manas-Zloczower. Dispersion of titanium dioxide agglomerates in viscous media. *Chemical Engineering Science*, 48(19):3363–3372, October 1993.

[70] J. Boyle, I. Manas-Zloczower, and D.L. Feke. Influence of particle morphology and flow conditions on the dispersion behavior of fumed silica in silicone polymers. *Particle & Particle Systems Characterization*, 21(3):205–212, October 2004.

[71] Y. Komoda, K. Kameyama, E. Hasegawa, H. Suzuki, H. Usui, Y. Endo, and A. Syudo. Behavior of fine particle agglomerates in a newtonian molten polymer under a shear flow. *Advanced Powder Technology*, 19(6):507–521, 2008.

[72] T. Villmow, P. Potsche, S. Pegel, L. Haussler, and B. Kretzchmar. Influence of twin-screw extrusion conditions on the dispersion of multi-walled carbon nanotubes ina poly(lactic acid) matrix. *Polymer*, 49(16):3500–3509, July 2008.

[73] K. Sekiguchi and N. Obi. Studies on absorption of eutectic mixtures. i. a comparison of the behavior of eutectic mixture of sulfathiazole and that of ordinary sulfathiazole in man. *Chemical & Pharmaceutical Bulletin*, 9(11):866–872, November 1961.

[74] W.L. Chious and S. Riegelman. Pharmaceutical applications of solid dispersion systems. *Journal of Pharmaceutical Sciences*, 60(9):1281–1302, September 1971.

[75] J. Breitenbach. Melt extrusion: from process to drug delivery technology. *European Journal of Pharmaceutics and Biopharmaceutics*, 54(2):107–117, September 2002.

[76] A. Serajuddin. Solid dispersion of poorly water-soluble drugs: early promises, subsequent problems, and recent breakthroughs. *Journal of Pharmaceutical Sciences*, 88(10):1058–1066, October 1999.

[77] V. Tantishaiyakul, N. Kaewnopparat, and S. Ingkatawornwong. Properties of solid dispersions of piroxicam in polyvinylpyrrolidone k-30. *International Journal of Pharmaceutics*, 143(1):59–66, October 1996.

[78] H. Suzuki and H. Sunada. Some factors influencing the dissolution of solid dispersions with nicotinamide and hydroxypropylmethylcellulose as combined carrier. *Chemical & Pharmaceutical Bulletin*, 46(6):1015–1020, June 1998.

[79] A. Forster, J. Hempenstall, I. Tucker, and T. Rades. Selection of excipients for melt extrusion with two poorly water-soluble drugs by solubility parameter calculation and thermal analysis. *International Journal of Pharmaceutics*, 226(1-2):147–161, September 2001.

[80] Y. Shibata, M. Fujii, Y. Sugamura, R. Yoshikawa, S. Fujimoto, S. Nakanishi, Y. Motosugi, N. Koizumi, M. Yamada, K. Ouchi, and Y. Watanabe. The preperation of a solid dispersion powder of indomethacin with crospovidone using a twin-screw extruder or kneader. *International Journal of Pharmaceutics*, 365(1-2):53–60, January 2009.

[81] K. Nakamichi, T. Nakano, H. Yasuura, and Y. Kawashima. The role of the kneading paddle and the effects of screw revolution speed and water content on the preparation of solid dispersions using a twin-screw extruder. *International Journal of Pharmaceutics*, 241(2):53–60, July 2002.

[82] H. Liu, P. Wang, X. Zhang, F. Shen, and C. Gogos. Effects of extrusion process parameters on the dissolution behavior of indomethacin in eudragit epo solid dispersions. *International Journal of Pharmaceutics*, 383(2):161–169, January 2010.

[83] J.G. Lyons, P. Blackie, and C.L. Higginbotham. The significance of variation in extrusion speeds and temperatures on a peo/pcl blend based matrix for oral drug delivery. *International Journal of Pharmaceutics*, 351(1-2):201–208, March 2008.

[84] M. Li, C.G. Gogos, and N. Ioannidis. Improving the api dissolution rate during pharmaceutical hot-melt extrusion i: effect of the api particle size, and the co-rotating, twin-screw extruder configuration on the api dissolution rate. *International Journal of Pharmaceutics*, 478(1):201–208, January 2015.

[85] C.G. Gogos and H. Liu. Laminar dispersive and distributive mixing with dissolution and applications to hot-melt extrusion. In Dennis Douroumis, editor, *Hot-Melt Extrusion: Pharmaceutical Applications*, chapter 12, pages 266–290. John Wiley & Sons LTD, 2012.

[86] B. Hancock, S. Shamblin, and G. Zografi. Molecular mobility of amorphous pharmaceutical solids below their glass transition temperature. *Pharmaceutical Research*, 12(6):799–806, June 1995.

[87] V. Andronis, M. Yoshioka, and G. Zografi. Effects of sorbed water on the crystallization of indomethacin from the amorphous state. *Journal of Pharmaceutical Science*, 86(3):346–351, March 1997.

[88] B. Hancock and G. Zografi. The relationship between the glass transition temperature and the water content of amorphous pharmaceutical solids. *Pharmaceutical Research*, 11(4):471–477, April 1994.

[89] D.G. Baird and D.I. Collias. *Polymer Processing: Principles and Design*. Wiley-Interscience, Hoboken, New Jersey, 2nd edition, 2006.

[90] J. Biesenberger. *Devolatilization of Polymers: fundaments, equipment, applications*. Hanser-Verlag, 1st edition, 1983.

[91] J. Feng, L. Xu, R. Gao, Y. Luo, and X. Tang. Evaluation of polymer carriers with regard to bioavailability enhancement of bifendate solid dispersions prepared by hot melt extrusion. *Drug Development and Industrial Pharmacy*, 38(6):735–743, June 2012.

[92] J.P. Lakshman, Y. Cao, J. Kowalski, and A.T.M> Serajuddin. Application of melt extrusion in the development of a physically and chemically stable high-energy amorphous solid dispersion of a poorly-water soluble drug. *Molecular Pharmaceutics*, 5(6):994–1002, November 2008.

[93] U. Diebold. The surface science of titanium dioxide. *Surface Science Reports*, 48 (5-8):53–229, January 2003.

[94] A.N. Ghebremeskel, C. Vemavarapu, and M. Lodaya. Use of surfactants as plasticizers in preparing solid dispersions of poorly water soluble api: selection of polymer-surfactant combinations using solubility parameters and testing the processability. *International Journal of Pharmaceutics*, 328(2):119–129, January 2007.